The Method of Fundamental Solutions and MCMC Methods for Solving Electrical Tomography Problems

Taysir Emhemed Dyhoum

Submitted in accordance with the requirements for the degree of

Doctor of Philosophy

The University of Leeds

School of Mathematics

August 2016

The candidate confirms that the work submitted is his/her own, except where work which has formed part of jointly authored publications has been included. The contribution of the candidate and the other authors to this work has been explicitly indicated below. The candidate confirms that appropriate credit has been given within the thesis where reference has been made to the work of others.

Joint Publications

Some material of Chapters 2 and 3 is based on one published journal paper and one published chapter in a book, as follows:

▶ Journal Publication

1. Dyhoum, T. E., Lesnic, D. and Aykroyd, R. G. (2014) Solving the complete-electrode direct model of ERT using the boundary element method and the method of fundamental solutions, *Electronic Journal of Boundary Elements*, Vol.12, pp.26–71.

▶ Chapter in a Book

1. Dyhoum, T. E., Aykroyd, R. G. and Lesnic, D. (2016) Reconstructing rigid inclusions in the complete-electrode model of ERT, In: *Inverse Problems and Computational Mechanics*, Chapter 4, (eds. L. Marin, L. Munteanu and V. Chiroiu), pp.73–102.

Acknowledgements

Thanks to Allah (subhanahu wa ta'ala), who has provided me with his spiritual support which is indispensable to sustain me to complete this thesis.

I would like to express my gratitude to Professor Daniel Lesnic, not just for introducing me to such an interesting area of research but also for guiding me through the present work and supporting me during the difficult times I experienced. My sincere gratitude also goes to my co-supervisor Dr. Robert Aykroyd, who offered me valuable suggestions throughout my PhD studies.

Many thanks to:
My parents, whose emotional and physical support is the secret to mine and my siblings' success.
My husband, whose words of motivation and encouragement do not vanish in my mind.
My little sons, who prayed a lot for me especially if they saw me with my laptop bag leaving the flat,
and My sister 'Eman', who shares the same experience of being a mum whilst studying a PhD at University of Leeds and is always ready to help me.

I would like to thank my external examiner Dr. Manuchehr Soleimani from University of Bath and my internal examiner Professor Charles Taylor, for their kindness, as well as for the enjoyable Viva discussion that they made.

Finally, I am also very grateful to my colleagues Mohammed, Areena and Shilan who were willing to give me a technical help as soon as I needed it, as well as the Ministry of Libyan Higher Education and Libyan embassy for their phenomenal support.

Abstract

Electrical impedance tomography (EIT) is a non-intrusive and portable imaging technique which has been used widely in many medical, geological and industrial applications for imaging the interior electrical conductivity distribution within a region from the knowledge of the injected currents through attached electrodes and resulting voltages, or boundary potential and current flux. If the quantities involved are all real then EIT is called electrical resistance tomography (ERT).

The work in this thesis focuses on solving inverse geometric problems in ERT where we seek detecting the size, the shape and the location of inner objects within a given bounded domain. These ERT problems are governed by Laplace's equation subject either to the most practical and general boundary conditions, forming the so-called complete-electrode model (CEM), in two dimensions or to the more idealised boundary conditions in three-dimensions called the continuous model.

Firstly, the method of the fundamental solutions (MFS) is applied to solve the forward problem of the two-dimensional complete-electrode model of ERT in simply-connected and multiple-connected domains (rigid inclusion, cavity and composite bi-material), as well as providing the corresponding MFS solutions for the three-dimensional continuous model. Secondly, a Bayesian approach and the Markov Chain Monte Carlo (MCMC) estimation technique are employed in combinations with the numerical MFS direct solver in order to obtain the inverse solution.

The MCMC algorithm is not only used for reconstruction, but it also deals with uncertainty assessment issues. The reliability and accuracy of a fitted object is investigated through some meaningful statistical aspects such as the object boundary histogram and object boundary credible intervals.

Nomenclature

Roman Symbols

A, B	BEM matrices
$\underline{B}$	electric flux density (Chapter 1) and single vector of MCMC parameters (Chapter 3)
$\underline{c}$	vector/matrix of MFS coefficients
D	coefficient matrix obtained from applying the BEM to CEM problem
$\underline{D}$	magnetic current density
$\underline{E}$	electric field
F	coefficient matrix obtained from applying the MFS to CEM problem
$\tilde{F}$, $\hat{F}$, $\breve{F}$	coefficient matrices obtained from applying the BEM to three-dimensional continuous model problem
g_p	gaps between the attached electrodes
G	fundamental solution
G', $\frac{\partial G}{\partial n}$	normal derivative of fundamental solution
$\underline{H}$	magnetic field
I	identity matrix
I_p	current injected via the electrode ε_p
j	current density in Chapter 1
$\underline{J}$	current
ℓ_p	length or the area of electrode p
$l(\underline{w}\|\underline{r}, \underline{c})$	conditional distribution or likelihood of $\underline{w}$ given $\underline{r}$ and $\underline{c}$
L	number of electrodes
M	number of boundary elements
$\underline{n}$, $\underline{n}_1$, $\underline{n}_2$	outward unit normals
N	number of source points (degree of freedom)

$\mathcal{N}$	normal distbution
$\underline{p}$	collocation points
$\underline{p}'$	source points
$\underline{p}_j$	boundary element endpoint
$\underline{\tilde{p}}_j$	boundary element midpoint
$\underline{r}$	vector of discretised radii
R	radius of circle/sphere where the external source points are located
R_1	radius of circle/sphere where the internal source points are located for first inclusion
R_2	radius of circle/sphere where the internal source points are located for second inclusion
s	external boundary segment
S	distance between centres of two circles/spheres
$\underline{T}$	vector of noisy voltage data
u	electric potential
u', $\frac{\partial u}{\partial n}$	current flux (normal derivative)
U_p	measured voltages on the attached electrode ε_p
$\mathcal{U}$	uniform distribution
$\underline{v}$	vector of noisy current flux data
$\underline{w}$	vector of noisy potential data
$\underline{x}$	collocation points
$\underline{X}$	unknown vector of linear system of algebraic equations
X_0, X_1	x-coordinates of unknown centres of two circles or spheres
$\mathcal{X}$	defined spaces
Y_0, Y_1	y-coordinates of unknown centres of two circles or spheres
$\mathcal{Y}$	defined spaces
z_p	surface/contact impedance between the attached electrode ε_p and the object

Z_0, Z_1	z-coordinates of unknown centres of two spheres

Greek Symbols

α_j, α_{j-1}	BEM discretised angles in Chapter 2
α_c	hyper-prior parameters for the MFS coefficients model parameters
α_r	hyper-prior parameters for the radii model parameters
β	BEM discretised angle in Chapter 2
β_c	the amount of variation between two adjacent MFS coefficients
β_r	the amount of variation between adjacent radii
γ	ratio between conductivities of two materials
δ	Dirac delta function
δ_{ij}	Kronecker delta function
ϵ	electric permittivity (Chapter 1) and ellipse parameter (Chapter 3)
ε_p	attached electrodes
ζ_j	additive noise variables
η_I	contraction parameter
η_j	additive noise variables
η_E	dilation parameter
$\underline{\theta}$	vector of discretised angles
μ	magnetic permeability
$\underline{\xi}$	sources ('singulaties') vector
$\pi(\underline{c}\|\beta_c)$	prior distribution for the MFS coeffiecents
$\pi(\underline{r}\|\beta_r)$	prior distribution for radii
ρ	volume charge density
σ	conductivity
σ_T^2, σ_v^2, σ_w^2	proposed variance

$\varsigma(\underline{r}, \underline{c})$	expectation of the voltage values
τ_v^2	proposed variance
$\underline{\phi}$	vector of discretised angles
ψ	BEM angle
Ω	domain (unit disk/sphere)
$\partial\Omega$	boundary of the domain
$\overline{\Omega}$	closure of Ω

Abbreviations

BEM	boundary element method
CCI	constant contact impedance
CEM	complete electrode model
$cond$	condition number
diam	diameter of the star-shaped object
EIT	electrical impedance tomography
ERT	electrical resistance tomography
FDM	finite difference method
FEM	finite element method
FVM	finite volume method
MCMC	Markov chain Monte Carlo
MFS	method of fundamental solustions
sign	signum function

Subscripts

u_{Inner}	potential solution on internal boundary $\partial\Omega$ (cavity) or on $\partial\Omega_2$ (bi-material composite)
$(\partial u/\partial n)_{Inner}$	current flux on the internal boundary $\partial\Omega_{Inner}$ (rigid inclusion) or on $\partial\Omega_2$ (bi-material composite)
$\Omega_{Inner} = \Omega_2$	inner object

u_{Outer}	potential solution on external boundary $\partial\Omega$ (rigid inclusion and cavity) or on $\partial\Omega_1$ (bi-material composite)
$(\partial u/\partial n)_{Outer}$	current flux on external boundary $\partial\Omega$ (rigid inclusion and cavity) or on $\partial\Omega_1$ (bi-material composite)
$\partial\Omega_{Outer}$	Outer boundary of Ω

Superscripts

u^{BEM}	BEM solution
$(\partial u/\partial n)^{BEM}$	BEM normal dervative
u^{MFS}	MFS solustion
$(\partial u/\partial n)^{MFS}$	MFS normal dervative

Contents

List of Figures

List of Tables

Chapter 1

Introduction

1.1 Electrical impedance tomography and its applications

Electrical impedance tomography (EIT) is a non-intrusive, low-cost and portable technique of imaging the interior of a specimen based on the knowledge of injected currents and the resulting voltages which are measured on electrodes, as explained in [35, 36, 63, 65]. It has widespread applications in medicine (biomedical applications) such as detecting and imaging malignant breast tumours [20, 21], comparing the complex impedance properties of two different tissues [16], producing images of lung and ventilation [27], monitoring brain function [32], identifying skin cancer [1], diagnosing cervical cancer [9], measuring gastric emptying of liquid feed and impedance changes which occurs while the human brain is performing its activities [62, 64], and constructing images of minimally invasive surgery [50]. If all the quantities involved are real then, this version of the more general complex EIT is also known as electrical resistance tomography (ERT). As for non-clinical applications, EIT/ERT is also used in geophysics and industry, for instance, it is applied to discover subsurface features without digging [56], study gas-solids and liquid-solids flows [25], collect data from two-phase pipe flow systems [23], investigate the mixing processes at industrial plant

scale [48] and observe hydrocyclone operation, [69].

When using this technique in electrostatics, for example, one seeks to create images of the electrical conductivity distribution in a body from static electrical measurements on the boundary of that body; the electric conductivity measures the ability of a material to pass an electric current whilst the electrical permittivity measures the ability of a material to interact with an electric field and become polarized by the field. In addition to this, due to the differences in conductive properties in muscle tissue, fat tissue, bones, and organs, an image of the conductivity and permittivity distributions inside the body can be used for effective medical diagnostics. By using the EIT imaging method, tumors can be detected and distinguished from healthy tissue at an early stage because not only do the different organs have different conductivity, but also the normal and abnormal tissues have different conductivity and permittivity, e.g. cancer cells contain a higher concentration of water and sodium [16]. Another advantage to EIT is that it has safe long term effects no matter how many EIT experiments have been preformed on the patient. In contrast, when using mammography, X-rays can be used for the same purpose only if the examined tissues differ significantly in their conductivities but this can only happen if the disease is in its final stages [8]. In addition, exposing the patient to a massive amount of radiation definitely has a bad impact on health.

1.2 Inverse geometric EIT problems

The EIT direct (forward) problem prescribes the current flux on the boundary, which in turn, leads to calculation of voltages via an estimated conductivity distribution based on Maxwell's equations. In contrast, the inverse EIT problem aims to evaluate the inner conductivity distribution and reconstruct an estimated image of the objects in the domain from the knowledge of the voltages for a wide pattern of injecting currents. In this problem, some part of the boundary must be identified, whilst the other part of the

boundary, the medium properties, the governing equation and the boundary conditions (over-determined conditions) are all available [37]. Due to the ill-posedness, which means a big change in the inner impedance may result in only a very small change in the boundary voltages and current flux, finding the solution of the EIT geometric problem is not an easy task. Additionally, in an EIT iterative optimization process, a nonlinear least-squares objective function has to be evaluated many times using a forward solver. Consequently, there is a need to obtain the solution of the direct problem accurately and fast if it is to be useful for real-time monitoring [31, 33, 55, 59].

Some comparison has been previously performed in [24] between the forward solutions of the finite volume method (FVM) and the finite element method (FEM) in terms of accuracy and stability, for the gap model of EIT. Also, very recently an improved boundary distributed source method has been compared in [37] with the more standard BEM and FEM numerical forward solvers for ERT.

1.3 The mathematical formulation of EIT

To model electromagnetic phenomena, we use Maxwell's equations which are given by

$$\bigtriangledown \times \underline{E} = -\partial_t \underline{B}, \qquad \text{(Faraday's law of induction)}, \tag{1.1}$$

$$\bigtriangledown \times \underline{H} = \underline{J} + \partial_t \underline{D}, \qquad \text{(Ampere's law of induction)}, \tag{1.2}$$

$$\bigtriangledown \cdot \underline{D} = \rho, \qquad \text{(Gauss's law of electric field)}, \tag{1.3}$$

$$\bigtriangledown \cdot \underline{B} = 0, \qquad \text{(Gauss's law of magnetic field)}, \tag{1.4}$$

where $\underline{E}$ is the electric field, $\underline{H}$ is the electric flux density, $\underline{B}$ is the magnetic field, $\underline{J}$ is the current density, $\underline{D}$ is the magnetic current density and ρ is the volume charge density, [19, 70].

There exist constitutive relationships linking the electric and magnetic flux densities

$\underline{D}$ and $\underline{B}$ along with the electric and magnetic fields $\underline{E}$ and $\underline{H}$. These relationships depend on the properties of the material and are given by

$$\underline{D} = \epsilon \, \underline{E}, \tag{1.5}$$

$$\underline{B} = \mu \, \underline{H}, \tag{1.6}$$

$$\underline{J} = \sigma \, \underline{E}, \tag{1.7}$$

where ϵ is the electric permittivity, μ the magnetic permeability and σ the conductivity, [8, 19, 70].

One way to obtain the differential equation for the interior of the body is by assuming that our experiments are static ones. This means that we can set the derivatives in (1.1) and (1.2), in respect to time, to be zero. Then, from (1.1) we conclude that there is a electric potential u such that

$$\underline{E} = - \bigtriangledown u. \tag{1.8}$$

Using equations (1.7), (1.8), as well as taking the divergence of (1.2), leads to the Laplace's conductivity equation which governs the electric potential u inside the domain Ω of the body,

$$\bigtriangledown \cdot (\sigma \bigtriangledown u) = 0 \quad \text{in} \quad \Omega. \tag{1.9}$$

The current density j is produced by injecting currents via electrodes which are attached to the surface $\partial\Omega$ of the object Ω. The resulting current density is specified as

$$\sigma \frac{\partial u}{\partial n} = j \quad \text{on} \quad \partial\Omega. \tag{1.10}$$

In [18], some mathematical models of the boundary conditions in ERT have been gradually developed to deduce the most suitable and general model. The most realistic

model takes into account the influences of restricting the current density values within a specific range, not ignoring the shunting effect of electrodes, and considering the electrochemical effect between the electrode and the object.

1.3.1 The continuous model

This model is formulated by equations (1.9) and (1.10) together with the following conditions:

$$\int_{\partial\Omega} j \, ds = 0 \qquad \text{(conservation of the charge)}, \tag{1.11}$$

$$\int_{\partial\Omega} u \, ds = 0 \qquad \text{(refering to the 'ground' or reference voltage)}. \tag{1.12}$$

Although the continuous model is commonly used, it is a poor EIT model for real experiments due to the lack of the current density values j in (1.10). In practice what is known, are only the currents that are sent down the wires attached to discrete electrodes, [8, 18, 19].

1.3.2 The gap model

This model is considered as an improvement of the continuous model. Herein, the current density is supposed to be non-zero and constant over each electrode and zero between any two adjacent electrodes (in the gaps). Mathematically, the L attached electrodes on the boundary are denoted by ε_p, for $p = \overline{1, L}$ and the condition (1.10) is modified as

$$\sigma \frac{\partial u}{\partial n} = \begin{cases} \frac{I_p}{\ell_p} & \text{on} \quad \varepsilon_p, \ p = \overline{1, L} \\ 0 & \text{on} \quad \partial\Omega \backslash \cup_{p=1}^{L} \varepsilon_p \end{cases} \tag{1.13}$$

where I_p is the current which is injected via electrode ε_p, and ℓ_p is the length or the area of electrode p. In addition, equation (1.11) can be rewritten in the form

$$\sum_{p=1}^{L} I_p = 0. \tag{1.14}$$

Considering the current density as a constant is an oversimplified assumption and not taking into account the shorting or shunting effect of the electrodes makes the gap model wholly inadequate in many practical EIT applications, [8, 18, 19].

1.3.3 The shunt model

In the previous two models, the resistivity of the medium is overestimated due to the ignorance of the shunting effect of electrodes. This defect is accounted for by the shunt electrode model because it is assumed that the metal electrodes are perfect conductors, therefore, the electric potential under each electrode is the same constant. As a result, equation (1.10) is replaced by

$$\int_{\varepsilon_p} \sigma \frac{\partial u}{\partial n} = I_p, \quad p = \overline{1, L}. \tag{1.15}$$

This is combined with

$$\sigma \frac{\partial u}{\partial n} = 0 \qquad \text{(in the gaps between electrodes)}. \tag{1.16}$$

Furthermore, in order to obtain the very high conductivity of electrodes, we assume that u is a constant on each electrode. These constants represent the measured voltages which take the form

$$u = U_p \qquad \text{on} \quad \varepsilon_p,\ p = \overline{1, L}. \tag{1.17}$$

For more details, see [8, 18, 19].

1.3.4 The complete model

Unfortunately, the shunt model does not reproduce the experimental data because it fails to consider the electrochemical effect between the electrode and the object. At the body-electrode interface there is a thin, highly resistive layer called the effective contact impedance or 'surface impedance' let us denote this quantity by z_p. This will then replace (1.17) by

$$u + z_p \sigma \frac{\partial u}{\partial n} = U_p \qquad \text{on} \quad \varepsilon_p,\ p = \overline{1, L}. \tag{1.18}$$

Now, the complete model or the shunt-plus-surface-impedance model consists of (1.9), (1.15) and (1.16), together with the conservation of charge law (1.14) and (1.12) which can be rewritten as

$$\sum_{p=1}^{L} U_p = 0. \tag{1.19}$$

Then this complete electrode model (CEM) has a unique solution, see [61] and Appendix A.

1.4 Data collection procedure

Two ways to collect the data for ERT problem are considered in the thesis. Either we inject a single current through the attached electrodes and calculate the potential and current flux at equally-spaced points on the outer boundary, or calculate the voltage measurements from equation (2.4) after we apply multiple current patterns when the CEM of ERT is solved in Chapters 3 and 4. Also, for the continuous model inverse

problem in three dimensions, which is considered in Chapter 5, the data is Cauchy data (the pair of boundary potential and current flux), see Figure 1.1. Throughout the thesis, both the potential and current flux are calculated at thirty equally-spaced points on the outer boundary, see Figure 1.1 (left), whilst the voltage values are calculated at L equally-spaced points on the outer boundary, see Figure 1.1 (right).

Figure 1.1: A sketch of the direct problem when $L = 4$ electrodes are attached: the blue dots show the inner and outer source points, the green object is known, and the red points show where the measurements are collected.

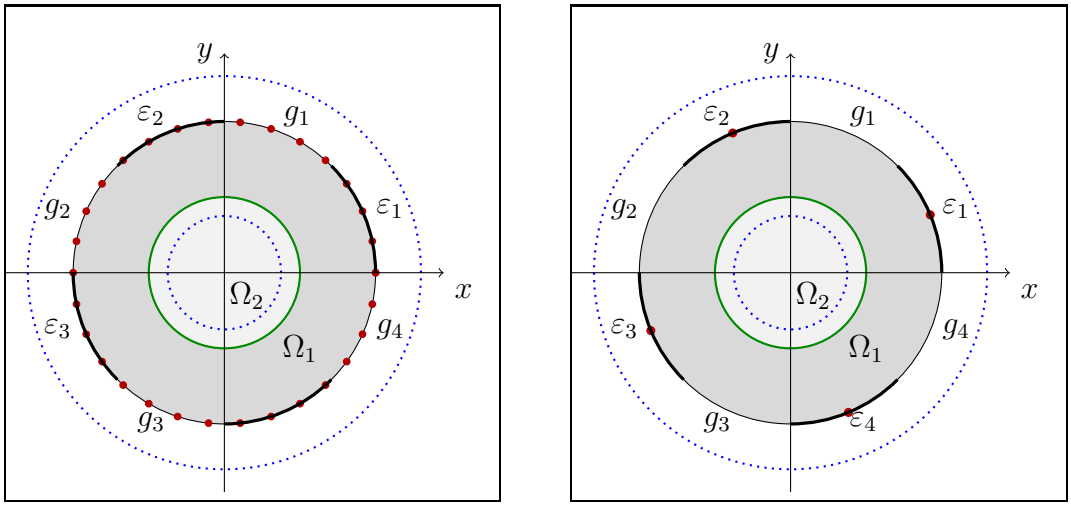

1.5 Bayesian statistical approach

The purpose behind using statistical techniques is to reformulate the inverse problem in the form of a statistical investigation (inference) in order to find a desirable reconstruction of the conductivity distribution based on ERT data. It is well known that the ERT inverse problem is both ill-posed and non-linear, and the Bayesian approach, linked to Markov chain Monte Carlo (MCMC) algorithms, works as a regularization scheme interpreted in terms of prior information, [58]. Modelling of the prior information is a very important process in order to achieve good knowledge about the problem's solution. Using the statistical framework allows the solution of the inverse problem

to be called the posterior distribution of the parameters of interest contingent on the measurements, for more details see [34]. This posterior distribution is obtained from a likelihood combined with a prior distribution using Bayes theorem, all the procedure is stated in section 1.5.1. MCMC offers a flexible tool to fully investigate the reliability and quantify uncertainty of that posterior distribution, but it makes intensive use of the forward solver which can be a big drawback especially when three-dimensional ERT problems are being solved. Hence, using the meshless Method of fundamental solutions (MFS) described in Chapter 2, is ideal. Section 1.5.2 provides a general background to the MCMC method.

1.5.1 Modelling of the ERT inverse problem

We shall solve the complete-electrode inverse model of ERT using the Bayesian approach and the MFS to detect an unknown object Ω_{Inner} (assumed star-shaped) contained in a domain Ω. The MFS coefficients $\underline{c} = (c_k)_{k=\overline{1,2M}}$, see (2.32) and the radii $\underline{r} = (r_i)_{i=\overline{1,M}}$, parameterising the star-shaped domain, see (3.12) and (3.13), must be estimated, [36, 37]. A sketch of the mathematical problem that is investigated throughout the thesis is shown in Figure 1.2.

Figure 1.2: A sketch of the inverse problem when $L = 4$ electrodes are attached: the red object is unknown, and the green points show the locations of the measurement data.

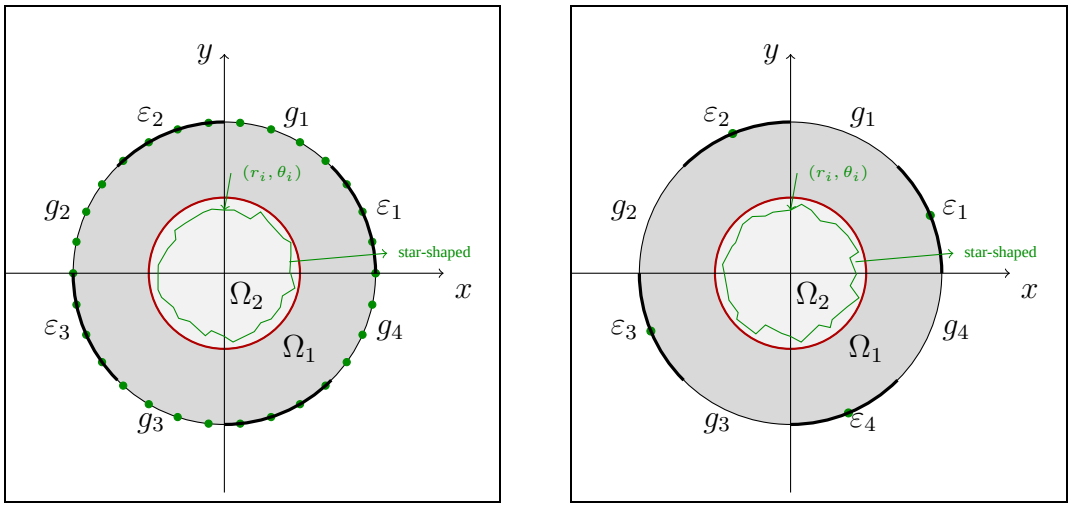

The following data model and its corresponding likelihood function, are used for all the numerical experiments in this thesis whatever the data set type, [2]. For example, let us consider the voltage data type $\mathbf{T}$ where the number of attached electrodes is equal to L allowing $(L-1)$ multiple current patterns. In this case, the data model merges two features of the measurements procedure. Firstly, the important relationship between the unknowns $\underline{r}$ and $\underline{c}$, and the voltage data is defined as the expectation of the voltage values (or the free-noise voltages) denoted by

$$E[\underline{T}|\underline{r}, \underline{c}] = \mu(\underline{r}, \underline{c}), \tag{1.20}$$

where $\mu(\underline{r}, \underline{c}) = U_p^i$, $p = \overline{1, L}$, $i = \overline{1, (L-1)}$ is obtained from the MFS forward solutions using equation (2.4) when the $(L-1)$-th current patterns defined in equations (3.27)-(3.33) are simultaneously applied. The total voltage data set is $\mu_(\underline{r}, \underline{c}) = (T_j)_{j=\overline{1,L(L-1)}}$. Secondly, a stochastic component which describes how the voltage data varies around their expected values is introduced as

$$\underline{T} = (T_j + \psi_j)_{j=\overline{1,L(L-1)}}, \tag{1.21}$$

where the additive noise variables ψ_j are assumed to follow independent Gaussian distributions with zero mean and variance σ_T^2, this leads to the likelihood defined in [2, 67], namely, $\underline{T}|\underline{r},\underline{c} \sim N((\mu(\underline{r},\underline{c}),\sigma_T^2 I)$ which has the density function

$$l(\underline{T}|\underline{r},\underline{c}) = (2\pi\sigma_T^2)^{-L(L-1)/2} \exp\left\{-\frac{1}{2\sigma_T^2}\left\|\underline{T}-\mu(\underline{r},\underline{c})\right\|^2\right\}, \quad \sigma_T > 0. \tag{1.22}$$

The main ingredients in the Bayesian statistical approach are the above defined likelihood function and a prior distribution, to be defined later, which describes the model parameters, $\underline{r}$ and $\underline{c}$ before the voltage data. A proportion of the likelihood function times the prior distribution (using Bayes theorem) leads to the posterior distribution, see Section 3.3.1 for more details.

1.5.2 Markov Chain Monte Carlo estimation

The aim of solving the inverse ERT problem is to reconstruct an image by estimating the unknown parameters (i.e. this set could be the radii of the star-shaped object and the MFS internal/external coefficients). For instance, when data measurements are $\underline{Y} = \{Y_j : j = 1, ..., n\}$ and the values of the unknowns are $\underline{X} = \{X_i : i = 1, ..., n\}$, the estimation is dependent on the posterior distribution

$$\pi(\underline{X}|\underline{Y}) = \frac{l(\underline{Y}|\underline{X})\pi(\underline{X})}{l(\underline{Y})}, \tag{1.23}$$

where $l(\underline{Y}|\underline{X})$ is a conditional distribution defined as the likelihood function and $\pi(\underline{X})$ is a prior distribution.

Equation (1.23) can be written as

$$\pi(\underline{X}|\underline{Y}) \propto l(\underline{Y}|\underline{X})\pi(\underline{X}), \tag{1.24}$$

since $l(\underline{Y})$ is not dependent on $\underline{X}$ and it does not play role in the estimation, [2].

In such inverse problems, the unknown parameter $\underline{X}$ is of high dimension making the posterior distribution complicated to be solved numerically using the standard regularization methods. At the same time, the analytical solution of the posterior problem is impossible. This is why the Markov chain Monte Carlo (MCMC) technique is used in this thesis to estimate the shape, size and location of the inner inclusion, as well as evaluating the constant contact impedance (CCI) values between the attached electrodes and the surface. Another advantage of using MCMC here is that it also allows deeper investigation of the posterior distribution in terms of accuracy and reliability by plotting histograms and credible intervals of the unknown parameters, more details are reported in Section 3.3.2.

1.6 Summary and outline of the thesis

In various applications of EIT, such as medical imaging or geophysics, the purpose is to evaluate the conductivity distribution within a domain. This means reconstructing the conductivity of the whole domain using some electrical measurements which are taken on the surface of the object (or body), [66]. This task can be achieved by attaching a finite number of electrodes to the outside boundary of the object. Then, currents are injected through the electrodes. The MFS is used to numerically simulate the boundary voltages of the complete-electrode direct model of ERT. In this process, we seek to determine an accurate solution because we lack the exact one for such complicated problems. Moreover, there are several advantages that make the MFS worth while. Firstly, it is a meshless scheme because only the boundary part of the domain needs to be collocated and no interior points are involved, [15, 37], unlike the FDM and FEM where the solution domain is discretised into internal cells and domain elements, respectively. Secondly, the MFS avoids any integral calculations whilst the boundary element method (BEM) does not. This advantage makes the MFS code not only eas-

ier to build in two dimensions comparing with the corresponding BEM code, but also for the three-dimensional case. Also, it can be easily implemented for irregular and complex geometries, [15, 38]. Thirdly, the MFS is a BEM-type method, so it shares its advantages over the FEM and FDM, [38]. Finally, it successfully deals with infinite domains by merging the behaviour of the resulting solutions into the fundamental solution of the governing equation, [38].

Using the voltages as a data set to estimate the interior conductivity distribution results in an ill-posed inverse problem, which needs to be regularized to obtain a stable and reliable solution. The Bayesian process is an explicit statistical approach which aims to determinate, interpret and reconstruct images from data using probability models. Also, this approach allows to assess the reliability and uncertainty for the unknowns by plotting the credibility intervals and the circular histograms for each sampled parameter, [28].

After introducing some background and fundamental concepts of this work, Chapter 2 begins with the mathematical formulation of the complete-electrode model (CEM) for ERT. Since in the direct problem of the CEM the constant voltage on each electrode is unknown, we can eliminate it by integrating the associated Robin boundary condition, as described in [22]. The resulting mathematical model is then solved using two numerical methods. These are the BEM and, for the first time, the meshless MFS. In the same spirit as [36], we compare thoroughly the numerical results obtained by these two methods for both simply-connected and multiply-connected domains containing a rigid inclusion or a cavity. An extension to composite bi-materials is also performed afterwards. Finally, Section 2.8 highlights the conclusions of Chapter 2 paving the way for of solving the inverse problem of ERT/EIT in the next chapter.

In Chapter 3, we are interested in identifying the size and shape of the inner inclusion. This means to approximate an image of the piecewise constant electrical conductivity distribution within the inclusion. So, we find the solution of the complete-electrode inverse model of ERT using the Bayesian approach and the MFS. Some examples using simulated experiments are examined to demonstrate the effectiveness of

the proposed statistical procedures.

In Chapter 4, we are interested in solving the inverse problem of CEM of ERT in an annular domain containing rigid inclusions that have unknown centres, this means detecting the locations of those inner objects besides their sizes and shapes. Firstly, we assume that we have only one rigid inclusion in the annular domain which has unknown centre needing to be estimated from noisy data. This data is represented by the boundary voltages obtained analytically or by solving numerically the direct problem using the MFS and are corrupted by some Gaussian random noise. The simulated data are inverted using the MCMC method to produce a reconstruction of the inner object. We find simultaneously the unknown centre and the CCI values between the attached electrodes and the outer surface. In addition, we extend the work to identify two inclusions having unknowns centres.

In Chapter 5, we extend our work to the three-dimensional EIT problem and, for simplicity, we consider solving the direct and inverse continuous model problems of ERT. In the first part of the chapter, we apply the MFS to find forward solutions of three-dimensional Laplace's equation subject to Dirichlet boundary conditions with or without an inclusion and we compare the obtained results of the interior solutions and the boundary derivative with the exact ones in cases where an analytical solution is available. Then, we use the MFS to find the numerical normal derivative on the outer boundary when the number of the rigid inclusions is extended to two. Next, we preform some numerical simulations and consider the same technique that combines the MCMC with the MFS to solve the inverse problems.

Finally, the conclusions of the thesis and further work are presented in Chapter 6.

Chapter 2

Solving the complete-electrode model of direct ERT

2.1 Introduction

The EIT direct (forward) problem involves the calculation of voltages, based on a given conductivity distribution. In contrast, the inverse EIT problem aims to reconstruct the inner conductivity distribution from knowledge of the voltages from set of injected current patterns. In the proposed iterative optimization process, the nonlinear least-squares objective function has to be evaluated many times using the forward solver. Consequently, there is a need to obtain the solution of the direct problem accurately and fast, [31, 33, 55, 59].

Some comparison has been previously performed in [24] between the finite volume method (FVM) and the finite element method (FEM), for the gap model of EIT. Also, very recently an improved boundary distributed source method has been compared in [33] with the more standard boundary element method (BEM) and FEM numerical forward solvers for ERT.

We begin with the mathematical formulation (Section 2.1) which describes the complete-electrode model (CEM) for ERT. Since in the direct problem of the CEM the

constant voltage on each electrode is unknown, we can eliminate it by integrating the associated Robin boundary condition, as described in [22]. The resulting mathematical model is then solved using two numerical methods. These are BEM (Section 2.3) and, for the first time, the meshless method of fundamental solutions (MFS) (Section 2.4). In the same spirit as [33], we compare thoroughly the numerical results obtained by these two methods for both simply-connected (Section 2.5) and multiply-connected domains containing a rigid inclusion or a cavity (Section 2.6). An extension to composite bi-materials is also performed in Section 2.7. Finally, conclusions are given in Section 2.8 paving the way for solving the inverse problem of ERT/EIT in subsequent chapters of the thesis.

2.2 Mathematical formulation

In this section, we consider Laplace's equation in a (two-dimensional) bounded domain Ω, namely,

$$\bigtriangledown^2 u = 0, \qquad \text{in } \Omega, \tag{2.1}$$

subject to certain boundary conditions which make the problem the so-called 'complete-electrode model' (CEM), [61]. In this model, on the boundary $\partial\Omega$ there are attached L electrodes, ε_p, for $p = \overline{1, L}$, see Figure 2.1.

Figure 2.1: The two-dimensional CEM, for $L = 2$ and 4 electrodes.

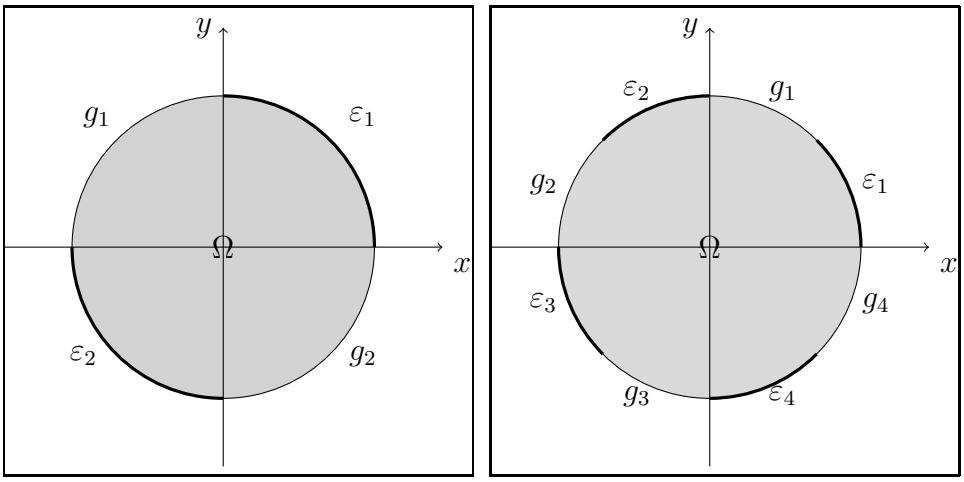

On these electrodes we have the Robin boundary condition, [22],

$$u + z_p \frac{\partial u}{\partial n} - \frac{1}{\ell_p} \int_{\varepsilon_p} u \, ds = \frac{z_p I_p}{\ell_p}, \qquad \text{on } \varepsilon_p, \;\; p = \overline{1, L}, \tag{2.2}$$

where $\underline{n}$ is the outward unit normal to the boundary $\partial\Omega$, $\frac{\partial}{\partial n} = \bigtriangledown \cdot \underline{n}$, ℓ_p is the length of the electrode ε_p and

$$I_p = \int_{\varepsilon_p} \frac{\partial u}{\partial n} \, ds \tag{2.3}$$

is the injected constant current applied on the electrode ε_p and satisfying $\sum_{p=1}^{L} I_p = 0$, and $z_p > 0$ is the constant contact impedance. In equations (2.1)-(2.3) we have assumed that the medium Ω has unit constant conductivity, but later on we shall also consider a piecewise constant version.

The derivation of the boundary condition (2.2) is as follows. The constant voltages U_p on the electrodes ε_p, that are to be determined in the direct problem, are calculated in the inverse problem from the Robin boundary condition

$$u + z_p \frac{\partial u}{\partial n} = U_p, \qquad \text{on } \varepsilon_p, \;\; p = \overline{1, L}. \tag{2.4}$$

Then, by integrating (2.4) over ε_p, and using (2.3) we can eliminate the unknown U_p

to obtain (2.2).

The electric current is assumed to vanish on the gaps, g_p for $p = \overline{1, L}$, between the electrodes on the boundary part, so that

$$\frac{\partial u}{\partial n} = 0, \qquad \text{on } \partial\Omega \backslash \cup_{p=1}^{L} \varepsilon_p =: \cup_{p=1}^{L} g_p. \tag{2.5}$$

In order to obtain a unique solution we also need that, [5],

$$\int_{\partial\Omega} u \, ds = 0. \tag{2.6}$$

Equations (2.1), (2.2), (2.5) and (2.6) represent the direct problem of ERT if the domain Ω is simply-connected. If Ω is multiply-connected, e.g. it contains holes, then an additional boundary condition of the form

$$u = 0, \quad \text{or} \quad \frac{\partial u}{\partial n} = 0, \quad \text{or} \quad z\frac{\partial u}{\partial n} + u = 0 \tag{2.7}$$

should be applied on the inner boundary portions of $\partial\Omega$, where $z \geq 0$ is a contact impedance.

The CEM given by equations (2.1), (2.3)-(2.6) is uniquely solvable, [61], and has been validated in [18] as being in most agreement with experiments compared with the simpler continuous, gap and shunt models of ERT/EIT.

Without loss of generality, we can assume that Ω is the unit disk $\{(x, y) \in \mathbb{R}^2 | x^2 + y^2 < 1\}$, otherwise we can always conformal a map from any the simply-connected domain Ω onto the unit disk, [35].

A closed form solution of the direct problem of ERT is available only in very restricted cases, e.g. for $L = 2$ electrodes and no contact impedances $z_1 = z_2 = 0$, [51], and therefore numerical methods are generally necessary. In the next sections we describe and compare two such numerical methods.

2.3 The boundary element method

The BEM has many advantages compared to other domain discretisation methods because it discretises only the boundary to obtain the unspecified boundary data and the solution in the whole domain, [3, 41]. This reduction makes the number of unknowns, which need to be determined, smaller in comparison with domain discretisation methods such as the FDM or FEM.

In this section, we will use the BEM to solve the forward problem (2.1), (2.2), (2.5) and (2.6) in the unit disk $\Omega = \{(x, y) \in \mathbb{R}^2 | x^2 + y^2 < 1\}$. The BEM reduces the problem to one of solving the linear system of equations

$$A\underline{u'} + B\underline{u} = \underline{0}, \tag{2.8}$$

where $\underline{u} := u\left(\underline{\tilde{p}}_j\right)_{j=\overline{1,M}}$, $\underline{u'} := \frac{\partial u}{\partial n}\left(\underline{\tilde{p}}_j\right)_{j=\overline{1,M}}$, A and B are matrices which depend solely on the geometry of $\partial\Omega$, and M is the number of boundary elements. The boundary element endpoint is $\underline{p}_j = (x_j, y_j) = \left(\cos\left(\frac{2\pi j}{M}\right), \sin\left(\frac{2\pi j}{M}\right)\right)$ for $j = \overline{1, M}$, with the convention that $\underline{p}_0 = \underline{p}_M$ and $\underline{\tilde{p}}_j$ is the boundary element node. For a constant BEM approximation, $\underline{\tilde{p}}_j$ is the midpoint of the segment $\Gamma_j = \overline{\underline{p}_{j-1}, \underline{p}_j}$. The derivation of this approximation can be briefly summarised in the following four steps:

(i) Find the fundamental solution $G(\underline{p}, \underline{p'})$ of Laplace's equation satisfying

$$\bigtriangledown^2 G(\underline{p}, \underline{p'}) = -\delta(\underline{p} - \underline{p'}),$$

where δ is the Dirac delta function. The fundamental solution which we seek is based on the distance between $\underline{p}$ and $\underline{p'}$. As a result, in two-dimensions

$$G(\underline{p}, \underline{p'}) = -\frac{1}{2\pi} \ln |\underline{p} - \underline{p'}| = -\frac{1}{2\pi} \ln \sqrt{(x - x')^2 + (y - y')^2}, \tag{2.9}$$

where $\underline{p} = (x, y)$ and $\underline{p'} = (x', y')$.

(ii) Transform Laplace's equation into the integral equation

$$\eta(\underline{p})u(\underline{p}) = \int_{\partial\Omega} \left[G(\underline{p},\underline{p}')\frac{\partial u}{\partial n} - u(\underline{p}')\frac{\partial G}{\partial n}(\underline{p},\underline{p}') \right] dS, \tag{2.10}$$

where

$$\eta(\underline{p}) \;=\; \begin{cases} 0.5 & \text{if} \quad \underline{p} \in \partial\Omega \quad \text{(smooth)}, \\ 1 & \text{if} \quad \underline{p} \in \Omega, \\ 0 & \text{if} \quad \underline{p} \notin \overline{\Omega}, \end{cases}$$

This is obtained using the fundamental solution (2.9) and Green's identity.

(iii) Discretise the boundary into small straight line segments Γ_j for $j = \overline{1, M}$ and assume that the boundary potential u and its normal derivative $\frac{\partial u}{\partial n}$ are approximated by constant functions over each small boundary element Γ_j. Via these approximations, the integral equation (2.10) is expressed as

$$\eta(\underline{p})u(\underline{p}) = \sum_{j=1}^{M} u_j' A_j(\underline{p}) - \sum_{j=1}^{M} u_j B_j(\underline{p}), \tag{2.11}$$

where

$$A_j(\underline{p}) = \int_{\Gamma_j} G(\underline{p},\underline{p}')d\Gamma_j(\underline{p}')$$

$$= -\frac{1}{2\pi} \begin{cases} h(\ln(h/2) - 1) & \text{if } ab = 0, \\ a\cos(\beta)(\ln(a) - \ln(b)) - h(1 - \ln(b)) + a\psi\sin(\beta) & \text{if } ab \neq 0 \end{cases}$$

$$B_j(\underline{p}) = \int_{\Gamma_j} \frac{\partial G}{\partial n}(\underline{p}, \underline{p}')d\Gamma_j(\underline{p}')$$

$$= \frac{1}{2\pi}\begin{cases} 0 & \text{if} \quad ab = 0 \text{ or } \underline{p} \in \{\underline{p}_{j-1}, \underline{p}_j\} \\ \psi \text{ sign}(\alpha_{j-1}(\underline{p}) - \alpha_j(\underline{p})) & \text{if} \quad y \in [y_{j-1}, y_j], \\ \psi \text{ sign}(\alpha_j(\underline{p}) - \alpha_{j-1}(\underline{p})) & \text{otherwise} \end{cases}$$

where sign is the signum function, $a = |\underline{p} - \underline{p}_{j-1}|$, $b = |\underline{p} - \underline{p}_j|$, $h = |\underline{p}_j - \underline{p}_{j-1}|$, $\alpha_{j-1}(\underline{p})$ and $\alpha_j(\underline{p})$ are the angles between the x-axis and segments $\overline{\underline{p}, \underline{p}_{j-1}}$ and $\overline{\underline{p}, \underline{p}_j}$, respectively, and the angles ψ and β are given by

$$\psi = \arccos\left(\frac{a^2 + b^2 - h^2}{2ab}\right), \quad \beta = \arccos\left(\frac{a^2 + h^2 - b^2}{2ah}\right).$$

(iv) Apply equation (2.11) at the midpoint nodes $\tilde{p}_i$ for $i = \overline{1, M}$. This gives the system of linear algebraic equations (2.8) with the unknowns $\underline{u}$ and $\underline{u}'$. The system can be rewritten as

$$\sum_{j=1}^{M} (A_{ij}u'_i + B_{ij}u_i) = \underline{0}, \quad i = \overline{1, M}, \tag{2.12}$$

where A and B are matrices defined by

$$A_{ij} = A_j(\underline{\tilde{p}_i}), \;\; B_{ij} = -B_j(\underline{\tilde{p}_i}) - \frac{1}{2}\delta_{ij},$$

where δ_{ij} is the Kronecker delta function.

In compact form, (2.12) represents the system of equations (2.8). Specific boundary conditions must be imposed to make the resulting system of equations (2.12) solvable. The CEM boundary conditions (2.2), (2.5) and (2.6) will be considered next.

First, we collocate the boundary condition (2.2) for the electrodes ε_p, $p = \overline{1, L}$, at

the nodes $\tilde{p}_i$, resulting in

$$u_i + z_p u'_i - \frac{2\pi}{M\ell_p} \sum_{k=(KM/L)+1}^{(2K+1)M/(2L)} u_k = \frac{z_p I_p}{\ell_p},$$
$$i = \overline{(M+1+KM/L), (M+(2K+1)M/(2L))}, \quad (2.13)$$

where $K = \overline{0, (L-1)}$. This yields $\frac{M}{2}$ equations.

Secondly, by collocating the zero flux boundary condition (2.5) for the gaps g_p, $p = \overline{1, L}$, between electrodes at the nodes $\tilde{p}_i$, we obtain

$$u'_i = 0, \qquad i = \overline{(M+1+(2K-1)M/(2L)), (M+KM/L)}, \quad (2.14)$$

where $K = \overline{1, L}$. This yields another $\frac{M}{2}$ equations.

Finally, the condition (2.6) yields one more equation, namely,

$$\sum_{k=1}^{M} u_k = 0. \quad (2.15)$$

To find the solution of the CEM problem (2.1), (2.2), (2.5) and (2.6) using the BEM, the equations (2.12)-(2.15) have been reformulated in the following generic matrix form as a $(2M+1) \times (2M)$ linear system of algebraic equations:

$$D\underline{X} = \underline{b}, \quad (2.16)$$

where

$$\underline{X} = \begin{pmatrix} \underline{u} \\ \underline{u'} \end{pmatrix}.$$

Of course, from equations (2.13) and (2.14), in principle we could eliminate the current flux $\underline{u}'$ such that (2.16) can be reduced to a smaller $(M+1) \times M$ linear system of algebraic equations. Since the system of equations (2.16) is over-determined (the num-

ber of equations is greater than the number of unknowns), we can use the least-squares method to solve it. This yields

$$\underline{X} = (D^T D)^{-1} D^T \underline{b}. \tag{2.17}$$

Once the boundary values have been obtained accurately, equation (2.11) can be applied at $\underline{p} \in \Omega$ to provide explicitly the interior solution for $u(\underline{p})$.

2.4 The method of fundamental solutions

One of the reasons why the method of fundamental solutions (MFS) is becoming increasingly popular in various applications is that it is conceptually simple and easy to describe and implement. The MFS is regarded as a meshless BEM and it has been used to find the solution of inverse geometric problems governed by Laplace's equation in [35, 36].

The MFS seeks a solution of Laplace's equation (2.1) as a linear combination of fundamental solutions of the form:

$$u(\underline{p}) = \sum_{j=1}^{N} c_j G(\underline{\xi}_j, \underline{p}), \qquad \underline{p} \in \overline{\Omega} = \Omega \cup \partial\Omega, \tag{2.18}$$

where $\underline{\xi}_j$ are called sources ('singulaties') and are located outside $\overline{\Omega}$, and $(c_j)_{j=\overline{1,N}}$ are unknown coefficients to be determined by imposing the boundary conditions (2.2), (2.5) and (2.6). The approximation (2.18) is justified by the denseness of the set of these functions, as $N \to \infty$, into the set of harmonic functions, see [14, 60] and Appendix A. Note that in $\mathbb{R}^2$ there is an additional constant which has to be included in the expression (2.18) in order for the set to be complete, but this constant can usually be taken to be zero without much loss of generality.

Since Ω is the unit disk, we take the source points

$$\underline{\xi}_j = (\xi_j^1, \xi_j^2) = \left(R\cos\left(\frac{2\pi j}{N}\right), R\sin\left(\frac{2\pi j}{N}\right)\right), \quad j = \overline{1, N},$$

where $1 < R < \infty$, and the boundary collocation points

$$\underline{x}_i = \left(\cos\left(\frac{2\pi i}{M}\right), \sin\left(\frac{2\pi i}{M}\right)\right), \quad i = \overline{1, M}.$$

From (2.9) we have

$$\frac{\partial G}{\partial n}(\underline{\xi}_j, \underline{p}) = \frac{1 - (\xi_j^1 x + \xi_j^2 y)}{2\pi|\underline{\xi}_j - \underline{p}|^2}, \qquad \underline{p} = (x, y) \in \partial\Omega, \tag{2.19}$$

where $\underline{\xi}_j = (\xi_j^1, \xi_j^2)$. In order to obtain the coefficient vector $\underline{c} = (c_j)_{j=\overline{1,N}}$, we substitute equations (2.9) and (2.19) into the boundary conditions (2.2), (2.5) and (2.6).

Firstly, we apply the boundary condition (2.2) for the electrodes ε_p, $p = \overline{1, L}$, at the collocation points $\underline{x}_i$ on ε_p resulting in

$$\sum_{j=1}^{N}\left[G(\underline{\xi}_j, \underline{x}_i) - \frac{2\pi}{M\ell_p}\sum_{k=(KM/L)+1}^{(2K+1)M/(2L)} G(\underline{\xi}_j, \underline{x}_k) + z_p\frac{\partial G}{\partial r}(\underline{\xi}_j, \underline{x}_i)\right] c_j = \frac{z_p I_p}{\ell_p},$$
$$i = \overline{(KM/L) + 1, (2K + 1)M/(2L)}, \tag{2.20}$$

where $K = \overline{0, (L - 1)}$. This yields $\frac{M}{2}$ equations.

Secondly, by applying the zero flux boundary condition (2.5) on the gaps $g_p, p = \overline{1, L}$, between electrodes, at the collocation points $\underline{x}_i$ on g_p, we obtain

$$\sum_{j=1}^{N} c_j\frac{\partial G}{\partial r}(\underline{\xi}_j, \underline{x}_i) = 0, \quad i = \overline{(1 + (2K - 1)M/(2L)), (KM/L)}, \tag{2.21}$$

where $K = \overline{1, L}$. This yields another $\frac{M}{2}$ equations.

Finally, imposing the condition (2.6) yields one more equation

$$\sum_{i=1}^{M} \sum_{j=1}^{N} c_j G(\underline{\xi}_j, \underline{x}_i) = 0. \tag{2.22}$$

Again, to find the solution of the CEM problem (2.1), (2.2), (2.5) and (2.6) using the MFS, the equations (2.20)-(2.22) have been reformulated in the following generic matrix form as an $(M + 1) \times N$ linear system of algebraic equations

$$F\underline{c} = \underline{b}. \tag{2.23}$$

The least-squares method is used to solve the system of equations (2.23) if $M+1 \geq N$. This yields

$$\underline{c} = \left(F^T F\right)^{-1} F^T \underline{b}. \tag{2.24}$$

Once the coefficient vector $\underline{c}$ has been obtained accurately, equations (2.18) and (2.19) provide explicitly the solution for the potential u in $\overline{\Omega}$, and the current flux $\partial u/\partial n$ on $\partial\Omega$.

2.5 Numerical results and discussion

In this section, we will discuss and compare the numerical solutions of the direct ERT problem given by equations (2.1), (2.2), (2.5) and (2.6) obtained using the BEM and the MFS.

Example 1. For simplicity, choose $L = 2$ (only two electrodes which are attached to the boundary) and solve the problem (2.1), (2.2), (2.5) and (2.6) with the following input data: $z_1 = z_2 = I_1 = 1$, and $I_2 = -1$.

BEM Solution: The matrix D in equation (2.16) is given by

$$D_{i,l} = \begin{cases} B_{i,l} & \text{if } l = \overline{1, M}, \\ A_{i,l} & \text{if } l = \overline{(M+1), 2M}, \end{cases} \quad i = \overline{1, M}.$$

Using equations (2.13)- (2.15) we obtain

$$D_{i,l} = \begin{cases} -\frac{h}{\ell_1} & \text{if } (i-M) \neq l, l = \overline{1, M/4}, \\ (1 - \frac{h}{\ell_1}) & \text{if } (i-M) = l, l = \overline{1, M/4}, \\ 0 & \text{if } l = \overline{(M/4+1), M}, \\ z_1 \delta_{i,l} & \text{if } l = \overline{(M+1), 2M}, \end{cases} \quad i = \overline{(M+1), (M+M/4)},$$

$$D_{i,l} = \begin{cases} -\frac{h}{\ell_2} & \text{if } (i-M) \neq l, l = \overline{(M/2+1), 3M/4}, \\ (1 - \frac{h}{\ell_2}) & \text{if } (i-M) = l, l = \overline{(M/2+1), 3M/4}, \\ 0 & \text{if } l = \overline{1, M/2} \cup \overline{(3M/4+1), M}, \\ z_2 \delta_{i,l} & \text{if } l = \overline{(M+1), 2M}, \end{cases}$$

$$i = \overline{(M + M/2 + 1), (M + 3M/4)},$$

$$D_{i,l} = \delta_{i,l}, \quad l = \overline{(M+1), 2M},$$

$$i = \overline{(M + M/4 + 1), (M + M/2)} \cup \overline{(M + 3M/4 + 1), 2M}.$$

The last row in the matrix D is given by

$$D_{(2M+1),l} = \begin{cases} 1 & \text{if } l = \overline{1, M}, \\ 0 & \text{if } l = \overline{M+1, 2M}. \end{cases}$$

Finally, the vector $\underline{b}$ is given by

$$\underline{b} = \left(\underline{0} \quad \frac{z_1 I_1}{\ell_1} \quad \underline{0} \quad \frac{z_2 I_2}{\ell_2} \quad \underline{0} \quad 0 \right)^T.$$

Table 1 illustrates the numerical solution of the direct problem (2.1), (2.2), (2.5)

and (2.6) obtained using the BEM with various numbers of boundary elements M. We only show the solution in the upper semi-disk because the solution is symmetric on the lower semi-disk, namely $u(x, y) = u(-x, -y)$ for $x \in (-1, 1), y \in (0, 1)$. Also, in Table 2.1 (as well as Tables 2.2 and 2.4 later on) we only show, for simplicity of illustration, the results at $r \in \{1, 2, 3, 9\}/10$. We mention that the numerical results for the other values of $r \in \{4, ..., 8\}/10$ have been found to possess similar features and therefore are not included. From Table 2.1 it can be seen that using the BEM to solve the CEM yields a convergent interior solution up to four decimal places, as the number of boundary elements M increases.

Table 2.1: The numerical solution of Example 1 at selected interior points (r, θ) obtained using the BEM for various numbers of boundary elements $M \in \{8, 16, 32, 64, 128, 256\}$.

r \ θ	$2\pi/10$	$4\pi/10$	$6\pi/10$	$8\pi/10$	$10\pi/10$	M
	0.0540	0.0487	0.0247	-0.0085	-0.0386	8
	0.0556	0.0502	0.0255	-0.0088	-0.0398	16
$1/10$	0.0561	0.0508	0.0257	-0.0088	-0.0401	32
	0.0562	0.0506	0.0257	-0.0089	-0.0401	64
	0.0562	0.0506	0.0257	-0.0089	-0.0402	128
	0.0562	0.0507	0.0258	-0.0089	-0.0402	256
	0.1083	0.974	0.0491	-0.0169	-0.0769	8
	0.1116	0.1004	0.0517	-0.0174	-0.0793	16
$2/10$	0.1124	0.1011	0.0511	-0.0175	-0.0799	32
	0.1126	0.1013	0.0511	-0.0176	-0.0800	64
	0.1126	0.1014	0.0512	-0.0176	-0.0801	128
	0.1127	0.1014	0.0512	-0.0176	-0.0801	256
	0.1632	0.1463	0.0727	-0.0248	-0.1147	8
	0.1681	0.1508	0.0751	-0.0257	-0.1184	16
$3/10$	0.1693	0.1519	0.0757	-0.0259	-0.1193	32
	0.1696	0.1521	0.0759	-0.0260	-0.1195	64
	0.1697	0.1522	0.0759	-0.0260	-0.1196	128
	0.1697	0.1522	0.0759	-0.0260	-0.1196	256
...	...	...	...	...	...	...
	0.5051	0.4723	0.1592	-0.0734	-0.3175	8
	0.5264	0.4774	0.1793	-0.0565	-0.3440	16
$9/10$	0.5264	0.4774	0.1793	-0.0565	-0.3440	32
	0.5263	0.4772	0.1792	-0.0564	-0.3436	64
	0.5264	0.4774	0.1793	-0.0565	-0.3439	128
	0.5264	0.4774	0.1793	-0.0565	-0.3440	256

Figures 2.2 and 2.3 show the BEM boundary solution for u and its normal derivative $\partial u/\partial n$, respectively. From these figures it can be seen that the BEM solutions for both u and $\partial u/\partial n$ have rapid convergence on the boundary. So, we can rely on these results and consider them as the ‘exact solution‘ of the well-posed direct problem of the CEM of EIT.

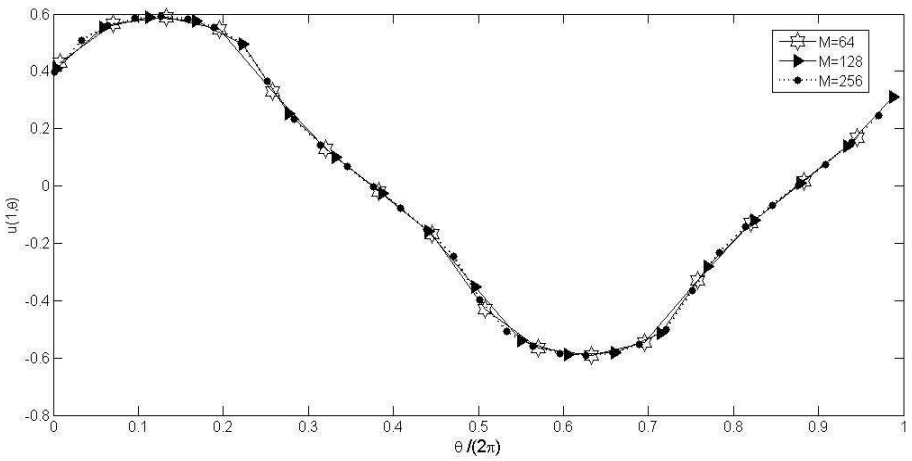

Figure 2.2: The boundary solution $u(1,\theta)$, as a function of $\theta/(2\pi)$, obtained using the BEM with $M \in \{64, 128, 256\}$, for Example 1.

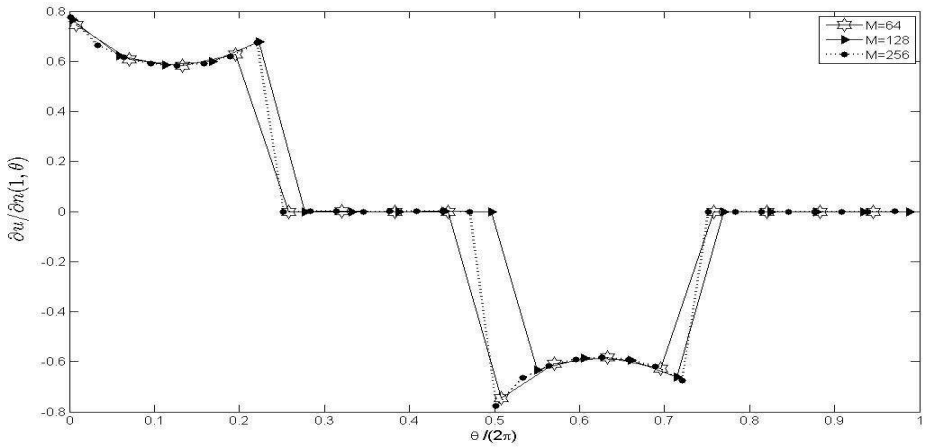

Figure 2.3: The normal derivative $\frac{\partial u}{\partial n}(1,\theta)$, as a function of $\theta/(2\pi)$, obtained using the BEM with $M \in \{64, 128, 256\}$, for Example 1.

Figure 2.4 shows the resulting voltages U_p, $p = 1, 2$, obtained from equation (2.4). In this figure the top part illustrates that the voltage is indeed constant and equal to $U_1 \approx 1.1738$, whilst the bottom one indicates that $U_2 \approx -1.1738$.

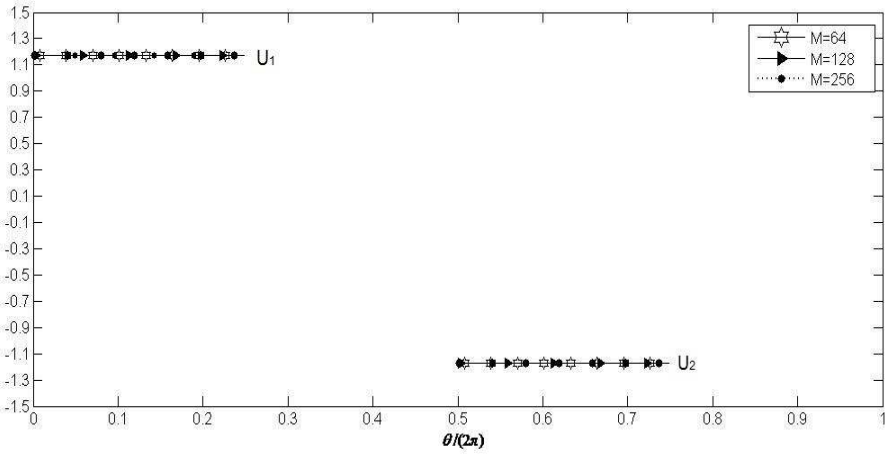

Figure 2.4: The voltages U_p, $p = 1, 2$, as functions of $\theta/(2\pi)$, obtained using the BEM with $M \in \{64, 128, 256\}$, for Example 1.

MFS solution: We now solve the problem (2.1), (2.2), (2.5) and (2.6) for Example 1 using the MFS instead of the BEM.

To begin with, the first $M/4$ rows of the matrix F in equation (2.23), corresponding to the first electrode ε_1, are

$$F_{i,j} = G_{i,j} - \frac{2\pi}{M\ell_1}\left(G_{i,j} + G_{i+1,j} + ... + G_{M/4,j}\right) + z_1 G'_{i,j}, \;\; i = \overline{1, M/4}, \;\; j = \overline{1, N},$$

where $G_{i,j} = G(\xi_j, x_i)$ and $G'_{i,j} = \frac{\partial G}{\partial n}(\xi_j, x_i)$. Another $\frac{M}{4}$ rows in the matrix F are generated by applying the boundary condition (2.20) on the second electrode ε_2, namely

$$F_{i,j} = G_{i,j} - \frac{2\pi}{M\ell_2}\left(G_{(M/2+1),j} + G_{(M/2+2),j} + ... + G_{3M/4,j}\right) + z_2 G'_{i,j},$$

$$i = \overline{(M/2+1), 3M/4}, \;\; j = \overline{1, N}.$$

In addition, applying the no flux boundary condition (2.21) results in another $\frac{M}{2}$ rows given by

$$F_{i,j} = G'_{i,j}, \;\; i = \overline{(M/4+1), M/2} \cup \overline{(3M/4+1), M}, \;\; j = \overline{1, N}.$$

To end with, the last row in the matrix F obtained from the condition (2.22) is:

$$F_{(M+1),j} = \sum_{i=1}^{M} G_{i,j}, \quad j = \overline{1, N}.$$

Similarly, the vector $\underline{b}$ of the linear system of equations (2.23) is given by

$$\underline{b} = \left(\frac{z_1 I_1}{\ell_1} \quad \underline{0} \quad \frac{z_2 I_2}{\ell_2} \quad \underline{0} \quad 0 \right)^T.$$

Table 2.2 illustrates the numerical solution of the problem (2.1), (2.2), (2.5) and (2.6) obtained using the MFS with various $M = N$ and $R = 1.15$. From this table it can be seen that using the MFS to solve the CEM provides a convergent interior solution up to four decimal places. However, by inspecting Tables 2.1 and 2.2 it can be seen that this convergence is slightly slower in the MFS than in the BEM, as $M = N$ increases.

Table 2.2: The numerical solution of Example 1 at selected interior points (r, θ) obtained using the MFS for various $M = N \in \{8, 16, 32, 64, 128, 256\}$ and $R = 1.15$.

r \ θ	$2\pi/10$	$4\pi/10$	$6\pi/10$	$8\pi/10$	$10\pi/10$	M
	0.1316	0.1225	0.0619	-0.0213	-0.0968	8
	0.0731	0.0658	0.0334	-0.0115	-0.0227	16
$1/10$	0.0578	0.0521	0.0265	-0.0091	-0.0413	32
	0.0562	0.0507	0.0257	-0.0088	-0.0401	64
	0.0562	0.0506	0.0257	-0.0088	-0.0401	128
	0.0561	0.0506	0.0257	-0.0088	-0.0401	256
	0.1466	0.1318	0.0664	-0.0227	-0.1040	8
	0.2740	0.2457	0.1216	-0.0422	-0.1909	16
$2/10$	0.1160	0.1043	0.0526	-0.0180	-0.0824	32
	0.1127	0.1014	0.0512	-0.0175	-0.0801	64
	0.1126	0.1013	0.0511	-0.0175	-0.0801	128
	0.1126	0.1013	0.0511	-0.0175	-0.0800	256
	0.4144	0.3704	0.1777	-0.0422	-0.1909	8
	0.2210	0.1981	0.0982	-0.0335	-0.1552	16
$3/10$	0.1747	0.1567	0.0781	-0.0267	-0.1230	32
	0.1698	0.1523	0.0759	-0.0259	-0.1197	64
	0.1697	0.1522	0.0759	-0.0259	-0.1196	128
	0.1696	0.1522	0.0759	-0.0259	-0.1195	256
...	...	...	...	...	...	...
	1.2972	1.1393	0.4321	-0.4131	-0.1860	8
	0.9671	0.5922	0.1302	-0.0360	-0.3042	16
$9/10$	0.5478	0.4905	0.1825	-0.0572	-0.3505	32
	0.5270	0.4783	0.1791	-0.0564	-0.3439	64
	0.5265	0.4775	0.1792	-0.0564	-0.3439	128
	0.5263	0.4773	0.1792	-0.0564	-0.3437	256

Figures 2.5 and 2.6 show comparisons between the BEM and MFS solutions for the boundary data $u(1, \theta)$ and $\partial u/\partial n(1, \theta)$, respectively. In these figures the markers are shown only on a coarse selection of boundary points in order to allow the curves to be distinguishable. In the MFS, we present the results obtained with $R = 1.15$ which is the choice for which the numerical MFS results are closest to the BEM results. In the absence of the BEM numerical results, or of an analytical solution, one could still optimize the choice of R by minimizing (with respect to R) the error in

a least-squares sense, in the boundary conditions (2.2), (2.5) and (2.6) at points on the boundary different to the collocation points $(\underline{x}_i)_{i=\overline{1,M}}$. The reason why R is close to unity is because the boundary value problem possesses singularities in the normal derivative, see Figure 2.5, at the end points of the electrodes where the Robin boundary condition (2.3) and the Neumann boundary condition (2.5) mix. This in turn means that the harmonic solution u cannot be analytically continued too far outside the unit disk Ω and the MFS approximation (2.18) is accurate only provided that the sources $(\underline{\xi}_j)_{j=\overline{1,N}}$ are positioned on a circle of radius $R > 1$ such that there are no singularities in u in the circular annulus $\{(x, y) \in \mathbb{R}^2 | 1 < x^2 + y^2 < r^2\}$. From Figure 2.5 it can be seen that there is excellent agreement between the BEM and MFS numerical solutions except for the coarse boundary mesh/degrees of freedom of 8 to 16 elements. However, increasing the number of collocation points M and the degrees of freedom N, leads to both $u(1, \theta)$ and its derivative $\partial u/\partial n(1, \theta)$ showing good agreement with the BEM solution. Furthermore, the MFS gives the closest agreement to the BEM results with $M = N = 128$ and $R = 1.15$. However, for the large choice of $M = N = 256$, the MFS shows some slight instability in the normal derivative, see Figure 2.6. This instability is due to the ill-conditioning of the matrix F. This is a commonly known problem with the MFS, see [17, 43, 52].

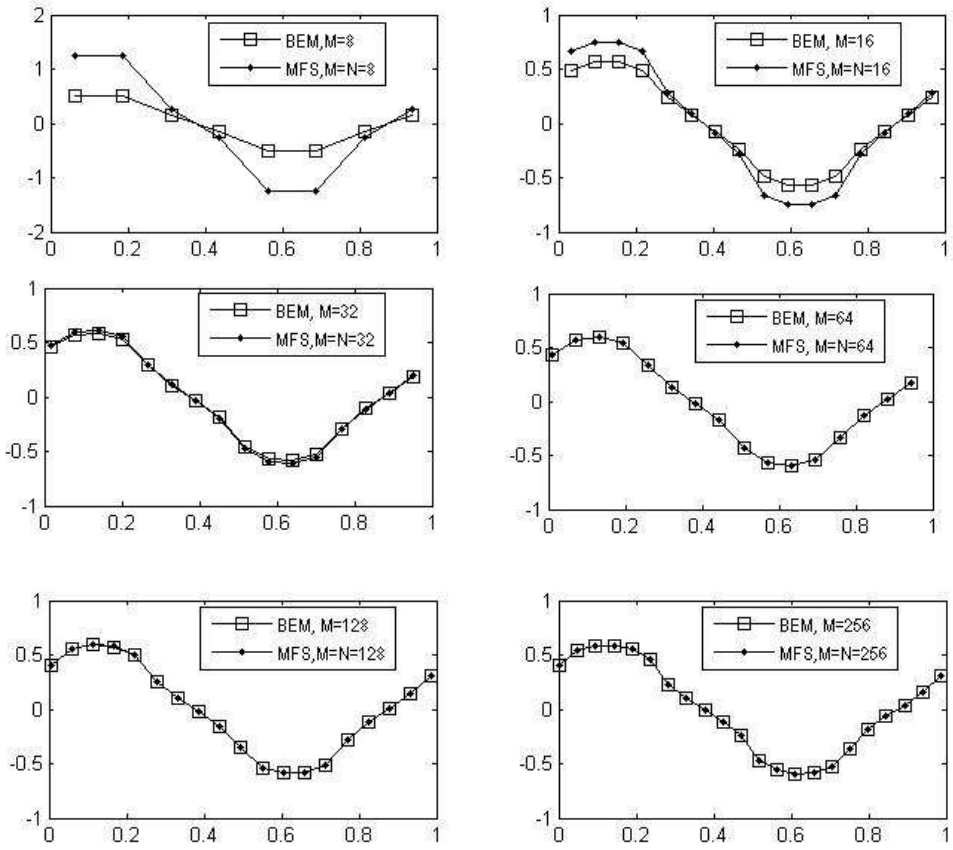

Figure 2.5: Comparison between $u^{MFS}(1,\theta)$ and $u^{BEM}(1,\theta)$, as functions of $\theta/(2\pi)$, for Example 1.

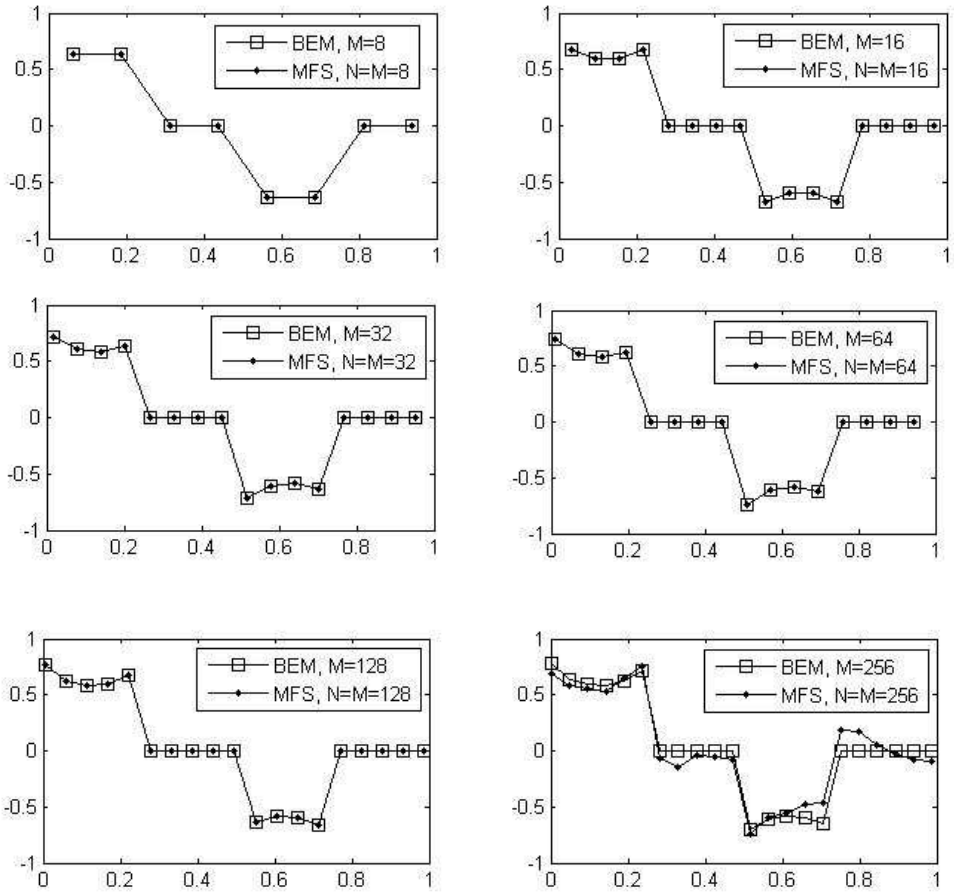

Figure 2.6: Comparison between $\frac{\partial u}{\partial n}^{MFS}(1,\theta)$ and $\frac{\partial u}{\partial n}^{BEM}(1,\theta)$, as functions of $\theta/(2\pi)$, for Example 1.

Table 2.3 shows the condition numbers, defined as the ratio between the largest singular value to the smallest one, of the BEM and MFS matrices D and F, respectively. This table shows that the BEM matrix D is well-conditioned, but the MFS matrix F is ill-conditioned.

Table 2.3: Condition numbers of the matrices D and F of the BEM and MFS systems of equations (2.16) and (2.23), respectively, for various numbers of boundary elements M (in the BEM) and degrees of freedom $M = N$ (in the MFS with $R = 1.15$), for Example 1.

$M = N$	8	16	32	64	128	256
$cond(D)$	35.58	86.62	215.97	484.40	10^3	2×10^3
$cond(F)$	3×10^{16}	5×10^{16}	3×10^{17}	7×10^{16}	2×10^{17}	4×10^{18}

Example 2. We next solve Example 1 using the BEM and MFS when the number of electrodes is increased to $L = 4$ and 8, with the input data $z_p = 1$ for $p = \overline{1, L}$ and injected currents

$$I_p = \begin{cases} 1 & \text{if } p = 1, \\ -1 & \text{if } p = L, \\ 0 & \text{if } p \in \{2, ..., L-1\}. \end{cases} \tag{2.25}$$

Solution: Table 2.4 shows the numerical MFS and BEM interior solutions and the absolute errors between them. It can be seen that for both $L = 4$ and $L = 8$, the MFS and the BEM interior solutions agree up to three decimal places. In addition, the accuracy increases as we move further towards the centre of the unit disk.

Table 2.4: The BEM numerical solution (with $M = 128$) of Example 2 at the some interior points and (in brackets) the absolute errors between the BEM and MFS (with $M = N = 128$).

$L = 4$					
r \ θ	$2\pi/10$	$4\pi/10$	$6\pi/10$	$8\pi/10$	$10\pi/10$
$1/10$	0.0394 (1×10^{-5})	0.0426 (1×10^{-5})	0.0301 (8×10^{-6})	0.0088 (2×10^{-6})	-0.0146 (3×10^{-6})
$2/10$	0.0841 (3×10^{-5})	0.0836 (2×10^{-5})	0.0551 (1×10^{-5})	0.0156 (3×10^{-6})	-0.0259 (5×10^{-6})
$3/10$	0.1340 (5×10^{-5})	0.1223 (3×10^{-5})	0.0752 (1×10^{-5})	0.0207 (3×10^{-6})	-0.0345 (5×10^{-6})
...	...	...	...	...	...
$9/10$	0.5723 (4×10^{-4})	0.2593 (3×10^{-5})	0.1216 (3×10^{-5})	0.0330 (3×10^{-6})	-0.0560 (8×10^{-6})
$L = 8$					
r \ θ	$2\pi/10$	$4\pi/10$	$6\pi/10$	$8\pi/10$	$10\pi/10$
$1/10$	0.0199 (7×10^{-6})	0.0242 (7×10^{-6})	0.0191 (4×10^{-6})	0.0085 (2×10^{-6})	-0.0039 (9×10^{-7})
$2/10$	0.0449 (1×10^{-5})	0.0484 (1×10^{-5})	0.0347 (7×10^{-6})	0.0147 (2×10^{-6})	-0.0067 (1×10^{-6})
$3/10$	0.0752 (2×10^{-5})	0.0714 (1×10^{-5})	0.0469 (7×10^{-6})	0.0191 (2×10^{-6})	-0.0087 (1×10^{-6})
...	...	...	...	...	...
$9/10$	0.3099 (1×10^{-4})	0.1451 (1×10^{-5})	0.0748 (4×10^{-6})	0.0276 (4×10^{-7})	-0.0127 (2×10^{-6})

Figures 2.7 and 2.8 represent the comparison on the boundary for $L = 4$ and 8, respectively. From these figures it can be seen that both methods still follow the same pattern as for the case $L = 2$.

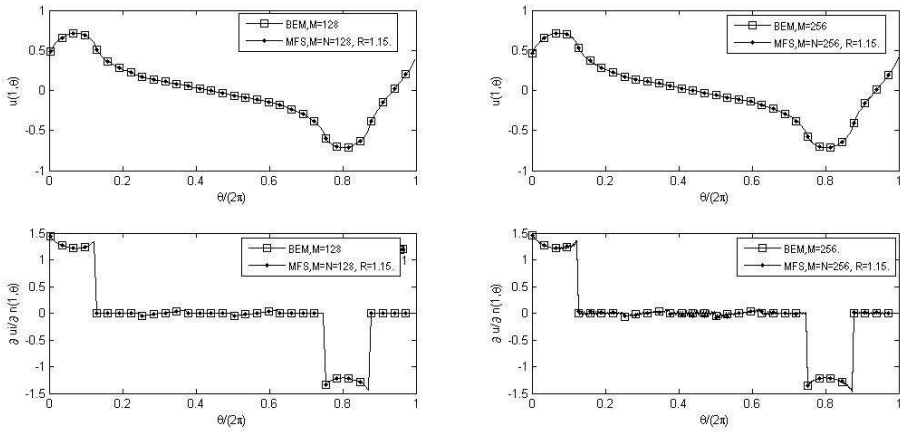

Figure 2.7: Comparison between the MFS and BEM solutions and their normal derivatives on the boundary when the number of electrodes is $L = 4$.

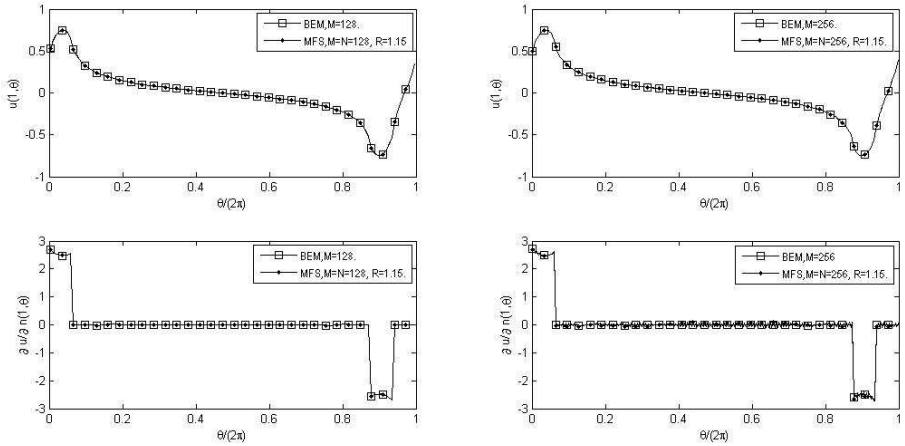

Figure 2.8: Comparison between the MFS and BEM solutions and their normal derivatives on the boundary when the number of electrodes is $L = 8$.

2.6 Extension to multiply-connected domains

So far, the solution domain Ω, which has been considered, has been a simply-connected domain. In this section, we will investigate the direct ERT problem in a domain which has a void (rigid inclusion or cavity) inside.

2.6.1 Applying the BEM to the direct ERT problem in an annular domain with a rigid inclusion

Here, the solution domain is the annulus
$\Omega\backslash\Omega_{Inner} = \{(x,y) \in \mathbb{R}^2 | (0.5)^2 < x^2 + y^2 < 1\}$, where on the boundary of the hole inside (rigid inclusion), the boundary condition is $u = 0$.

First, the external boundary $r = 1$ is uniformly discretised into M boundary elements and the numbering of these elements is anticlockwise. Similarly, the internal boundary $r = 0.5$ is uniformly discretized into another M boundary elements, but these are numbered clockwise, [55]. The endpoints of the external boundary elements are

$$\underline{p_i} = (x_i, y_i) = \left(\cos\left(\frac{2\pi i}{M}\right), \sin\left(\frac{2\pi i}{M}\right)\right), \quad i = \overline{1, M},$$

with the convention that $\underline{p}_0 = \underline{p}_M$, whereas the endpoints of the internal boundary elements are

$$\underline{p_i} = (x_i, y_i) = \left(0.5\cos\left(2\pi - \frac{2\pi(i-M)}{M}\right), 0.5\sin\left(2\pi - \frac{2\pi(i-M)}{M}\right)\right),$$
$$i = \overline{M+1, 2M}.$$

Since $u = 0$ on the boundary of the rigid inclusion, the EIT problem is reduced to solving a new linear system of BEM equations

$$B\underline{u}_{Outer} + A\underline{u'} = \underline{0}, \tag{2.26}$$

where $\underline{u} := \left(u\left(\underline{\tilde{p}_i}\right)\right)_{i=\overline{1,M}}$, and $\underline{u'} := \begin{pmatrix} \underline{u'}_{Outer} \\ \underline{u'}_{Inner} \end{pmatrix} := \begin{pmatrix} \frac{\partial u}{\partial n}(\underline{\tilde{p}}_i)_{i=\overline{1,M}} \\ \frac{\partial u}{\partial n}(\underline{\tilde{p}}_i)_{i=\overline{M+1,2M}} \end{pmatrix}$. We also denote the boundary element node $\tilde{p}_i = (p_i + p_{i-1})/2$ for $i = \overline{1, M} \cup \overline{M+2, 2M}$, and $\tilde{p}_{M+1} = (p_{M+1} + p_{2M})/2$.

First, we collocate the boundary condition (2.2) for the electrodes ε_p, $p = \overline{1, L}$, at

the nodes $\tilde{p}_{i-2M}$, resulting in

$$u_{i-2M} + z_p {u'}_{i-2M} - \frac{2\pi}{M\ell_p} \sum_{k=(KM/L)+1}^{(2K+1)M/(2L)} u_k = \frac{z_p I_p}{\ell_p},$$
$$i = \overline{(2M+1+KM/L), (2M+(2K+1)M/(2L)}, \qquad (2.27)$$

where $K = \overline{0, (L-1)}$. This yields $\frac{M}{2}$ equations.

Second, by applying the zero flux boundary condition (2.5) for the gaps g_p, $p = \overline{1, L}$, between electrodes at the nodes $\tilde{p}_{i-2M}$, we obtain

$$u'_{i-2M} = 0, \;\; i = \overline{(2M+1+(2K-1)M/(2L)), (2M+KM/L)}, \qquad (2.28)$$

where $K = \overline{1, L}$. This yields another $\frac{M}{2}$ equations.

Finally, the condition

$$\int_{\partial\Omega_{Outer}} u \; ds = 0$$

yields one more equation, namely,

$$\sum_{k=1}^{M} u_k = 0. \qquad (2.29)$$

Therefore, to find the solution of the CEM problem (2.1), (2.2), (2.5) and (2.6) in an annular domain containing an inner rigid inclusion using the BEM, the equations (2.27)-(2.29) are reformulated in the following matrix form as a $(3M+1) \times (3M)$ linear system of algebraic equations:

$$D\underline{X} = \underline{b}, \qquad (2.30)$$

where

$$\underline{X} = \begin{pmatrix} \underline{u}_{Outer} \\ \underline{u'}_{Outer} \\ \underline{u'}_{Inner} \end{pmatrix}. \tag{2.31}$$

Since the system of equations (2.30) is over-determined, we have used the least-squares method to solve it. This yields the solution (2.17) for the unspecified boundary data (2.31).

Once the boundary data has been obtained accurately, equation (2.11) can be applied for $\underline{p} \in \Omega$ to provide explicitly the interior solution for $u(\underline{p})$.

2.6.2 Applying the MFS to the direct ERT problem in an annular domain with a rigid inclusion

In this section, the MFS seeks a solution of Laplace's equation (2.1) as a linear combination of fundamental solutions of the form:

$$u(\underline{p}) = \sum_{j=1}^{2N} c_j G(\underline{\xi}_j, \underline{p}), \qquad \underline{p} \in \Omega \backslash \Omega_{Inner} \tag{2.32}$$

where $\underline{\xi}_j$ are the sources located outside the outer domain

$$\Omega = \left\{(x, y) \in \mathbb{R}^2 | x^2 + y^2 < 1\right\}$$

and inside the rigid inclusion

$$\Omega_{Inner} = \left\{(x, y) \in \mathbb{R}^2 | x^2 + y^2 < (0.5)^2\right\}.$$

The $(c_j)_{j=\overline{1,2N}}$ are unknown coefficients to be determined by imposing the boundary conditions (2.2), (2.5), (2.6) and

$$u = 0 \quad \text{on} \quad \partial\Omega_{Inner}. \tag{2.33}$$

We take the external source points $\underline{\xi}_j = (\xi_j^1, \xi_j^2) = (R\cos\left(\frac{2\pi j}{N}\right), R\sin\left(\frac{2\pi j}{N}\right))$ for $j = \overline{1, N}$, where $1 < R < \infty$, the internal source points $\underline{\xi}_j = (\xi_j^1, \xi_j^2) = \left(R_1\cos\left(\frac{2\pi(j-N)}{N}\right), R_1\sin\left(\frac{2\pi(j-N)}{N}\right)\right)$, for $j = \overline{N+1, 2N}$, where $0 < R_1 < 0.5$. We also take the external boundary collocation points $\underline{x}_i = (\cos\left(\frac{2\pi i}{M}\right), \sin\left(\frac{2\pi i}{M}\right))$ for $i = \overline{1, M}$, and the internal boundary collocation points $\underline{x}_i = \left(0.5\cos\left(\frac{2\pi(j-M)}{M}\right), 0.5\sin\left(\frac{2\pi(j-M)}{M}\right)\right)$ for $i = \overline{M+1, 2M}$.

For external points $\underline{p} = (x, y) \in \partial\Omega$ we have

$$\frac{\partial G}{\partial n}(\underline{\xi}_j, \underline{p}) = \frac{1 - (\xi_j^1 x + \xi_j^2 y)}{-2\pi|\underline{\xi}_j - \underline{p}|^2}, \qquad j = \overline{1, 2N}, \tag{2.34}$$

whilst for internal points $\underline{p} = (x, y) \in \partial\Omega_{Inner}$ we have

$$\frac{\partial G}{\partial n}(\underline{\xi}_j, \underline{p}) = \frac{(0.5)^2 - (\xi_j^1 x + \xi_j^2 y)}{-2(0.5)\pi|\underline{\xi}_j - \underline{p}|^2}, \qquad j = \overline{1, 2N}. \tag{2.35}$$

In order to obtain the coefficient vector $\underline{c} = (c_j)_{j=\overline{1,2N}}$, we substitute equations (2.9), (2.34), and (2.35) into the boundary conditions (2.2), (2.5), (2.6) and (2.33).

First, we apply the boundary condition (2.2) for the electrodes ε_p, $p = \overline{1, L}$, at the collocation points $\underline{x}_i$ on ε_p resulting in

$$\sum_{j=1}^{2N}\left[G(\underline{\xi}_j, \underline{x}_i) - \frac{2\pi}{M\ell_p}\sum_{k=(KM/L)+1}^{(2K+1)M/(2L)} G(\underline{\xi}_j, \underline{x}_k) + z_p\frac{\partial G}{\partial r}(\underline{\xi}_j, \underline{x}_i)\right]c_j = \frac{z_p I_p}{\ell_p},$$
$$i = \overline{(KM/L)+1, (2K+1)M/(2L)}, \tag{2.36}$$

where $K = \overline{0,(L-1)}$. This yields $\frac{M}{2}$ equations.

Second, by applying the zero flux boundary condition (2.5) on the gaps $g_p, p = \overline{1,L}$, between electrodes, we obtain

$$\sum_{j=1}^{2N} c_j \frac{\partial G}{\partial r}(\underline{\xi}_j, \underline{x}_i) = 0, \quad i = \overline{(1+(2K-1)M/(2L)),(KM/L)} \tag{2.37}$$

where $K = \overline{1,L}$. This yields another $\frac{M}{2}$ equations.

Third, we apply (2.33) which gives M more equations

$$\sum_{j=1}^{2N} c_j G(\underline{\xi}_j, \underline{x}_i) = 0, \quad i = \overline{M+1,2M}. \tag{2.38}$$

Finally, by imposing the condition (2.6) and using (2.38), yields one more equation

$$\sum_{i=1}^{2M} \sum_{j=1}^{2N} c_j G(\underline{\xi}_j, \underline{x}_i) = 0. \tag{2.39}$$

Again, to find the solution of the CEM problem (2.1), (2.2), (2.5), (2.6) and (2.33) using the MFS, the equations (2.36)-(2.39) are reformulated in the following matrix form as a $(2M+1) \times 2N$ linear system of algebraic equations:

$$F\underline{c} = \underline{b}. \tag{2.40}$$

The least-squares method is used to solve the system of equations (2.40). This yields the solution (2.24).

Once the coefficient vector $\underline{c}$ has been obtained accurately, equations (2.32), (2.34) and (2.35) provide explicitly the solution for the potential u_{Outer} on the external boundary $\partial\Omega$ and inside the annular domain Ω, the current flux $(\partial u/\partial n)_{Outer}$ on the external boundary $\partial\Omega$ and the current flux $(\partial u/\partial n)_{Inner}$ on the internal boundary $\partial\Omega_{Inner}$, respectively.

Example 3. Solve the problem (2.1), (2.2), (2.5), (2.6) and (2.33) using the BEM and MFS with the same input data as in Example 1.

BEM solution: The matrix D in equation (2.30) is given by

$$D_{i,l} = \begin{cases} B_{i,l} & \text{if } l = \overline{1, M}, \\ A_{i,l} & \text{if } l = \overline{(M+1), 3M} \end{cases} \qquad i = \overline{1, 2M}.$$

Using equations (2.27)-(2.29) we obtain:

$$D_{i,l} = \begin{cases} -\frac{h}{\ell_1} & \text{if } (i-2M) \neq l, l = \overline{1, M/4}, \\ (1 - \frac{h}{\ell_1}) & \text{if } (i-2M) = l, l = \overline{1, M/4}, \\ 0 & \text{if } l = \overline{(M/4+1), M} \cup \overline{(2M+1), 3M}, \\ z_1\delta_{i,l} & \text{if } l = \overline{(M+1), 2M}, \end{cases}$$

$$i = \overline{(2M+1), (2M+M/4)},$$

$$D_{i,l} = \begin{cases} -\frac{h}{\ell_2} & \text{if } (i-2M) \neq l, l = \overline{(M/2+1), 3M/4}, \\ (1 - \frac{h}{\ell_2}) & \text{if } (i-2M) = l, l = \overline{(M/2+1), 3M/4}, \\ 0 & \text{if } l = \overline{1, M/2} \cup \overline{(3M/4+1), M} \cup \overline{(2M+1), 3M}, \\ z_2\delta_{i,l} & \text{if } l = \overline{(M+1), 2M}, \end{cases}$$

$$i = \overline{(2M+M/2+1), (2M+3M/4)},$$

$$D_{i,l} = \delta_{i,l}, \text{ if } l = \overline{(M+1), 2M},$$

$$i = \overline{(2M+M/4+1), (M+M/2)} \cup \overline{(2M+3M/4+1), 3M}.$$

The last row in the matrix D is given by

$$D_{(3M+1),l} = \begin{cases} 1 & \text{if } l = \overline{1, M}, \\ 0 & \text{if } l = \overline{M+1, 3M}. \end{cases}$$

Furthermore, the vector $\underline{b}$ is given by

$$\underline{b} = \begin{pmatrix} \underline{0} & \frac{z_1 I_1}{\ell_1} & \underline{0} & \frac{z_2 I_2}{\ell_2} & \underline{0} & 0 \end{pmatrix}^T. \tag{2.41}$$

MFS solution: Turning now to the MFS solution, the first $M/4$ rows of the matrix F in equation (2.40) corresponding to the first electrode ε_1 are

$$F_{i,j} = G_{i,j} - \frac{2\pi}{M\ell_1}\left(G_{i,j} + G_{i+1,j} + ... + G_{M/4,j}\right) + z_1 G'_{i,j}, \;\; i = \overline{1, M/4}, \;\; j = \overline{1, 2N}.$$

Another $\frac{M}{4}$ rows in the matrix F are generated by applying the boundary condition (2.2) on the second electrode ε_2, namely

$$F_{i,j} = G_{i,j} - \frac{2\pi}{M\ell_2}\left(G_{(M/2+1),j} + G_{(M/2+2),j} + ... + G_{3M/4,j}\right) + z_2 G'_{i,j},$$

$$i = \overline{(M/2+1), 3M/4}, \;\; j = \overline{1, 2N}.$$

In addition, applying the no flux boundary condition (2.5) results in another $\frac{M}{2}$ rows given by

$$F_{i,j} = G'_{i,j}, \;\; i = \overline{(M/4+1), M/2} \cup \overline{3M/4+1}, \;\; j = \overline{1, 2N}.$$

Moreover, another M rows are generated by applying the inner boundary condition (2.33), namely,

$$F_{i,j} = G_{i,j}, \;\; i = \overline{(M+1), 2M}, \;\; j = \overline{1, 2N}.$$

To end with, the last row in the matrix F, obtained using equation (2.39), is:

$$F_{2(M+1),j} = \sum_{i=1}^{2M} G_{i,j}, \quad j = \overline{1, 2N}.$$

The vector $\underline{b}$ of the linear system of equations (2.40) is given by

$$\underline{b} = \left(\frac{z_1 I_1}{\ell_1} \quad \underline{0} \quad \frac{z_2 I_2}{\ell_2} \quad \underline{0} \quad 0 \right)^T . \tag{2.42}$$

In the MFS we take $R = 1.15$ and $R_1 = 0.45$.

Figures 2.9, 2.10 and 2.11 present a comparison between the BEM and MFS solutions for the boundary data $u_{Outer}(1,\theta)$, $(\partial u/\partial n)_{Outer}(1,\theta)$ and $(\partial u/\partial n)_{Inner}(0.5,\theta)$, respectively. From these figures it can be seen that the BEM outer solution and its derivative, as well as the BEM inner derivative are convergent, as the number of boundary elements M increases. This is also true when the MFS is used except for $M = N = 256$. In this later case, the outer solution still has reasonable accuracy, but the normal derivative (Figure 2.11) on the inner boundary becomes highly unstable, see also Table 2.5 for the condition numbers.

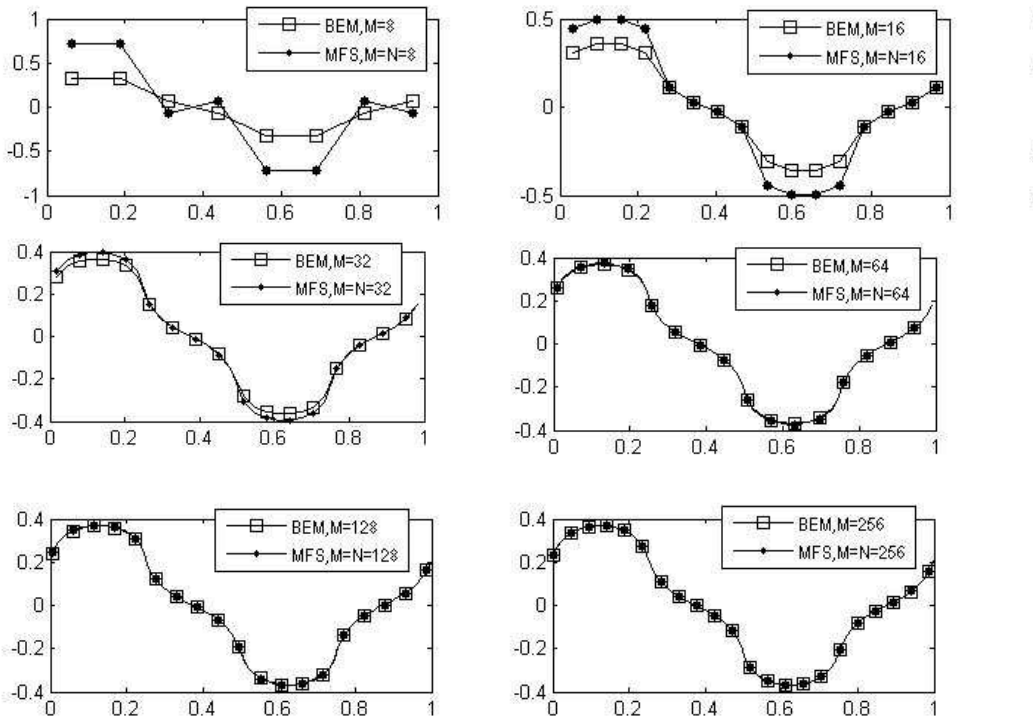

Figure 2.9: Comparison between $u_{Outer}^{MFS}(1,\theta)$ and $u_{Outer}^{BEM}(1,\theta)$, as functions of $\theta/(2\pi)$, for Example 3.

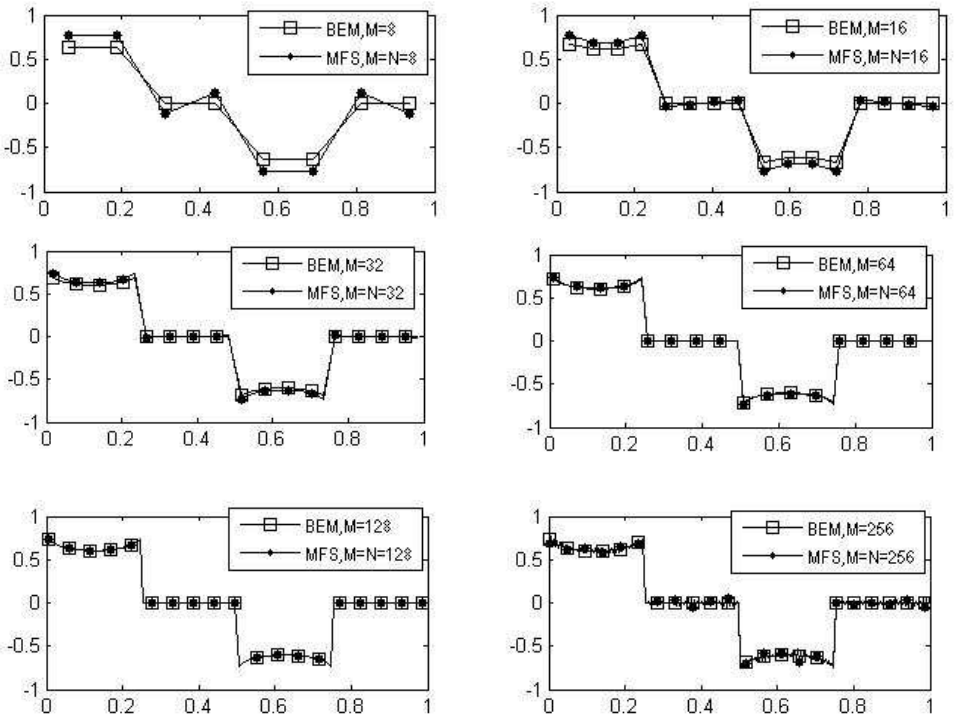

Figure 2.10: Comparison between $(\frac{\partial u}{\partial n})_{Outer}^{MFS}(1,\theta)$ and $(\frac{\partial u}{\partial n})_{Outer}^{BEM}(1,\theta)$, as functions of $\theta/(2\pi)$, for Example 3.

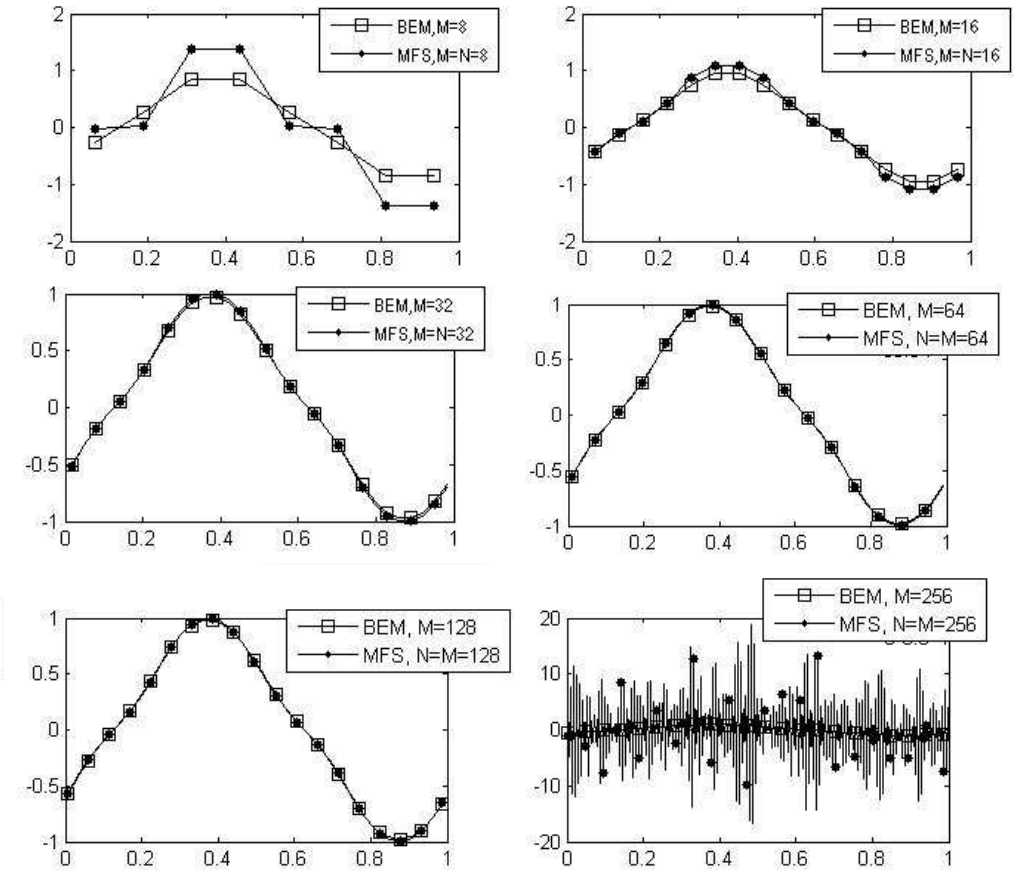

Figure 2.11: Comparison between $(\frac{\partial u}{\partial n})_{Inner}^{MFS}(0.5,\theta)$ and $(\frac{\partial u}{\partial n})_{Inner}^{BEM}(0.5,\theta)$, as functions of $\theta/(2\pi)$, for Example 3.

Table 2.5: Condition numbers of the matrices D and F of the BEM and MFS systems of equations (2.30) and (2.40), respectively, for various numbers of boundary elements M (in the BEM) and degrees of freedom $M = N$ (in the MFS with $R = 1.15$ and $R_1 = 0.45$), for Example 3.

	8	16	32	64	128	256
$cond(D)$	2×10^3	10^4	10^5	7×10^5	6×10^6	5×10^7
$cond(F)$	10^{17}	6×10^{18}	2×10^{18}	5×10^{18}	4×10^{17}	2×10^{19}

2.6.3 Applying the BEM to the direct ERT problem in an annular domain with a cavity

Here, the solution domain is the same annulus as in Subsection 2.6.1, but now it contains a cavity inside on whose boundary $\partial u/\partial n = 0$.

The BEM implementation is the same as that for the rigid inclusion of Subsection 2.6.1, however now the BEM reduces to solving the system of equations

$$B\underline{u} + A\underline{u'}_{Outer} = \underline{0}, \tag{2.43}$$

where $\underline{u} := \begin{pmatrix} \underline{u}_{Outer} \\ \underline{u}_{Inner} \end{pmatrix} := \begin{pmatrix} u(\underline{\tilde{p}}_i)_{i=\overline{1,M}} \\ u(\underline{\tilde{p}}_i)_{i=\overline{M+1,2M}} \end{pmatrix}$, and $\underline{u'}_{Outer} := \left(\frac{\partial u}{\partial n}\left(\underline{\tilde{p}}_i\right)\right)_{i=\overline{1,M}}$.
Equations (27)-(29) remain the same. Therefore, to find the solution of the CEM (2.1), (2.2), (2.5) and (2.6) in an annular domain with a cavity using the BEM, the equations (2.27)-(2.29) and (2.43) are reformulated in the following matrix form as a $(3M+1)\times(3M)$ linear system of algebraic equations:

$$D\underline{X} = \underline{b}, \tag{2.44}$$

where

$$\underline{X} = \begin{pmatrix} \underline{u}_{Outer} \\ \underline{u'}_{Outer} \\ \underline{u}_{Inner} \end{pmatrix}. \tag{2.45}$$

Since the system of equations (2.44) is over-determined, we have used the least-squares method to solve it. This yields the solution (2.17) for the unspecified boundary data (2.45). Afterwards, equation (2.11) can be applied for $\underline{p} \in \Omega \backslash \Omega_{Inner}$ to provide explicitly the interior solution for $u(\underline{p})$.

2.6.4 Applying the MFS to the direct ERT problem in an annular domain with a cavity

Using the MFS to solve the forward ERT problem in a region which contains a cavity inside is similar to solving that problem with the rigid inclusion of Subsection 2.6.2. The only difference is that the internal Dirichlet homogenous boundary condition (2.33) is replaced by the zero flux boundary condition

$$\frac{\partial u}{\partial n} = 0 \ \text{ on } \ \partial\Omega_{Inner}. \tag{2.46}$$

Hence,

$$\sum_{j=1}^{2N} c_j \frac{\partial G}{\partial n}(\underline{\xi}_j, \underline{x}_i) = 0, \ \ i = \overline{M+1, 2M}. \tag{2.47}$$

Due to this change, the rows

$$F_{i,j} = G'_{i,j}, \ \ i = \overline{(M+1), 2M}, \ \ j = \overline{1, 2N},$$

will be updated in the new matrix F.

Example 4. Solve the problem (2.1), (2.2), (2.5), (2.6) and (2.46) using the BEM and MFS with the same input data as in Example 1.

Solution: The matrix D in equation (2.44) has the same structure as for Example 3, but the last row is given by

$$D_{(3M+1),l} = \begin{cases} 1 & \text{if } l = \overline{1, M} \cup \overline{2M+1, 3M}, \\ 0 & \text{if } l = \overline{M+1, 2M}. \end{cases}$$

Furthermore, the vector $\underline{b}$ is the same as that given by (2.41).

Figures 2.12, 2.13 and 2.14 present a comparison between the BEM and MFS so-

lution for the boundary data $u_{Outer}(1,\theta)$ and $(\partial u/\partial n)_{Outer}(1,\theta)$ and $u_{Inner}(0.5,\theta)$, respectively. First, from Figures 2.12 and 2.13 the same conclusions, as those obtained from Figures 2.9 and 2.10 for the rigid inclusion problem of Example 3, can be drawn for the cavity problem of Example 4. Second, for large $M = N = 256$, the MFS instability in the normal derivative on the inner boundary of the rigid inclusion, highlighted in Figure 2.11, is not present in Figure 2.14. The reason for this is that retrieving higher order derivatives is less accurate and less stable than retrieving lower order ones, [47].

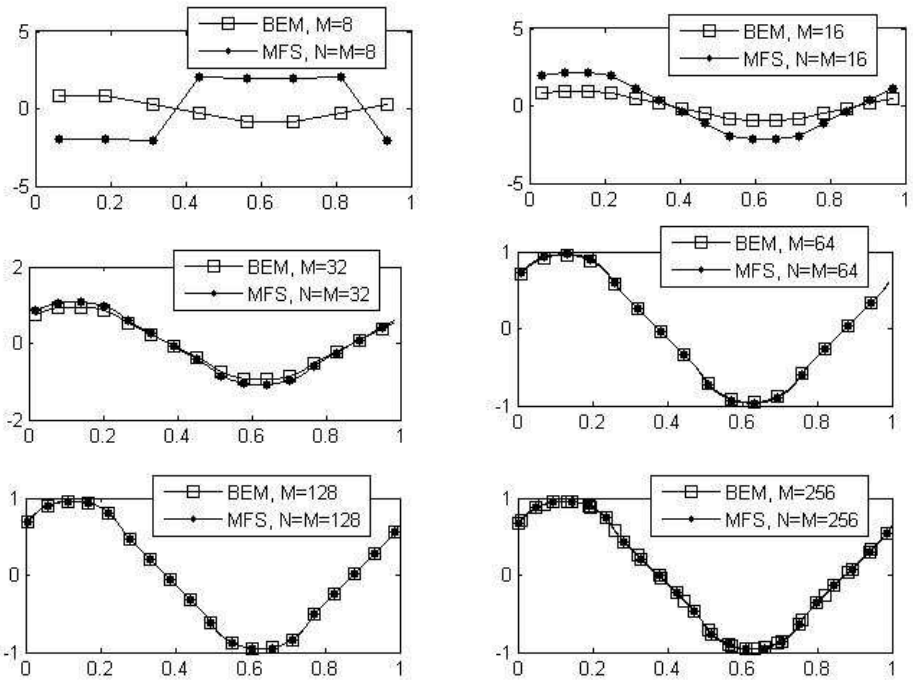

Figure 2.12: Comparison between $u_{Outer}^{MFS}(1,\theta)$ and $u_{Outer}^{BEM}(1,\theta)$, as functions of $\theta/(2\pi)$, for Example 4.

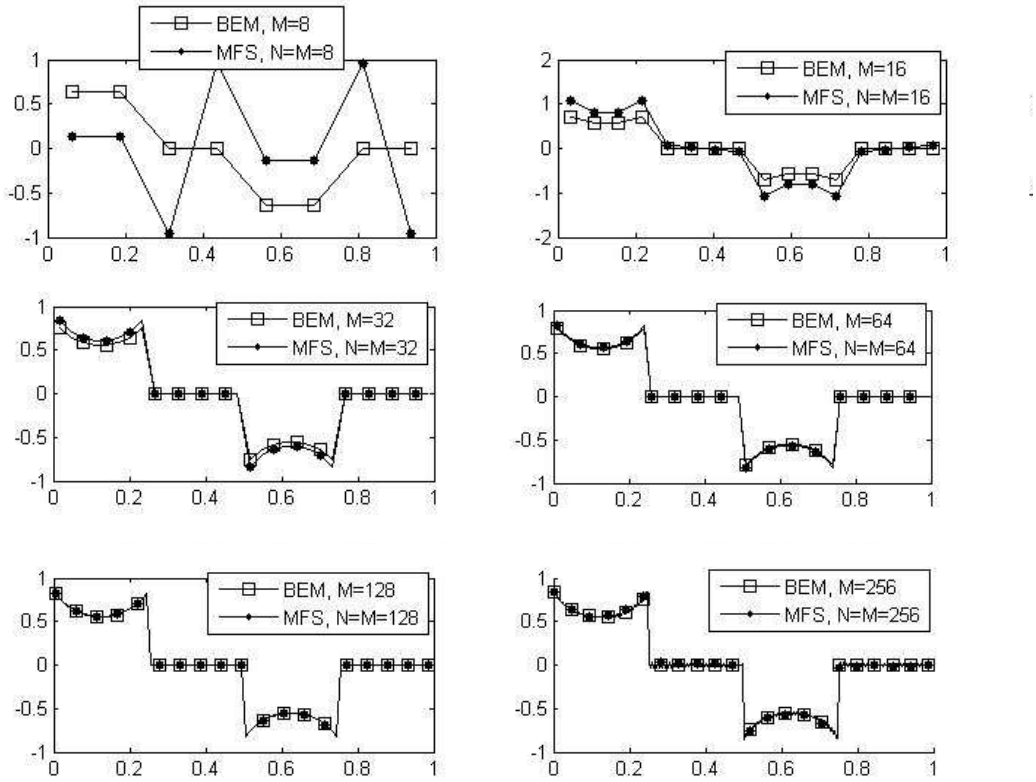

Figure 2.13: Comparison between $(\frac{\partial u}{\partial n})_{Outer}^{MFS}(1,\theta)$ and $(\frac{\partial u}{\partial n})_{Outer}^{BEM}(1,\theta)$, as functions of $\theta/(2\pi)$, for Example 4.

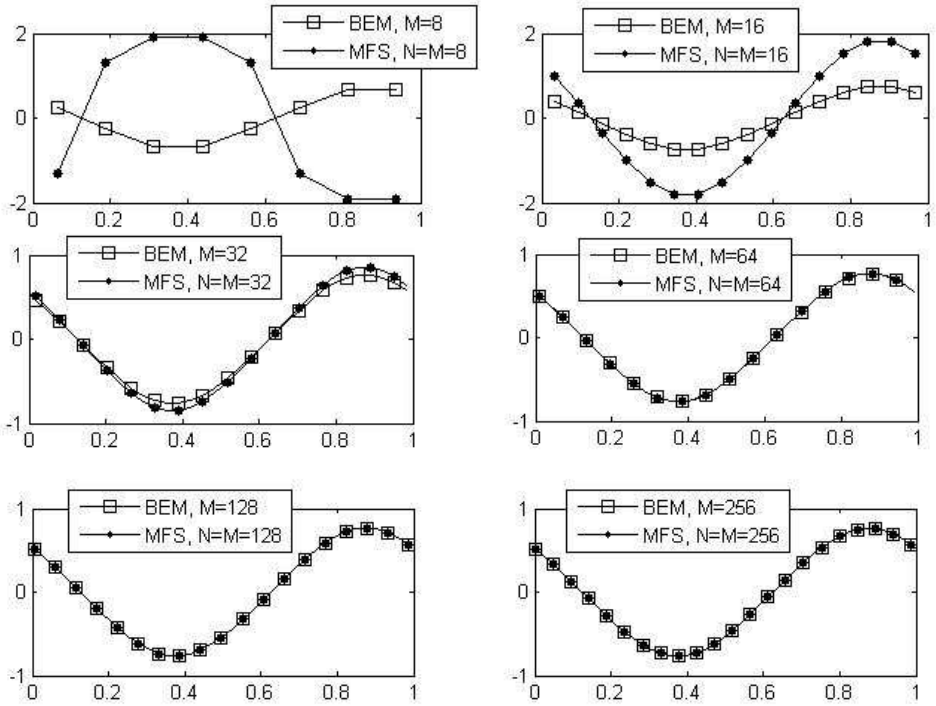

Figure 2.14: Comparison between $u_{Inner}^{MFS}(0.5,\theta)$ and $u_{Inner}^{BEM}(0.5,\theta)$, as functions of $\theta/(2\pi)$, for Example 4.

Table 2.6 shows the condition numbers of the BEM and MFS matrices D and F, respectively. This table shows that the BEM matrix D is well-conditioned, but the MFS matrix F is ill-conditioned.

Table 2.6: Condition numbers of the matrices D and F of the BEM and MFS systems of equations, for various numbers of boundary elements M (in the BEM) and degrees of freedom $M = N$ (in the MFS with $R = 1.15$ and $R_1 = 0.45$), for Example 4.

	8	16	32	64	128	256
$cond(D)$	311.91	643.53	10^3	2×10^3	5×10^3	$\times 10^4$
$cond(F)$	2×10^{17}	5×10^{16}	10^{18}	9×10^{17}	5×10^{17}	10^{18}

2.7 Extension to composite materials

In this section, the solution domain is represented by a bi-material $\Omega = \Omega_1 \cup \overline{\Omega}_2$, where $\Omega_1 = \{(x, y) \in \mathbb{R}^2 | (0.5)^2 < x^2 + y^2 < 1\}$ and
$\Omega_2 = \{(x, y) \in \mathbb{R}^2 | x^2 + y^2 < (0.5)^2\}$. So, the mathematical formulation of this problem is governed by two Laplace's equations, are in each of the two-dimensional bounded domains Ω_1 and Ω_2. The first equation is

$$\bigtriangledown^2 u_1 = 0, \qquad \text{in } \Omega_1 \tag{2.48}$$

subject to the same boundary conditions (2.2), (2.5) and (2.6) which make the problem the so-called 'complete-electrode model' (CEM).
The second Laplace's equation is

$$\bigtriangledown^2 u_2 = 0, \qquad \text{in } \Omega_2 \tag{2.49}$$

subject to the following transmission conditions on the interface $\overline{\Omega}_1 \cap \overline{\Omega}_2 = \partial\Omega_2$:

$$u_1 = u_2 \tag{2.50}$$

and

$$\frac{\partial u_1}{\partial n_1} = -\gamma \frac{\partial u_2}{\partial n_2} \tag{2.51}$$

where $\underline{n}_1$ is the outward unit normal to the boundary $\partial\Omega_1$ of the material Ω_1 and $\underline{n}_2 = -\underline{n}_1$ is the outward unit normal to the boundary $\partial\Omega_2$ of the material Ω_2, and $0 < \gamma \neq 1 < \infty$ is the ratio between the conductivities of the two materials Ω_2 and Ω_1.
The previous cases (simply-connected and multiply-connected) of Sections 2.5 and 2.6 could be considered as special cases of this composite material case, since:

(i) if $\gamma = 1$, then the two composite material case becomes the simply-connected

domain of Section 2.5.

(ii) if $\gamma = \infty$, then the two composite material case becomes the annular domain with a rigid inclusion of Section 2.6.1.

(iii) if $\gamma = 0$, then the two composite material case becomes the annular domain with a cavity of Section 2.6.2.

In the formulation above, Ω_2 is defined as a general inclusion and the geometry of the whole inclusion ERT problem is shown in Figure 2.15.

Figure 2.15: The two-dimensional CEM in a composite domain, for $L = 2$ and 4 electrodes.

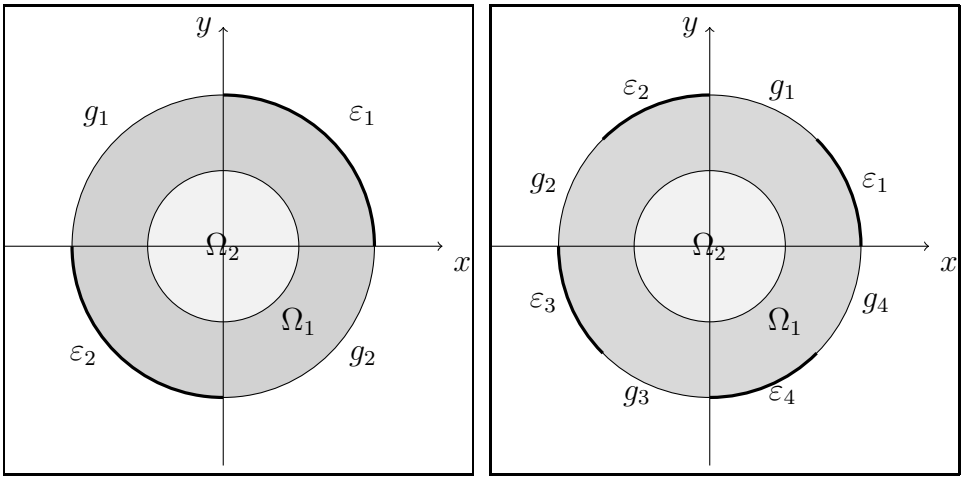

2.7.1 Applying the BEM to the direct ERT problem in a composite bi-material

In this section, we will use the BEM to solve the inclusion ERT problem given by equations (2.2), (2.5), (2.6), (2.48)-(2.51). For the first domain Ω_1, the discretisation of the boundary $\partial\Omega_1$, is the same as in Section 2.6.1. Hence, the BEM reduces the Laplace's equation (2.48) for u_1 to a new linear system of equations similar to (2.26), namely,

$$B\underline{u_1} + A\underline{u_1'} = \underline{0}, \tag{2.52}$$

where $\underline{u_1} := \begin{pmatrix} \underline{u_1}_{Outer} \\ \underline{u_1}_{Inner} \end{pmatrix} := \begin{pmatrix} u_1(\underline{\tilde{p}}_i)_{i=\overline{1,M}} \\ u_1(\underline{\tilde{p}}_i)_{i=\overline{M+1,2M}} \end{pmatrix}$ and $\underline{u_1'} := \begin{pmatrix} \underline{u_1'}_{Outer} \\ \underline{u_1'}_{Inner} \end{pmatrix} := \begin{pmatrix} \frac{\partial u_1}{\partial n_1}(\underline{\tilde{p}}_i)_{i=\overline{1,M}} \\ \frac{\partial u_1}{\partial n_1}(\underline{\tilde{p}}_i)_{i=\overline{M+1,2M}} \end{pmatrix}$. Equation (2.52) provides the first $2M$ rows of the matrix D.

Now, for the second domain Ω_2 we discretise the internal boundary $\partial\Omega_2$ into M boundary elements, directed clockwise. Hence, the BEM reduces the second Laplace's equation (2.49) for u_2 to a new linear system of equations, similar to (2.8), namely,

$$\tilde{B}\underline{u_2} + \tilde{A}\underline{u_2'} = \underline{0}, \tag{2.53}$$

where $\underline{u_2} = (u_2(\tilde{p}_{2M+1-i}))_{i=\overline{M+1,2M}}$ and $\underline{u_2'} = \left(\frac{\partial u_2}{\partial n_2}(\tilde{p}_{2M+1-i})\right)_{i=\overline{M+1,2M}}$. Collocating the interface transmission conditions (2.50) and (2.51) at the corresponding boundary element nodes and using (2.53) we obtain

$$\tilde{B}\left(\underline{u_1}\right)_{Inner} - \frac{1}{\gamma}\tilde{A}\left(\underline{u_1'}\right)_{Inner} = \underline{0}. \tag{2.54}$$

Equations (2.52) and (2.54) from a system of $3M$ equations with $4M$ unknowns. In order to make this system of equations uniquely solvable the conditions (2.2), (2.5) and (2.6) should be imposed on the outer boundary. To begin with, we collocate the boundary condition (2.2) for the electrodes ε_p, $p = \overline{1, L}$, at the nodes $\tilde{p}_{(i-3M)}$, resulting in

$$u_{1(i-3M)} + z_p {u'}_{1(i-3M)} - \frac{2\pi}{M\ell_p}\sum_{k=(KM/L)+1}^{(2K+1)M/(2L)} u_{1k} = \frac{z_p I_p}{\ell_p},$$
$$i = \overline{(3M + 1 + KM/L), (3M + (2K + 1)M/(2L))}, \tag{2.55}$$

where $K = \overline{0, (L-1)}$. This yields $\frac{M}{2}$ equations.

Second, by applying the zero flux boundary condition (2.5) on the gaps g_p, $p = \overline{1, L}$,

between electrodes, we obtain

$$u'_{1(i-3M)} = 0, \quad i = \overline{(3M + 1 + (2K - 1)M/(2L)), (3M + KM/L)}, \tag{2.56}$$

where $K = \overline{1, L}$. This yields another $\frac{M}{2}$ equations.

Finally, the condition (2.6) yield one more equation, namely,

$$\sum_{k=1}^{M} u_{1k} = 0. \tag{2.57}$$

Therefore, to find the solution of the CEM given by equations (2.2), (2.5) and (2.48)-(2.51) in a composite material using the BEM, the equations (2.52), (2.54) and (2.55)-(2.57) are reformulated in the following matrix form as a $(4M + 1) \times (4M)$ linear system of algebraic equations:

$$D\underline{X} = \underline{b}, \tag{2.58}$$

where

$$\underline{X} = \begin{pmatrix} \underline{u}_{Outer} \\ \underline{u}_{Inner} \\ \underline{u'}_{Outer} \\ \underline{u'}_{Inner} \end{pmatrix}. \tag{2.59}$$

Since the system of equations (2.58) is over-determined, we have used the least-squares method to solve it. This yields the solution (2.17) for the unspecified boundary data (2.59).

2.7.2 Applying the MFS to the direct ERT problem in a composite bi-material

In this section, the MFS for the Laplace's equations (2.48) and (2.49) in the composite material $\Omega = \Omega_1 \cup \overline{\Omega}_2$ is applied by seeking a solution of Laplace's equation (2.48) as a linear combination of fundamental solutions of the form:

$$u_1(\underline{p}) = \sum_{j=1}^{2N} c_j G(\underline{\xi}_j, \underline{p}), \qquad \underline{p} \in \overline{\Omega}_1, \tag{2.60}$$

where the sources $\underline{\xi}_j$ and the collocation points $\underline{x}_i$ are exactly the same as in Section 2.6.2, and by seeking a solution of Laplace's equation (2.49) as a linear combination of fundamental solutions of the form:

$$u_2(\underline{p}) = \sum_{j=2N+1}^{3N} c_j G(\underline{\xi}_j, \underline{p}), \qquad \underline{p} \in \overline{\Omega}_2. \tag{2.61}$$

Similar domain decompositions technique for composite materials have been developed in [11–13] for the steady-state heat conduction governed by Laplace's equation, for the steady-state elasticity governed by the Lame´ system, and for the steady-state heat transfer governed by the modified Helmholtz equation, respectively.

In (2.61), the sources $\underline{\xi}_j$ are located outside Ω_{Inner}, so

$$\underline{\xi}_j = (\xi_j^1, \xi_j^2) = \left(R_2 \cos\left(\frac{2\pi(j-2N)}{N}\right), R_2 \sin\left(\frac{2\pi(j-2N)}{N}\right)\right), \ j = \overline{2N+1, 3N},$$

where $0.5 < R_2 < \infty$, and the new internal boundary collocation points are

$$\underline{x}_i = \left(0.5 \cos\left(\frac{2\pi(i-2M)}{M}\right), 0.5 \sin\left(\frac{2\pi(i-2M)}{M}\right)\right), \ i = \overline{2M+1, 3M}.$$

In order to obtain the coefficient vector $\underline{c} = (c_j)_{j=\overline{1,3N}}$, we substitute equations (2.9), (2.34), and (2.35) into the boundary conditions. To begin with, applying the boundary condition (2.2) results in equation (2.36), which in turn yields $\frac{M}{2}$ equations. In addi-

tion, applying the zero flux boundary condition (2.5) we obtain (2.38). This yields an additional $\frac{M}{2}$ equations.

Using the transmission conditions (2.50) and (2.51) results in

$$\sum_{j=1}^{2N} c_j G(\underline{\xi}_j, \underline{x}_i) - \sum_{j=2N+1}^{3N} c_j G(\underline{\xi}_j, \underline{x}_i) = 0, \quad i = \overline{M+1, 2M} \tag{2.62}$$

and

$$\sum_{j=1}^{2N} c_j G'(\underline{\xi}_j, \underline{x}_i) - \hat{K} \sum_{j=2N+1}^{3N} c_j G'(\underline{\xi}_j, \underline{x}_i) = 0, \quad i = \overline{2M+1, 3M}, \tag{2.63}$$

respectively. These give $2M$ equations.

Finally, by imposing the condition (2.6), yields one more equation

$$\sum_{i=1}^{2M} \sum_{j=1}^{2N} c_j G(\underline{\xi}_j, \underline{x}_i) = 0. \tag{2.64}$$

Again, to find the solution of the CEM problem (2.2), (2.5) and (2.48)-(2.51) using the MFS, the equations (2.60)-(2.64) are reformulated in the following matrix form as a $(3M+1) \times 3N$ linear system of algebraic equations:

$$F\underline{c} = \underline{b}. \tag{2.65}$$

The least-squares method is used to solve the system of equations (2.65). This yields the solution (2.24).

Example 5. Solve the problem (2.2), (2.5) and (2.48)-(2.51) using the BEM and MFS with the same input data as in Example 1 and $\gamma = 2$.

BEM solution: The matrix D in equation (2.58) is given by

$$D_{i,l} = \begin{cases} B_{i,l} & \text{if } l = \overline{1, 2M}, \\ A_{i,l} & \text{if } l = \overline{(2M+1), 4M}, \end{cases} \quad i = \overline{1, 2M},$$

and

$$D_{i,l} = \begin{cases} \tilde{B}_{i,l} & \text{if } l = \overline{M+1, 2M}, \\ \tilde{A}_{i,l} & \text{if } l = \overline{(3M+1), 4M}, \\ 0 & \text{if } l = \overline{1, M} \cup \overline{(2M+1), 3M}, \end{cases} \qquad i = \overline{(2M+1), 3M}.$$

Using equations (2.55)-(2.57) we obtain

$$D_{i,l} = \begin{cases} -\frac{h}{\ell_1} & \text{if } (i-3M) \neq l, l = \overline{1, M/4}, \\ (1 - \frac{h}{\ell_1}) & \text{if } (i-3M) = l, l = \overline{1, M/4}, \\ 0 & \text{if } l = \overline{(M/4+1), 2M} \cup \overline{(3M+1), 4M}, \\ z_1 \delta_{i,l} & \text{if } l = \overline{(2M+1), 3M}, \end{cases}$$

$$i = \overline{(3M+1), (3M+M/4)},$$

$$D_{i,l} = \begin{cases} -\frac{h}{\ell_2} & \text{if } (i-3M) \neq l, l = \overline{(M/2+1), 3M/4}, \\ (1 - \frac{h}{\ell_2}) & \text{if } (i-3M) = l, l = \overline{(M/2+1), 3M/4}, \\ 0 & \text{if } l = \overline{1, M/2} \cup \overline{(3M/4+1), M} \cup \overline{(3M+1), 4M}, \\ z_2 \delta_{i,l} & \text{if } l = \overline{(2M+1), 3M}, \end{cases}$$

$$i = \overline{(3M + M/2 + 1), (3M + 3M/4)},$$

$$D_{i,l} = \delta_{i,l}, \quad \text{if } l = \overline{(2M+1), 3M},$$

$$i = \overline{(3M + M/4 + 1), (M + M/2)} \cup \overline{(2M + 3M/4 + 1), 4M}.$$

The last row in the matrix D is given by

$$D_{(4M+1),l} = \begin{cases} 1 & \text{if } l = \overline{1, M}, \\ 0 & \text{if } l = \overline{M+1, 4M}. \end{cases}$$

Furthermore, the vector $\underline{b}$ is given by (2.41).

MFS solution: Turning now to the MFS solution, the first M rows of the matrix F in equation (2.65) are the same as those of the matrix F in Example 1. Moreover, another M rows are generated by applying the inner boundary condition (2.62), namely,

$$F_{i,j} = G_{i,j}, \;\; i = \overline{(M+1), 2M}, \;\; j = \overline{1, 2N},$$

$$F_{i,j} = -G_{i,j-N}, \;\; i = \overline{(M+1), 2M}, \;\; j = \overline{2N+1, 3N}.$$

Another M rows in the matrix F are obtained from (2.63) as

$$F_{i,j} = G'_{i,j}, \;\; i = \overline{(2M+1), 3M}, \;\; j = \overline{1, 2N},$$

$$F_{i,j} = 2G'_{i,j-N}, \;\; i = \overline{(2M+1), 3M}, \;\; j = \overline{2N+1, 3N}.$$

Finally, the last row in the matrix F is obtained from (2.64) as

$$F_{(3M+1),j} = \sum_{i=1}^{2M} G_{i,j}, \quad j = \overline{1, N},$$

$$F_{(3M+1),j} = 0, \quad j = \overline{N+1, 3N}.$$

Similarly, the vector $\underline{b}$ of the linear system of equations (2.65) is given by (2.42).
In the MFS we take $R = 1.15$, $R_1 = 0.45$ and $R_2 = 0.55$.

Figures 2.16-2.19 present a comparison between the BEM and MFS solutions for the boundary data $u_{Outer}(1, \theta)$, $u_{Inner}(0.5, \theta)$, $(\partial u/\partial n)_{Outer}(1, \theta)$ and

$(\partial u/\partial n)_{Inner}(0.5,\theta)$, respectively. The same conclusions as in Example 3 can be drawn by observing these figures.

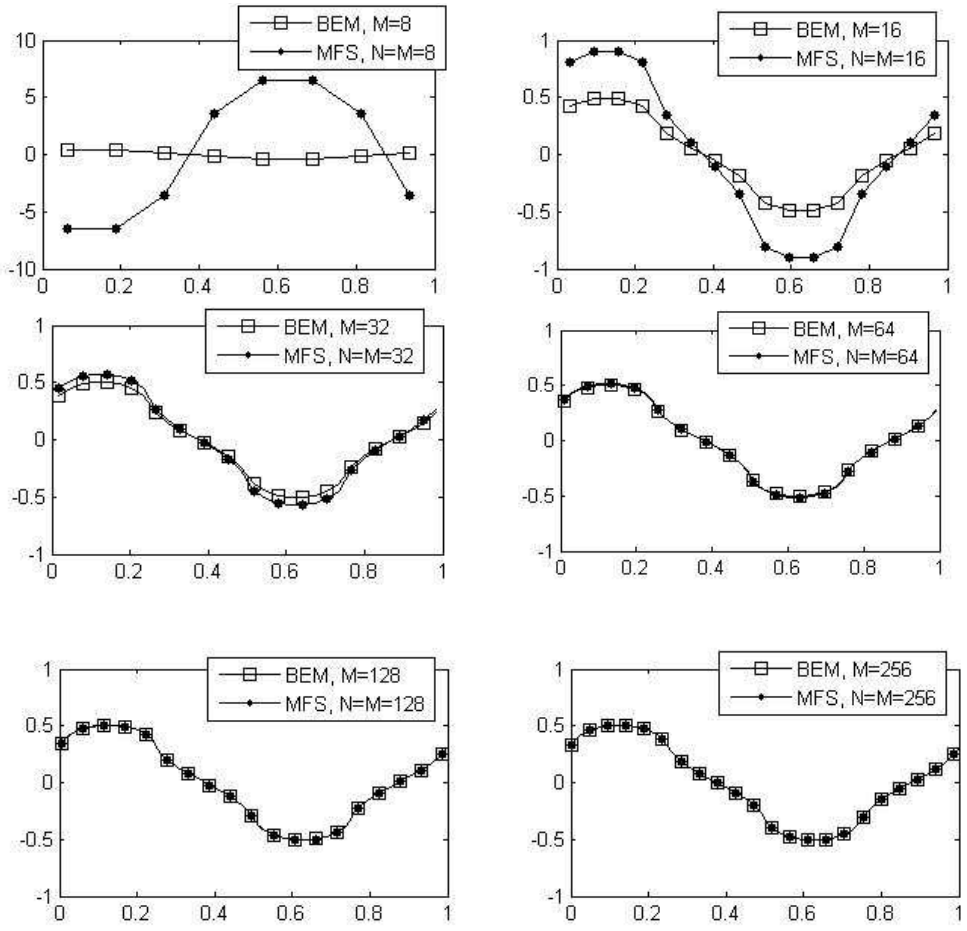

Figure 2.16: Comparison between $u_{Outer}^{MFS}(1,\theta)$ and $u_{Outer}^{BEM}(1,\theta)$, as functions of $\theta/(2\pi)$, for Example 5.

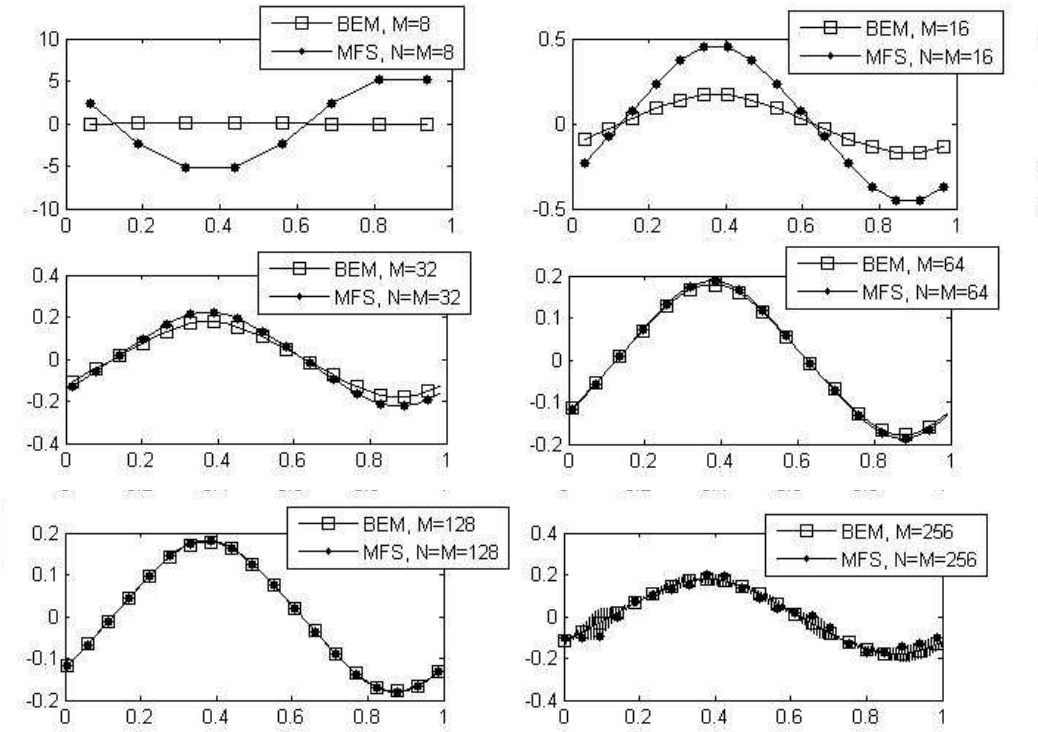

Figure 2.17: Comparison between $u_{Inner}^{MFS}(0.5,\theta)$ and $u_{Inner}^{BEM}(0.5,\theta)$, as functions of $\theta/(2\pi)$, for Example 5.

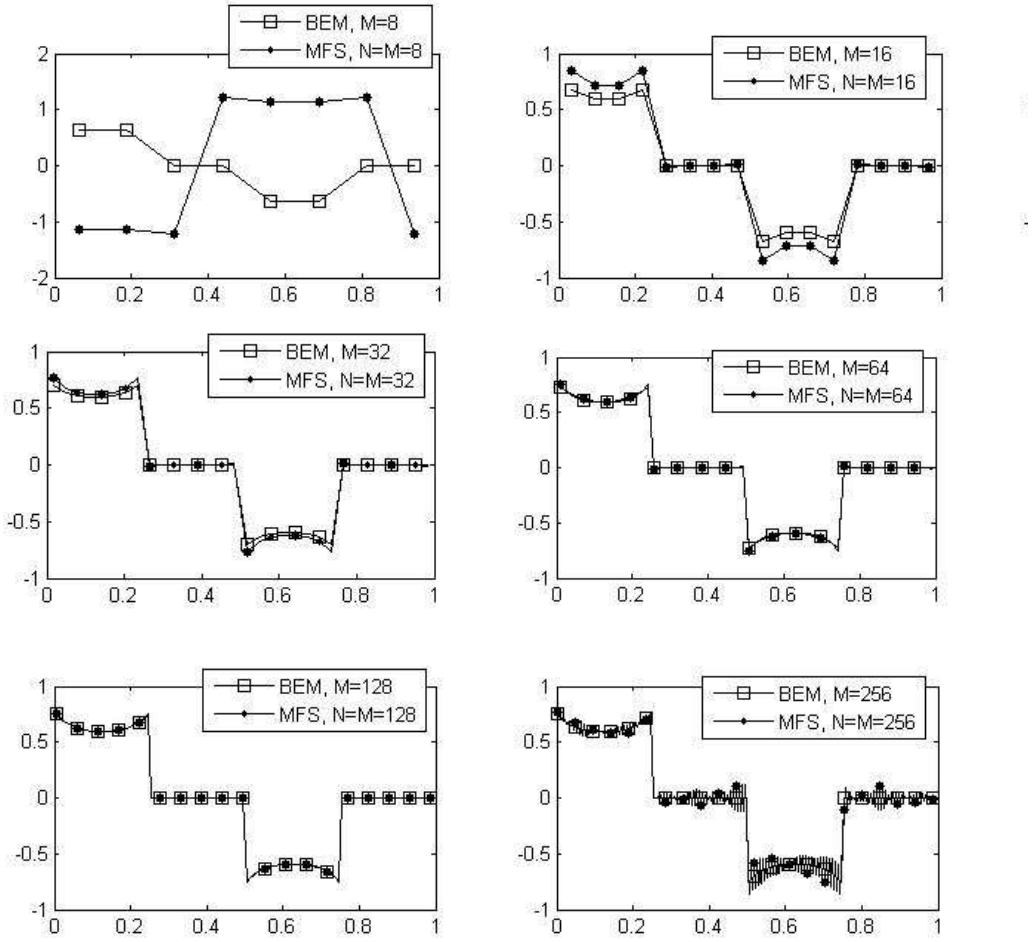

Figure 2.18: Comparison between $(\frac{\partial u}{\partial n})_{Outer}^{MFS}(1,\theta)$ and $(\frac{\partial u}{\partial n})_{Outer}^{BEM}(1,\theta)$, as functions of $\theta/(2\pi)$, for Example 5.

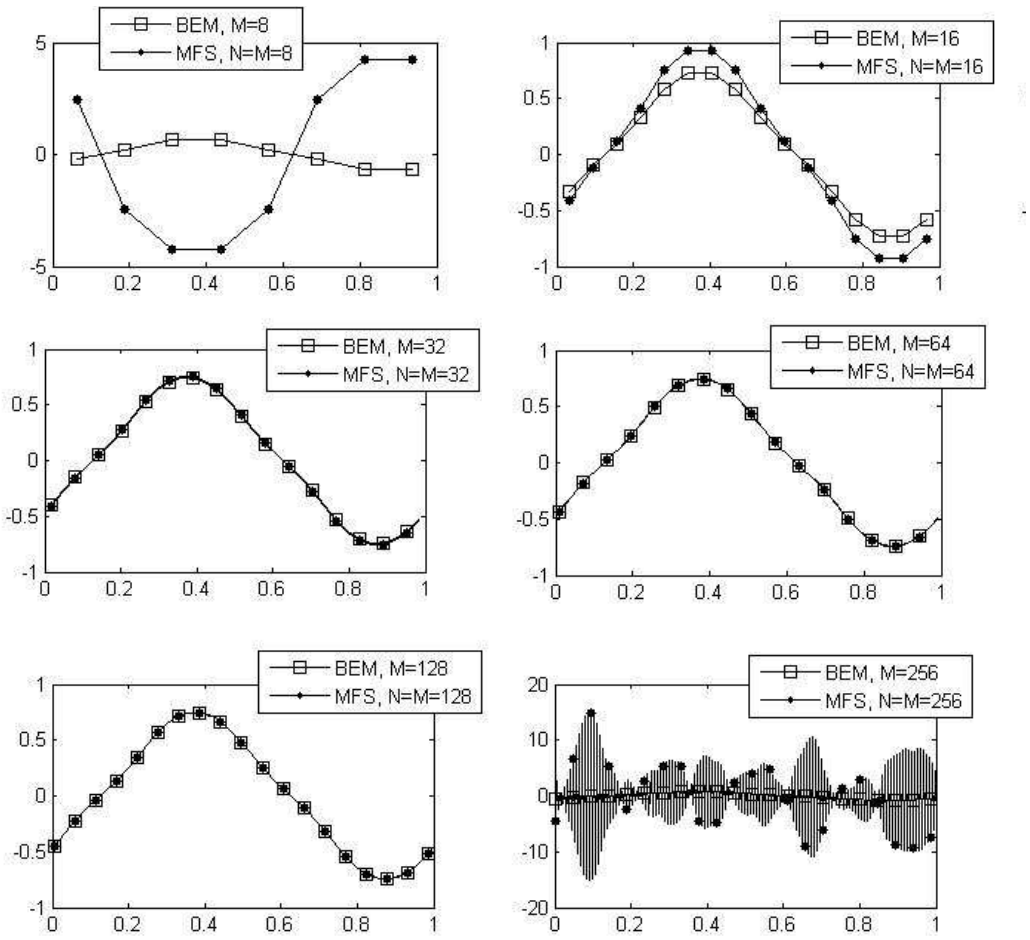

Figure 2.19: Comparison between $(\frac{\partial u}{\partial n})_{Inner}^{MFS}(0.5,\theta)$ and $(\frac{\partial u}{\partial n})_{Inner}^{BEM}(0.5,\theta)$, as functions of $\theta/(2\pi)$, for Example 5.

2.8 Conclusions

This chapter has applied and compared the BEM and MFS to solve direct CEM problem of ERT. These two numerical methods were examined for various simply and multiply-connected domains with various homogeneous boundary conditions on the inner boundary in the latter case. Due to the lack of an analytical solution, the BEM solution has been considered as the 'exact' solution because it is more accurate than the one obtained using the MFS which gives some instability when the degrees of freedom become too large. The boundary integrals involved in the BEM have been evaluated

analytically. As far as the computational time is concerned, both the BEM and the MFS require almost the same modest amount of time (mainly used to invert the linear systems of equations (2.16) or (2.23)); e.g. 3, 5 and 30 seconds for $M \in \{64, 128, 256\}$ boundary elements, respectively. Another interesting point to make is that in the MFS we have experimented with various values of $R > 1$ and have found that R between 1.01 and 1.15 produces the most accurate results. For larger values of R, the MFS accuracy decreases showing that the harmonic function u outside the unit disk domain Ω has reached its limit, i.e. the circle of radius R captured in its interior a singularity of u. The nature of the Robin boundary condition (2.2) and, in general, the sophisticated CEM makes it difficult to predict analytically beforehand where the singularities of u lie in the exterior of Ω. In any case, R should be chosen less than the magnitude of the position vector of the nearest singularity to the origin. Although the MFS has produced unstable solutions for large degrees of freedom, such as $M = N = 256$, for lower values its accuracy and stability are excellent when compared to the BEM numerical solution. Moreover, the MFS is much easier to implement than the BEM especially in three-dimensional problems in irregular domains.

In the rest of the thesis, the MFS developed in this chapter will be applied and combined with statistical inversion methods for solving several inverse problems of ERT/EIT.

Chapter 3

Identification of rigid inclusions in the complete-electrode model of ERT

3.1 Introduction

In various applications of EIT, such as medical imaging or geophysics, the purpose is to reconstruct the conductivity within a region, which might be the human body or a geographical area, using some non-invasive electrical measurements which are taken on the surface of the region, [66]. This task can be achieved by attaching electrodes to the outside boundary of the region. Then, currents are injected through the electrodes and simultaneously voltages between electrodes are recorded. Using these voltages as a data set to estimate the interior conductivity distribution is an ill-posed non-linear inverse problem, which needs to be regularized in order to obtain a stable and reliable solution. An alternative framework is offered by the Bayesian approach which is an explicit statistical method widely used in image analysis [28, 30]. Within the reconstruction process, and for data simulation, voltages can be calculated using the solution of Laplace's equation, as described in [34], and here the MFS is used to solve this direct problem numerically, [26].

In Section 3.2, the mathematical formulation is considered; that is, a brief descrip-

tion is given of the MFS for solving the direct problem of the CEM of ERT in a domain containing a rigid inclusion. Then, the Bayesian statistical modeling approach and the MCMC estimation technique will be discussed in Section 3.3. Finally, in Section 3.4 some examples, representing numerically simulated experiments, will be examined thoroughly to demonstrate the effectiveness and accuracy of the proposed procedures.

3.2 Mathematical formulation

In this section, the mathematical models for the direct and inverse ERT problems are formulated. We consider solving Laplace's equation in a two-dimensional doubly-connected bounded domain $\Omega \backslash \Omega_{Inner}$ of uniform unit conductivity, namely,

$$\bigtriangledown^2 u = 0, \qquad \text{in } \Omega \backslash \Omega_{Inner} \tag{3.1}$$

subject to certain boundary conditions which makes the problem the so-called 'complete-electrode model' (CEM), [61]. In this model, on the boundary $\partial\Omega$ there are attached L electrodes, ε_p, for $p = \overline{1, L}$. On the boundary $\partial\Omega$ we also have the boundary conditions (2.2), (2.5) and (2.6).

Assuming that Ω_{Inner} is a perfectly conductive rigid inclusion having infinite (or at least very large) conductivity we have the homogeneous Dirichlet boundary condition

$$u = 0 \qquad \text{on } \partial\Omega_{Inner}. \tag{3.2}$$

Insulated cavities over which $\partial u/\partial n = 0$ on $\partial\Omega_{Inner}$ can also be considered.

Equations (2.2), (2.5), (2.6), (3.1) and (3.2) represent the direct problem of ERT in the domain Ω containing a rigid inclusion Ω_{Inner}.

3.2.1 MFS for the direct problem

The MFS for solving the direct problem (2.2), (2.5), (2.6), (3.1) and (3.2) is described in Subsection 2.6.2.

For illustrative purposes, let us take $M = N = 128$, $R = 1.15$, $R_1 = 0.45$ and $L = 4$, and consider two current patterns, namely,

$$I_p = \begin{cases} 1 & \text{if } p = 1, \\ -1 & \text{if } p = 4, \\ 0 & \text{if } p \in \{2, 3\}, \end{cases} \tag{3.3}$$

and

$$I_p = \begin{cases} 1 & \text{if } p = 1, \\ -1 & \text{if } p = 3, \\ 0 & \text{if } p \in \{2, 4\}. \end{cases} \tag{3.4}$$

Figures 3.1(a) and 3.1(b) show the comparison between the MFS solutions for the boundary potential $u(1, \theta)$ and the current flux $(\partial u/\partial n)(1, \theta)$, respectively, for the current patterns (3.3) and (3.4).

(a)

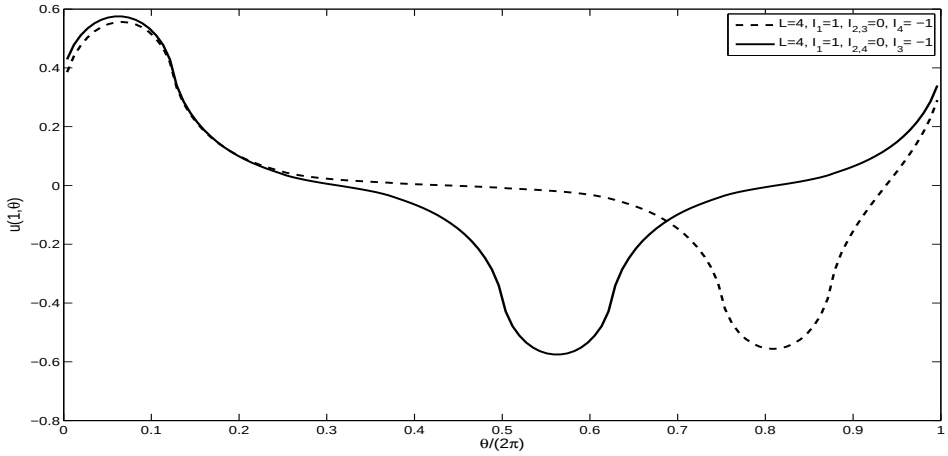

(b)

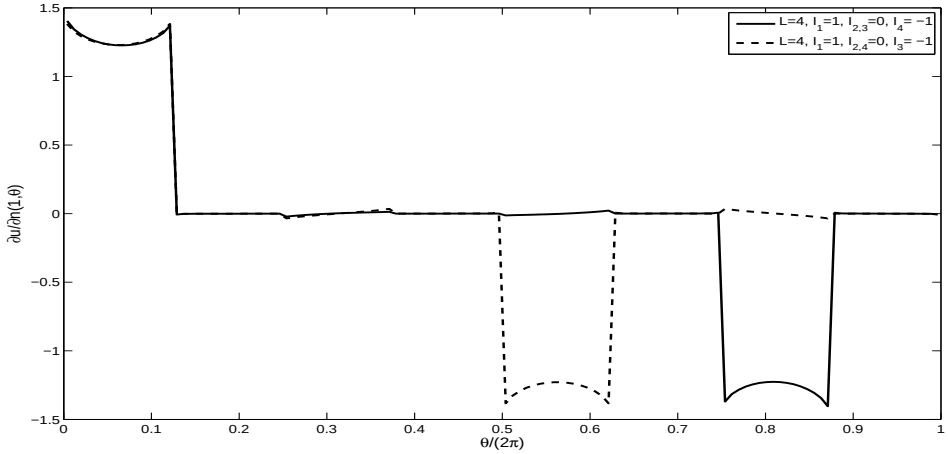

Figure 3.1: Comparison between the solutions for (a) $u\,(1,\theta)$ and (b) $\partial u/\partial n\,(1,\theta)$, for the current patterns (3.3) and (3.4).

Figure 3.2 shows the approximate equipotential lines of the MFS solutions $u\,(r,\theta)$, where $r \in (0.5,1)$ and $\theta \in [0,2\pi)$, for the current patterns (3.3) and (3.4). From this figure it can be seen that when the current is injected in the first electrode and drawn out though the fourth electrode the equipotential lines which originate on the right side of the domain do not fill the left side of the domain. Whilst when the current is injected in the first electrode, and drawn out through the third electrode, the equipotential lines

which originate on the top-right and bottom-left sides of the domain fill the top-left and bottom-right side of that domain.

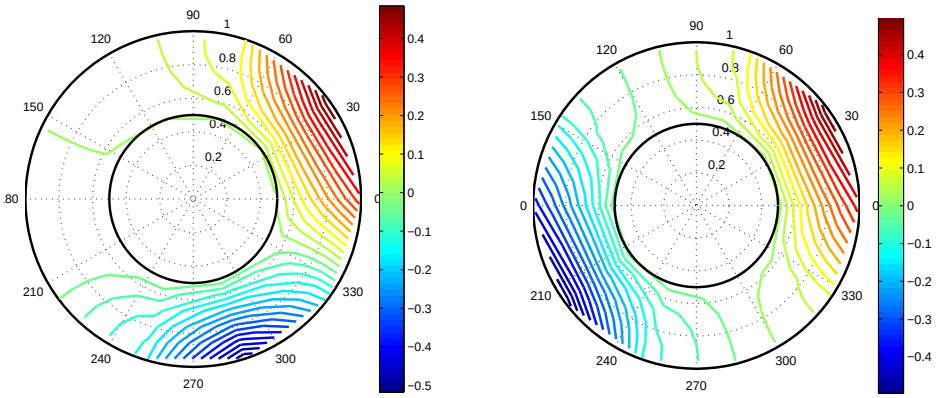

Figure 3.2: Equipotential lines of the interior solution $u\,(r,\theta)$ for the current patterns (3.3) (left) and (3.4) (right).

Figures 3.3(a) and 3.3(b) show a comparison between the MFS solutions for the boundary potential $u(1,\theta)$ and the current flux $(\partial u/\partial n)(1,\theta)$, respectively, when the numbers of the attached electrodes are $L = 2$ and $L = 4$. In the case $L = 4$ we take the current pattern (3.4), whilst in the case $L = 2$ we take the current pattern $I_1 = 1$ and $I_2 = -1$.

(a)

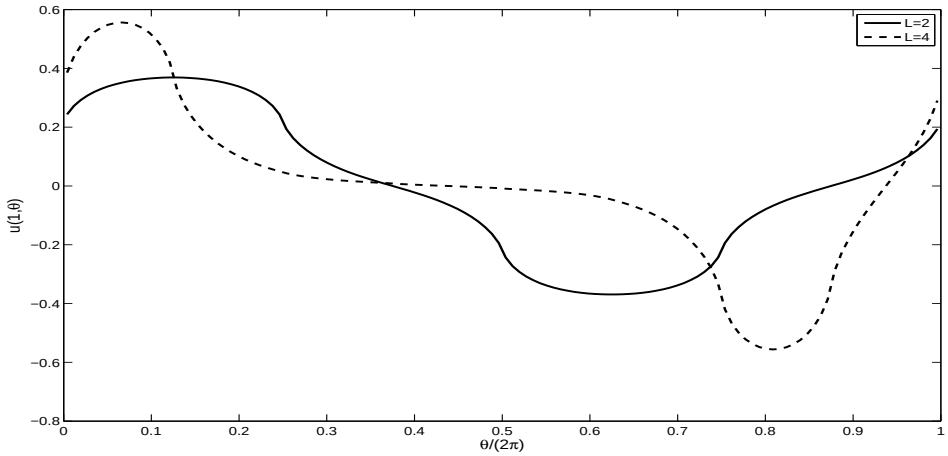

(b)

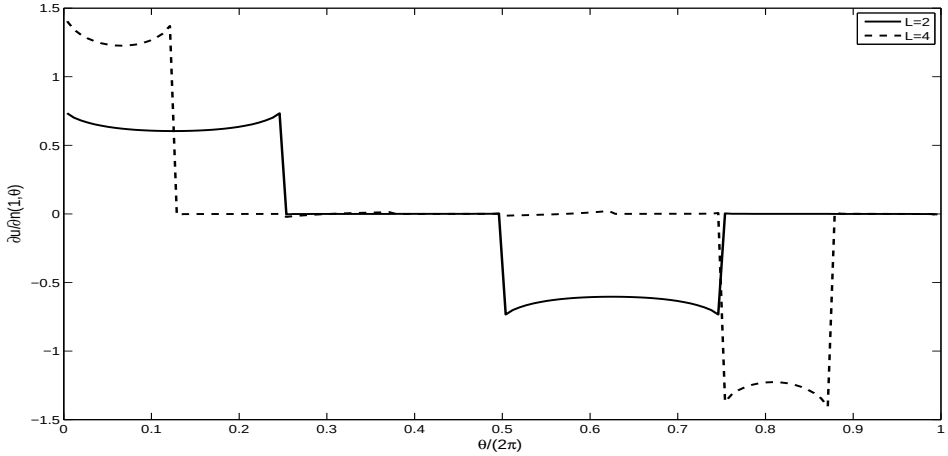

Figure 3.3: Comparison between the solutions for $(a)\ u\,(1,\theta)$ and $(b)\ \partial u/\partial n\,(1,\theta)$, as functions of $\theta/(2\pi)$, for $L = 2$ and 4 electrodes.

Elliptical Rigid Inclusion

Consider an elliptic rigid inclusion $\Omega_{Inner} = \left\{(x,y) \in \mathbb{R}^2 \mid \frac{x^2}{a^2} + \frac{y^2}{b^2} < 1\right\}$. If $a = b$, then Ω_{Inner} is circle, If $a > b$, then Ω_{Inner} is a horizontal ellipse, otherwise Ω_{Inner} is a vertical ellipse. The polar coordinates of the ellipse are $x = a\cos(\theta)$ and $y = b\sin(\theta)$.

As a result, the radius is

$$r(\theta) = \frac{ab}{\sqrt{\left(b\cos(\theta)\right)^2 + \left(a\sin(\theta)\right)^2}}, \quad \theta \in [0, 2\pi), \tag{3.5}$$

and its derivative is

$$r'(\theta) = \frac{ab(b^2 - a^2)\cos(\theta)\sin(\theta)}{\left(\left(b\cos(\theta)\right)^2 + \left(a\sin(\theta)\right)^2\right)^{3/2}}, \quad \theta \in [0, 2\pi). \tag{3.6}$$

In equations (2.38) and (2.39), and for the internal points $(x, y) \in \partial\Omega_{Inner}$, the $\frac{\partial G}{\partial n}$ is changed to

$$\frac{\partial G}{\partial n}(\underline{\xi}_j, \underline{x}) = \frac{\partial G}{\partial x} n_x + \frac{\partial G}{\partial y} n_y, \quad \underline{x} = (x, y) \in \partial\Omega_{Inner}, \tag{3.7}$$

where

$$\frac{\partial G}{\partial x}(\underline{\xi}_j, \underline{x}) = -\frac{-(x - \xi_j^1)}{2\pi|\underline{\xi}_j - \underline{x}|^2}, \quad \frac{\partial G}{\partial y}(\underline{\xi}_j, \underline{x}) = -\frac{-(y - \xi_j^2)}{2\pi|\underline{\xi}_j - \underline{x}|^2}. \quad j = \overline{1, 2N},$$

$$n_x = \frac{-\left(r'(\theta)\sin(\theta) + r(\theta)\cos(\theta)\right)}{\sqrt{r(\theta)^2 + r'(\theta)^2}}, \quad n_y = \frac{r'(\theta)\cos(\theta) + r(\theta)\sin(\theta)}{\sqrt{r(\theta)^2 + r'(\theta)^2}}.$$

Bean-shaped Rigid Inclusion

A more complicated geometry for the internal object $\partial\Omega_{Inner}$ is considered here, which is a bean-shape inclusion described in [6, 7, 40] and defined by the radial parameterization

$$r(\theta) = \frac{0.5 + 0.4\cos\theta + 0.1\sin 2\theta}{0.1 + 0.7\cos\theta}, \quad \theta \in [0, 2\pi). \tag{3.8}$$

Its derivative is

$$r'(\theta) = \frac{-5\sin\theta + 40\cos^2\theta - 20 + 14\cos^3\theta}{100 + 140\cos\theta + 49\cos^2\theta}, \quad \theta \in [0, 2\pi), \tag{3.9}$$

where $\theta \in [0, 2\pi)$ hence, equations (3.5) and (3.6) is replaced by (3.8) and (3.9) when using the MFS to solve forward EIT problem in an annular domain with bean-shaped rigid inclusion.

Direct Solver Comparison

We compare the boundary potential $u(1, \theta)$ and current flux $(\partial u/\partial n)(1, \theta)$, on the outer boundary $\partial\Omega$, obtained from the circular, elliptical and bean-shaped objects Ω_{Inner}. We apply the MFS when the number of attached electrodes is $L = 2$, and both the number of collocation points M and the number of degrees of freedom points N are equal with $M = N = 128$. The contraction parameter $\eta_I = 0.9$ and dilation parameter $\eta_E = 1.15$ determine the locations of the sources; this means how close, or far, the internal/external source points are from the inner/outer boundary, respectively. We have, [36, 40],

$$(\text{The radii of the internal source points}) = \eta_I \times (\text{radii of the inclusion})$$

and

$$(\text{The radii of the external source points}) = \eta_E \times (\text{radii of the unit disk}).$$

Figures 3.4(a) and 3.4(b) show the comparison between the outer potential and current flux for various shapes of rigid inclusion. From Figure 3.4(a), it can be seen that the curve corresponding to the boundary potential function resulting from the inner horizontal elliptical object shows a small movement to the right in comparison to that obtained from the inner circular object. Whilst the curve of the boundary potential function produced when the domain contains the vertical elliptical object illustrates an

equal movement to the left, comparing to that obtained from the circular object. We finally observe that the boundary potential function resulting from the bean-shaped object shows a very substantial difference to the corresponding function from the circular object.

Figure 3.4 (b) shows the corresponding normal derivative $\partial u/\partial n\,(1,\theta)$ on the boundary $\partial\Omega$ for various shapes of rigid inclusions as in Figure 3.4(a). From this figure, it can be seen that there are only small changes in the boundary current flux function values obtained from the inner bean or horizontal/vertical elliptical object comparing to the ones obtained from the circular object. More precisely, on the first electrode, the values of the horizontal ellipse function are greater that those of the circle, whilst the the values of the vertical ellipse function are smaller, before reaching the mid-interval where they intersect and swap roles afterwards, until they reach 0.25. On the second attached electrode, the values of the horizontal ellipse function are smaller that those of the circle, whilst the values of the vertical ellipse function are greater, before reaching the mid-interval where they intersect on the second attached electrode and swap roles afterwards, until they reach 0.75.

(a)

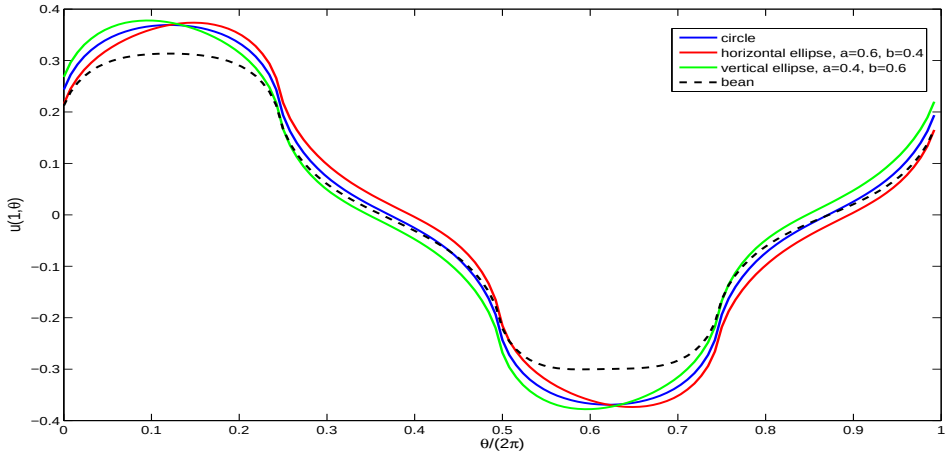

(b)

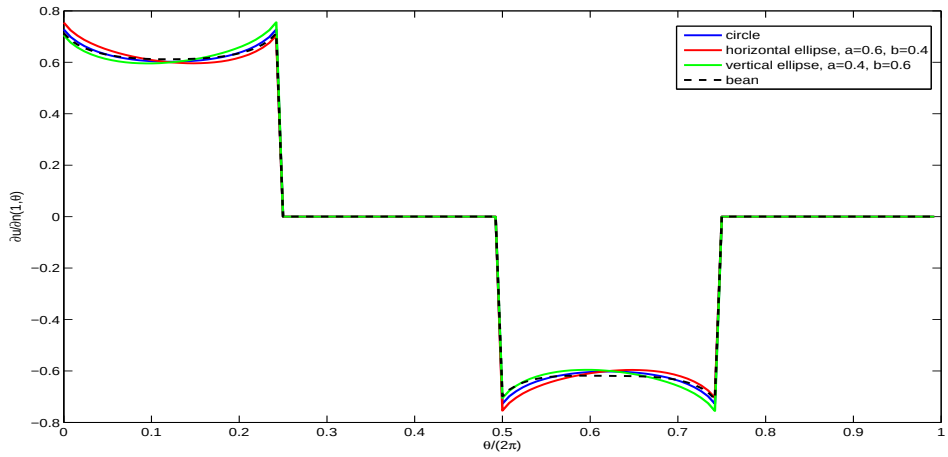

Figure 3.4: Comparison between (a) the boundary potentials $u\,(1,\theta)$ and (b) the normal derivatives $\partial u/\partial n\,(1,\theta)$, as functions of $\theta/(2\pi)$, for various shapes of rigid inclusions.

3.3 Statistical approach

The general strategy behind the statistical approach is to recast the inverse problem in the form of a statistical inference problem. Throughout this description, the aim is to solve the same inverse problem defined above concerning the identification of the shape, position and size of a rigid inclusion $\partial\Omega_{Inner}$ which is compactly embedded

in the host medium Ω. The goal of the statistical approach is to incorporate as much information as possible about these quantities from all sources, including subjective knowledge as well as data measurements. The uncertainty in the value of all random quantities must be modelled in terms of probability distributions. In brief, the solution of the inverse problem is then given by the most likely model parameter values based on the appropriate probability distribution, but the probabilistic nature means that it is also possible to assess model reliability through probability statements such as credible intervals, for more details see [34]. Central to this inference is the posterior distribution which is obtained from a likelihood combined with a prior distribution using Bayes theorem, details of this procedure are stated in Subsection 3.3.1. Background to the Markov chain Monte Carlo algorithm (MCMC), which permits numerical solution of the statistical inference problem, is provided in Subsection 3.3.2. Although there is no explicit solution of the inverse problem, the MCMC algorithm does make extensive use of the direct numerical solver described in Subsection 3.2.1. This approach allows us not only to image the reconstruction, but also to deeply examine the reliability and uncertainty of that estimation.

Initially, a noisy data set of boundary potential $u(1,\theta)$ and current flux $\partial u/\partial n(1,\theta)$ is simulated based on the MFS. This data set can be written as

$$w_j = u(x_j) + \eta_j, \quad v_j = \frac{\partial u}{\partial n}(x_j) + \zeta_j, \quad j = \overline{1,N}, \tag{3.10}$$

where the additive noise variables η_j and ζ_j follow independent Gaussian distributions which have zero means and variances σ_w^2 and σ_v^2, respectively. This leads to data $\underline{w} = (w_j)_{j=\overline{1,N}}$ and $\underline{v} = (v_j)_{j=\overline{1,N}}$. The Gaussian distribution is widely used to model and describe several kinds of natural variability, [7, 67], and has been used elsewhere for ERT data. Later we shall solve the inverse problem using voltage data (2.4) which, when perturbed by noise, is given as

$$T_p = U_p + \psi_p, \quad p = \overline{1,L}, \tag{3.11}$$

where ψ_p are Gaussian noise variables with mean zero and variance σ_T^2, leading to data $\underline{T} = (T_p)_{p=\overline{1,L}}$.

3.3.1 Statistical modelling

In order to detect Ω_{Inner}, assumed to be star-shaped, i. e.,

$$\Omega_{Inner} = \{r(\theta)\,(\cos(\theta), \sin(\theta))\,|0 < r(\theta) < 1, \theta \in [0, 2\pi]\}, \tag{3.12}$$

contained in the domain Ω (assumed to be the unit disk), the MFS coefficients $\underline{c} = (c_k)_{k=\overline{1,2M}}$ and the radii

$$r_i = r(2\pi i/M), \quad i = \overline{1, M}, \tag{3.13}$$

must be estimated. These are the parameters of the model.

First, by supposing the independence of $\underline{w}$ and $\underline{v}$ given $\underline{r}$ and $\underline{c}$, a suitable decomposition of the likelihood is given by the Bayes theorem which states that

$$l(\underline{w}, \underline{v}|\underline{r}, \underline{c}) = l(\underline{w}|\underline{r}, \underline{c}) \times l(\underline{v}|\underline{r}, \underline{c}). \tag{3.14}$$

The inexactness in the measured data (3.10), and other uncontrolled sources of variation which can appear during the experiment, are quantified by the likelihood, see [67], with

$$l(\underline{w}|\underline{r}, \underline{c}) = (2\pi\sigma_w^2)^{-N/2}\ \exp\left\{-\frac{1}{2\sigma_w^2}\,\|\underline{w} - \underline{\tilde{w}}(\underline{r}, \underline{c})\|^2\right\}, \tag{3.15}$$

and

$$l(\underline{v}|\underline{r}, \underline{c}) = (2\pi\sigma_v^2)^{-N/2}\ \exp\left\{-\frac{1}{2\sigma_v^2}\,\|\underline{v} - \underline{\tilde{v}}(\underline{r}, \underline{c})\|^2\right\} \tag{3.16}$$

These likelihoods are the conditional distributions of $\underline{w}$ and $\underline{v}$ given $\underline{r}$ and $\underline{c}$, since $\underline{w}|\underline{r},\underline{c} \sim \mathcal{N}\left(\underline{\tilde{w}}(\underline{r},\underline{c}), \sigma_w^2 I\right)$ and $\underline{v}|\underline{r},\underline{c} \sim \mathcal{N}\left(\underline{\tilde{v}}(\underline{r},\underline{c}), \sigma_v^2 I\right)$. Moreover,
$\underline{\tilde{w}}(\underline{r},\underline{c}) = \left(\tilde{w}_j(\underline{r},\underline{c})\right)_{j=\overline{1,N}}$ are the calculated boundary potential values and $\tilde{\mathrm{v}}(\underline{r},\underline{c}) = \left(\tilde{v}_j(\underline{r},\underline{c})\right)_{j=\overline{1,N}}$ are the calculated current flux values when the radii of the object are $\underline{r}$ and the MFS coefficients are $\underline{c}$.

Secondly, when the voltage data is used, the likelihood is

$$l(\underline{T}|\underline{r},\underline{c}) = (2\pi\sigma_T^2)^{-L/2} \exp\left\{-\frac{1}{2\sigma_T^2}\left\|\underline{T} - \underline{\tilde{T}}(\underline{r},\underline{c})\right\|^2\right\}, \tag{3.17}$$

where $\underline{\tilde{T}}(\underline{r},\underline{c}) = \left(\tilde{T}_p(\underline{r},\underline{c})\right)_{p=\overline{1,L}}$ are the calculated voltage values when the radii of the object are $\underline{r}$ and the MFS coefficients are $\underline{c}$. The following models will be defined in terms of data $(\underline{w},\underline{v})$, but equally apply to data $\underline{T}$ by replacing $l(\underline{w}|\underline{r},\underline{c}) \times l(\underline{v}|\underline{r},\underline{c})$ by $l(\underline{T}|\underline{r},\underline{c})$.

In general, finding the estimates of the model parameters, that is the rigid inclusion, from only the likelihood, may not be achievable because the inverse problem is ill-conditioned in terms of the discrete set of MFS coefficients $\underline{c}$ and there is also ill-posedness and non-linearity between the measured data and the radii $\underline{r}$ of the inclusion. In standard approaches, regularization is usually employed to overcome these difficulties. However, the reconstruction can only be found as a point estimate and fails to provide us with any information related to confidence statements. That is why, an alternative method based on the framework of Bayesian statistical modeling is considered. This method is represented by likelihood, prior and the resulting posterior distribution. Here, a prior assumption that the boundary around the internal object is gently varying, inspires smoothness. As a result, the prior distribution is defined as

$$\pi(\underline{r}|\beta_r) = (2\pi\beta_r^2)^{-M/2} \exp\left\{-\frac{1}{2\beta_r^2}\left\|\bigtriangledown\underline{r}\right\|^2\right\}, \tag{3.18}$$

where β_r^2 describes the amount of variation between adjacent radii, and the norm $\left\|\bigtriangledown\underline{r}\right\|^2 = \sum_{i=1}^{M}\left(r_i - r_{i-1}\right)^2$ is the first-order smoothing finite-difference, with the

convention that $r_0 = r_M$.

Similarly, the same prior distribution can be applied to the MFS coefficients to provide the prior distribution

$$\pi(\underline{c}|\beta_c) = (2\pi{\beta_c}^2)^{-N/2} \exp\left\{-\frac{1}{2\beta_c^2}\left\|\bigtriangledown\underline{c}\right\|^2\right\}. \tag{3.19}$$

Combination of the likelihood functions (3.15) and (3.16) with the prior distributions (3.18) and (3.19) results in the posterior distribution

$$\pi(\underline{r},\underline{c}|\underline{w},\underline{v}) \propto l(\underline{w}|\underline{r},\underline{c})l(\underline{v}|\underline{r},\underline{c}) \times \pi(\underline{r}|\beta_r)\pi(\underline{c}|\beta_c). \tag{3.20}$$

The likelihood function describes the relationship between the data $\underline{w}, \underline{v}$ and the parameters $\underline{r}, \underline{c}$ (that is, how likely is the data given the model that uses these parameters). Whilst, the prior distribution describes the relationship between the model parameters before data is considered (that is how likely the parameter values are when data has not yet been observed, or in other words an initial guess for the parameter values), [7]. Now, since the prior parameters β_r and β_c are not known they should be involved in the estimation process as well. We use hyper-prior (improper) distribution for these prior parameters are given as

$$\pi(\beta_r) \propto \exp\left\{-\frac{\alpha_r^2}{2\beta_r^2}\right\}, \tag{3.21}$$

and

$$\pi(\beta_c) \propto \exp\left\{-\frac{\alpha_c^2}{2\beta_c^2}\right\}. \tag{3.22}$$

The full posterior distributions can then be rewritten as

$$\pi(\underline{r},\underline{c},\beta_r,\beta_c|\underline{w},\underline{v}) \propto l(\underline{w}|\underline{r},\underline{c})l(\underline{v}|\underline{r},\underline{c}) \times \pi(\underline{r}|\beta_r)\pi(\beta_r) \times \pi(\underline{c}|\beta_c)\pi(\beta_c). \tag{3.23}$$

There are two different sets of MFS coefficients $\underline{c} = (\underline{c}_I, \underline{c}_E)$, those relating to the inner source points and the others which are linked to the outer source points. This suggests separating the prior distributions into $\pi(\underline{c}_I|\beta_{c_I})$ and $\pi(\underline{c}_E|\beta_{c_E})$, as well as separating the hyper-prior distributions into $\pi(\beta_{c_I})$ and $\pi(\beta_{c_E})$, which have separate hyper-prior parameters α_{c_I} and α_{c_E}, respectively. Then also write $\beta_c = (\beta_{cI}, \beta_{cE})$.

To conclude, the final full posterior distribution, which is again defined as the product of the likelihood functions, the various prior distributions and corresponding hyper-prior distributions, is

$$\begin{aligned}\pi(\underline{r}, \underline{c}, \beta_r, \beta_{c_I}, \beta_{c_E}|\underline{w}, \underline{v}) \propto l(\underline{w}|\underline{r}, \underline{c})l(\underline{v}|\underline{r}, \underline{c}) \times \pi(\underline{r}|\beta_r)\pi(\beta_r) \\ \times\pi(\underline{c}_I|\beta_{c_I})\pi(\beta_{c_I}) \times \pi(\underline{c}_E|\beta_{c_E})\pi(\beta_{c_E}). \qquad (3.24)\end{aligned}$$

Figure 3.5 illustrates the hierarchical relationship between fixed data and fixed prior parameters (boxes), and the model parameters which need to be estimated (circles). In the central and the right panels of Figure 3.5, the prior smoothing parameters need to be estimated in addition to the MFS coefficients and the radii values (right). This is achievable by fixing the hyper-prior parameters at some appropriate values. Whilst, in the left panel the values of the prior smoothing parameters are fixed with estimation of only the MFS coefficients and the object radii. We may need to separate the β_c into β_{cI} and β_{cE} corresponding to the inner and the outer source points so that the inner and the outer MFS coefficients will be better estimated when the values of β_{cI} and β_{cE} are not equal. Consequently, this change requires α_c to be separated into α_{cI} and α_{cE}, as well.

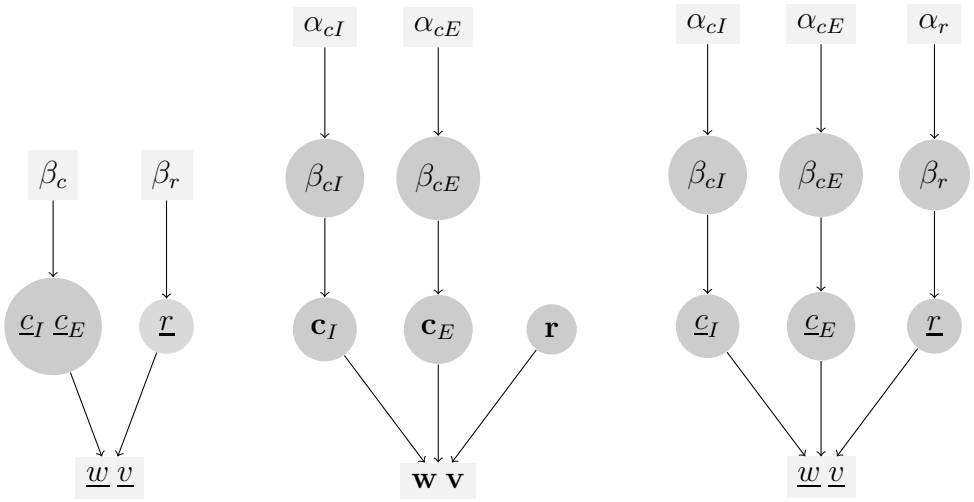

Figure 3.5: Hierarchical structure of the model.

3.3.2 Markov Chain Monte Carlo estimation

Although the history of Markov chain Monte Carlo (MCMC) started in the late 1940s, it has not been used effectively in statistics until the early 1990s. During the 1990s this technique had a remarkable development and nowadays the MCMC approach is widely used for many estimation problems due to the valuable advantages which it has. For example, it is very convenient to use MCMC estimation if the modeling is complicated and the dimension of the parameter space is large since these cases make the use of standard numerical methods infeasible. Moreover, it allows deep analysis of the posterior distribution, not only calculation of parameter estimates and standard deviations. Here plots of boundary histograms and credible intervals corresponding to the object boundaries will be used, [34].

Once, the posterior distribution of the parameters is defined, it is possible to use the Metropolis-Hastings algorithm, a special case of the general MCMC approach, to produce approximate samples from it by simulating a Markov chain. Throughout this procedure, the Markov chain has the parameter set to be estimated as its state variables, and the equilibrium distribution is required to exist and be equal to the posterior distribution, see [4]. The MCMC method is not an estimation technique itself, but it gives a

framework to produce tailor-made iterative algorithms which can be used to study the properties of the posterior distribution. This algorithm, as output, provides a correlated sample from the posterior distribution. The MCMC method is based on two important statistical ideas, these are Markov chains and rejection sampling. The first technique gives the 'candidate' values and the second tests these values. The transitions in the Markov chain are designed precisely to make an equilibrium distribution exist and which is equal to the target distribution. If the transitions in the Markov chain are planned well, then after an initial transient period, known as burn-in, the values which pass the test have the same statistical properties as if they had been taken from the posterior distribution itself. Due to the nature of Markov chains, however, there will be some correlation in the sample which must be taken into account when producing the summary of the output. On the other hand, if the initial transient period is long and the sample is highly correlated, then using the MCMC method is inefficient and larger samples are required to obtain accurate and reliable estimation. To conclude, designing the algorithm carefully means that the final reconstruction does not rely on the initial starting values of the parameters and the initial shape of the inclusion.

Let all the parameters, which have already been defined, be put in a single vector, $\underline{B} = (B_i)_{i=\overline{1,p}}$. For example, $\underline{B} = (\underline{r}, \underline{c})$, $\underline{B} = (\underline{r}, \underline{c}, \beta_r, \beta_c)$ or $\underline{B} = (\underline{r}, \underline{c}, \beta_r, \beta_{c_I}, \beta_{c_E})$, where the initial guess of the radii is chosen to form the best fitted circle for the inner inclusion and the initial values for the MFS coefficient parameters are selected to be zero.

The Metropolis-Hastings procedure can be briefly described in the following steps:

Set an arbitrary value for $\underline{B}$, say $\underline{B}^0$

Repeat the next steps for $k = \overline{1, K}$, where K is the desired sample size

Repeat the next steps for $i = \overline{1, p}$

Suggest a new value for the i-th parameter, $B_i^k = B_i^{k-1} + \mathcal{N}(0, \tau^2)$ giving proposal parameter vector $\underline{B}^k = (B_1^k, ..., B_i^k, B_{i+1}^{k-1}, ..., B_p^{k-1})$

Evaluate $\alpha = \min\{1, \pi(\underline{B}^k|\underline{w}, \underline{v})/\pi(\underline{B}^{k-1}|\underline{w}, \underline{v})\}$

Generate u from the uniform distribution, $\mathcal{U}(0, 1)$

If $\alpha > u$ then accept the suggested value, otherwise reject it and set $B_i^k = B_i^{k-1}$

End repeat

End repeat

Discard initial values and use remainder to make inference

A reasonable choice for the proposal variance, τ^2, can be made after running some initial experiments. It must be neither too big nor too small to avoid the long transient period and a highly correlated sample, [6, 7]. It has been proven theoretically in [54] that the optimal acceptance rate is 23.4%, for various problems of high dimensions. Moreover, it is also worth examining the Markov chain paths and investigating sample autocorrelation functions. For reasonable performance, the paths should appear random and the autocorrelation functions should be nearly zero for all except small lags, [2, 6, 7]. For more applications of MCMC to EIT, see [66, 67].

3.4 Numerical results and discussion

In this section, we will reconstruct a star-shaped rigid inclusion in a series of experiments based on simulated data. These data are either the boundary potential $\underline{w}$ and the current flux $\underline{v}$ on $\partial\Omega$ (Section 3.4.1) or, the voltages $\underline{T}$ on the electrodes (Section 3.4.2). The measurements are obtained by solving the CEM direct problem of ERT given by equations (2.2), (2.5), (2.6), (3.1) and (3.2) using the MFS, as described in Chapter 2. Moreover, it is worth mentioning that all data are corrupted by additive Gaussian noise with zero mean and standard deviation $\sigma = 0.01$.

The geometries considered in the experiments are circular or elliptical inclusions. The data simulation technique starts by obtaining the MFS coefficients $\underline{c}$ which are

divided in two different sets. The first group consists of $N = 128$ external MFS coefficients $\underline{c}_E$ related to the $N = 128$ equally-spaced source points located outside the domain Ω. Whilst, the second set consists of $N = 128$ internal MFS coefficients $\underline{c}_I$ related to the $N = 128$ equally-spaced source points, located inside the rigid inclusion Ω_{Inner}. Then, both sets of MFS coefficients are used to calculate the potential and the current flux, which are also used along with (2.4) to calculate the voltages.

3.4.1 Using the boundary potential and current flux data

In the following experiments, the simulated data are the boundary potential and the current flux at 30 equally-spaced points on the outer fixed boundary $\partial\Omega$ when the number of the collocation points on each boundary $\partial\Omega$ and $\partial\Omega_{Inner}$ is $M = 128$ and the number of the electrodes is $L = 2$ or 4.

The Truth Object is a Circle

In the following a single current pattern is injected through $L = 2$ electrodes with

$$I_p = \begin{cases} 1 & \text{if } p = 1, \\ -1 & \text{if } p = 2, \end{cases} \tag{3.25}$$

then u and $\partial u/\partial n$ have been plotted earlier in Figure 3.3. The following models of estimation will be considered.

Case 1: Fitting the simplest possible model (which is a circular object) including only a single unknown radius, $\underline{r} \in (0, 1)$, in addition to the unknown MFS coefficients, $\underline{c}$.

Experiment 1. Based on results from similar numerical experiments using the MFS and the Bayesian approach for shape estimation of objects, but solving the continuous inverse model of EIT, [7], the hyper-parameter values are fixed at $\alpha_{C_I} = 0.0116$ and

$\alpha_{C_E} = 0.2457$ for the internal and external MFS coefficients, respectively. This is the situation described in the central panel in Figure 3.5 because the prior smoothing parameters β_{C_I}, β_{C_E} are being estimated. The MCMC algorithm is implemented with $K = 2000$ iterations, where the first 1000 define the burn-in period.

Figure 3.6 illustrates the estimated object and the MFS coefficients. It can be seen that the accuracy of the reconstruction is very good with the estimated radius of 0.5017, compared to the true value of 0.5, and with a standard deviation of 0.0030. In addition to this, the MFS coefficients which are linked to the source points of the inner boundary keep track with the exact values and have narrow credible intervals. Whilst the estimated MFS coefficients for the source points of the outer boundary show some smoothness with wider credible intervals, which means greater uncertainty than the other coefficients.

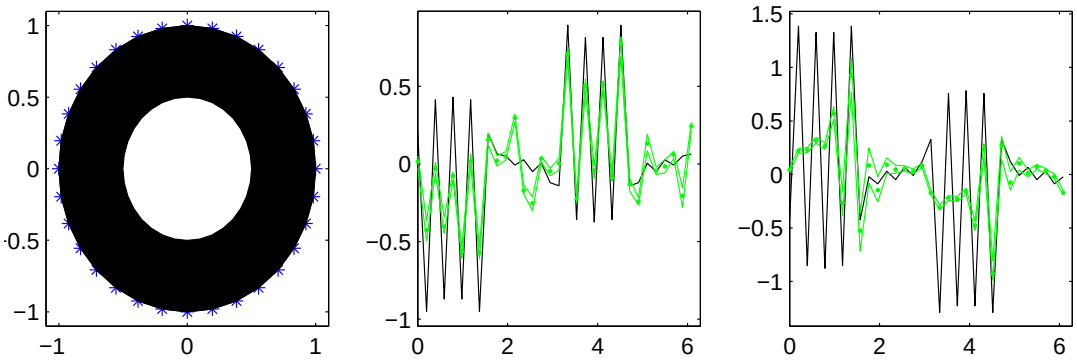

Figure 3.6: Circle model with full posterior distribution: fitted circle (left) and MFS coefficients along with credible intervals corresponding to the inner (middle) and outer (right) boundaries. Herein and throughout, in the second the third pictures with green lines we denote the retrieved MFS coefficients with the creditable intervals whilst the black lines represent the MFS coefficients obtained from the direct problem.

Figure 3.7 illustrates that the reconstruction of the circular object is extremely good since the estimation errors, which are defined as the difference between the true and estimated radii, cannot be seen on the left-hand graph. The middle and right-hand figures show a circular histogram and circular credible interval, respectively. The purpose of

these is to represent estimation variability. The darker areas of the histogram indicate the higher frequencies and the annular thickness of the credible interval refers to the amount of variation.

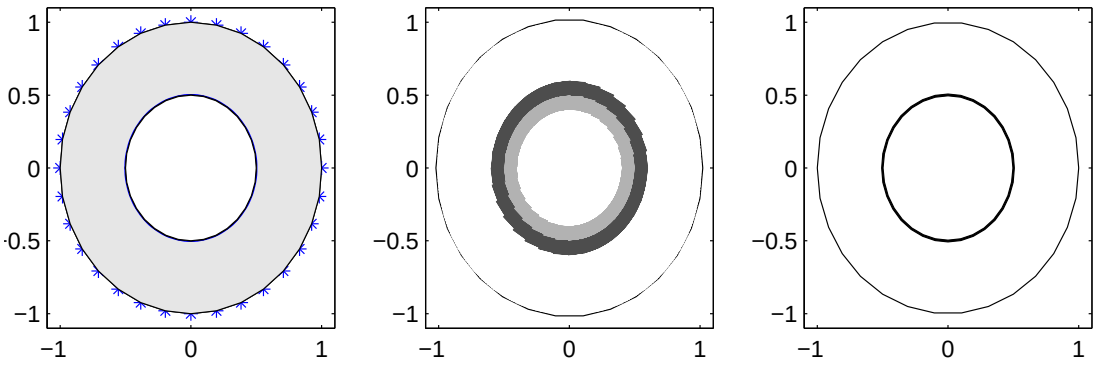

Figure 3.7: Circle model with full posterior distribution with prior parameters ($\alpha_r = 1.0$, $\alpha_{C_I} = 0.0116$ and $\alpha_{C_I} = 0.2457$): error estimates (left), object boundary histogram (middle) and object boundary credible interval (right).

Case 2: Fitting a more general model (which is a star-shaped object) that includes 32 radii, $\underline{r}$, at equally-spaced angles, in addition to the unknown MFS coefficients, $\underline{c}$.

Experiment 2. The hyper-prior parameters, α_{C_I} and α_{C_E}, are the same as in the previous experiment with $\alpha_r = 1.0$ used for the radius hyper-parameter. This is the situation described in the right-hand panel in the Figure 3.5 because the prior smoothing parameters β_{C_I}, β_{C_E} and β_r are being estimated.

Figure 3.8 displays the object reconstruction which seems to be reasonable all around the object except at two small parts of the boundary. The largest error can be described as an outward bump positioned in the top-left part of the reconstruction, whilst the other smaller error is an inward bump located in the bottom-right side. The graphs in the middle and right show the internal MFS coefficient estimation following the true values (the black continuous line) with narrow credible intervals, but clearly those associated with the internal source points are better estimated that those associated with the external source points.

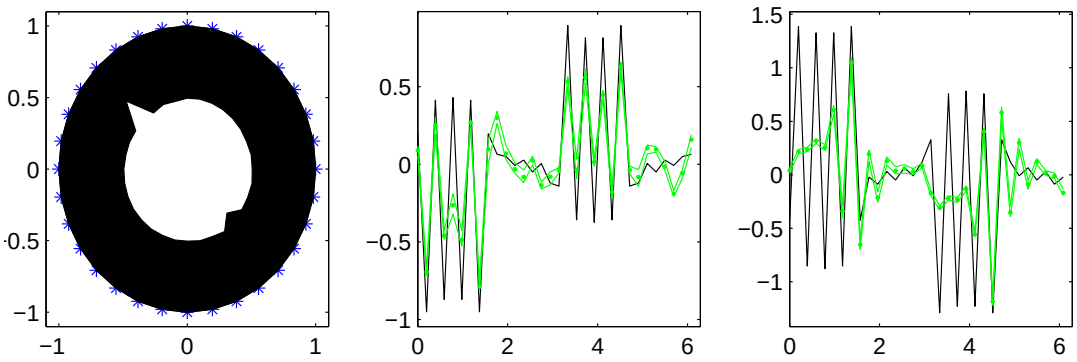

Figure 3.8: Star-shape model with full posterior distribution: fitted shape (left) and MFS coefficients along with reliable intervals corresponding to the inner (middle) and outer (right) boundaries.

Figure 3.9 shows the accuracy and the variability in the object reconstruction. Here, the average of the estimated radii is 0.5161 with a standard deviation of 0.0049. Overall, the errors in the left graph are quite small, however the estimated errors are more substantial in the top-left of the reconstructed object, followed by those which are located in the bottom-right. This is even more clearly represented in the annular thickness of the credible interval graph. This pattern is due to the position of the electrodes. The currents are injected through the first electrode, which is located in the top-right part of the outer boundary, and exit from the second electrode which is located in the bottom-left part. This makes the equipotential lines cover the whole domain (see Figure 3.2) except, importantly, in the small parts which have the bumps.

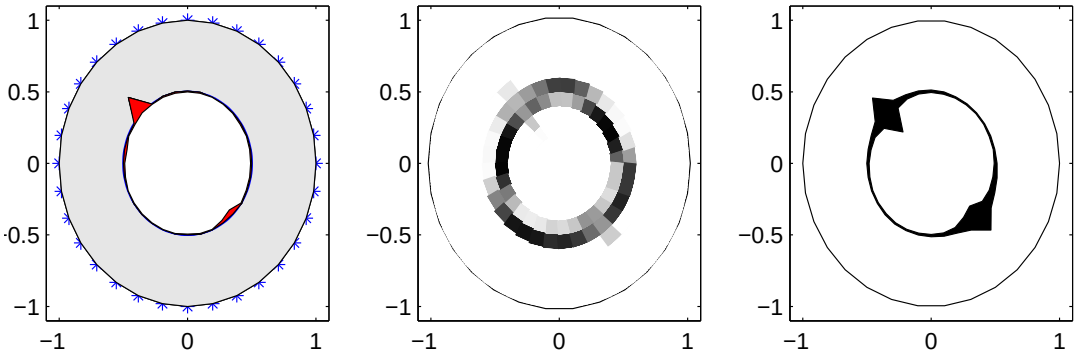

Figure 3.9: Star-shape model with full posterior distribution with prior parameters ($\alpha_r = 1.0$, $\alpha_{C_I} = 0.0116$ and $\alpha_{C_E} = 0.2457$): error estimates (left), object boundary histogram (middle) and object boundary credible interval (right).

Figure 3.10 shows the posterior histograms for the prior radii smoothing parameter and the prior MFS smoothing parameters. It can be seen that the average of the prior smoothing parameter for the radii is $\hat{\beta}_r = 0.2611$ (the standard deviation is 0.0334) and the posterior estimates of the inner and outer MFS smoothing parameters are $\hat{\beta}_{C_I} = 0.5104$ and $\hat{\beta}_{C_E} = 0.7390$ (the standard deviations are 0.0667 and 0.1172, respectively). It is also obvious from the posterior histograms that there is substantial variation in the smoothing parameter of the radius $\hat{\beta}_r$ which means it may not be well estimated. In addition, the variation in the smoothing parameter of the inner MFS coefficients $\hat{\beta}_{C_I}$ is reasonably small which indicates it is well-estimated. However, the smoothing parameter of the outer MFS coefficients $\hat{\beta}_{C_E}$ shows much more variability. Also, the histograms of the parameters are slightly positive skew.

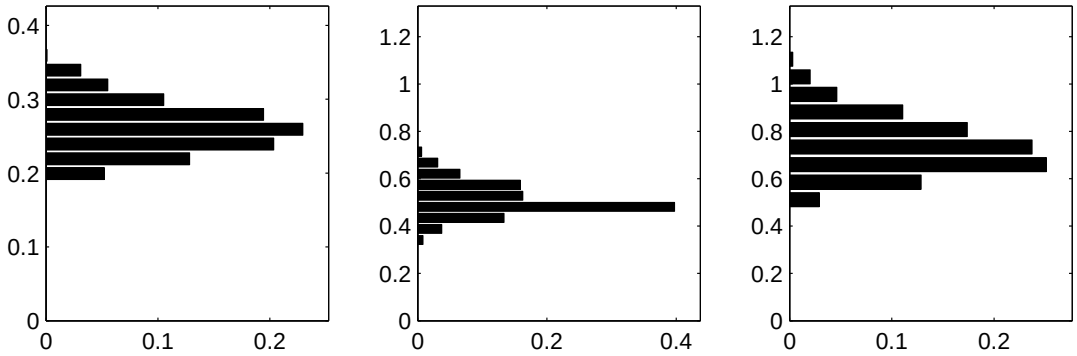

Figure 3.10: Star-shape model with full posterior distribution and prior parameter information: histograms for the radius (left) and the MFS inner (middle) and outer (right) boundary coefficients.

In order to see the effect of running the MCMC algorithm for further iterations, the calulations are re-started using the posterior estimates as initial values. So that the initial values of β_r, β_{C_I} and β_{C_E} are changed to 0.2611, 0.5104 and 0.7390, respectively.

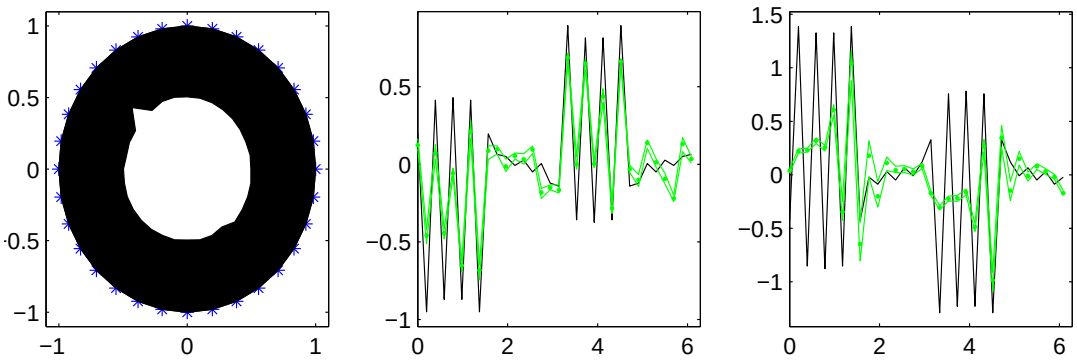

Figure 3.11: Star-shape model with full posterior distribution and separated prior information: fitted shape (left) and MFS coefficients (with credible intervals) corresponding to the inner (middle) and outer (right) boundaries.

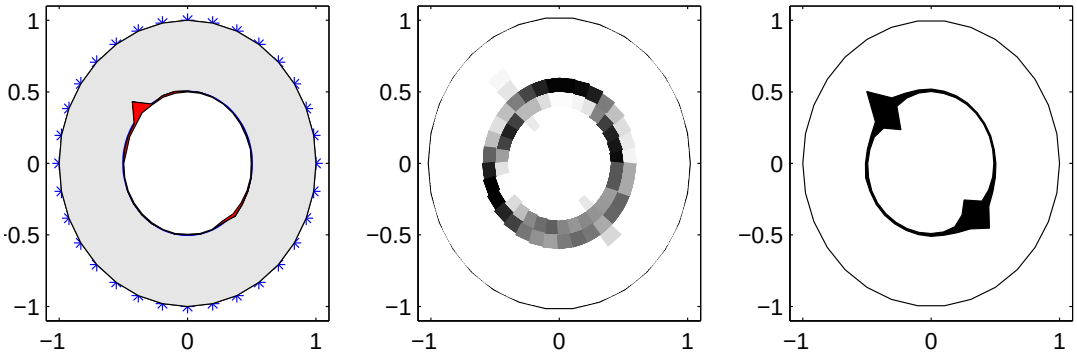

Figure 3.12: Star-shape model with full posterior distribution with prior parameters ($\beta_r = 0.2611,\ \alpha_r = 1.0,\ \beta_{C_I} = 0.5104,\ \alpha_{C_I} = 0.0116$ and $\beta_{C_E} = 0.7390,\ \alpha_{C_E} = 0.2457$): error estimates (left), object boundary histogram (middle) and object boundary credible interval (right).

All in all, Figures 3.11 and 3.12 show more accurate reconstruction than the previous example although the estimation errors are still greater in the top-left followed by the bottom right than elsewhere around the reconstructed object and the estimated radii average is 0.4953 with an estimated standard deviation of 0.0039.

Experiment 3. In this experiment, running with $\alpha_r = 1.0$, as in the previous two experiments, did not produce the same good performance. Thus, we decided here to take a smaller value for α_r, say $\alpha_r = 0.1$, which was also suggested in [6]. This results in better reconstruction with a new estimated radii average of 0.5012 and a standard deviation 0.0038. This is clearly shown by comparing Figures 3.13 and 3.14 with Figures 3.11 and 3.12.

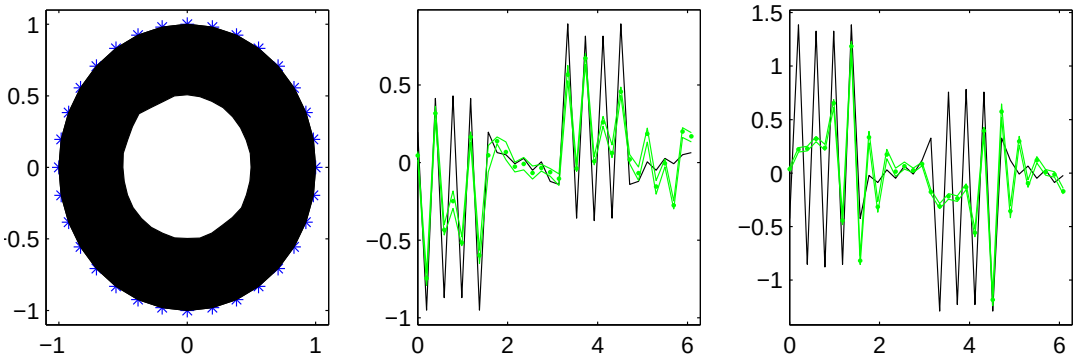

Figure 3.13: Star-shape model with full posterior distribution and separated prior information: fitted circle (left) and MFS coefficients (with credible intervals) corresponding to the inner (middle) and outer (right) boundaries.

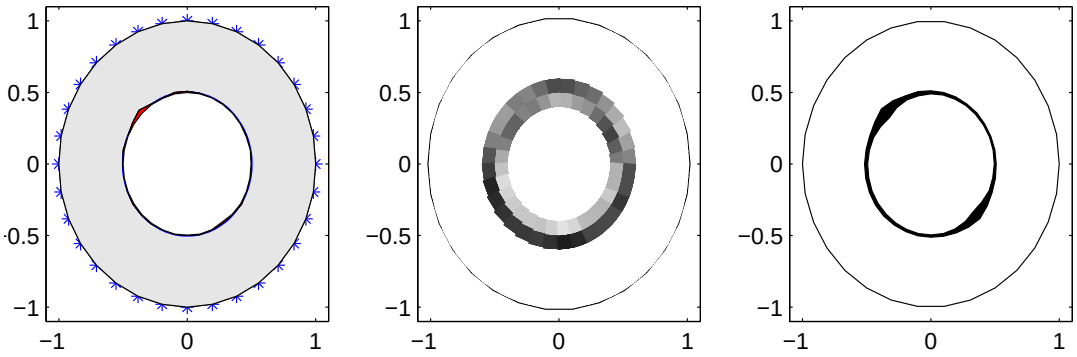

Figure 3.14: Star-shape model with full posterior distribution with prior parameters ($\beta_r = 0.2611,\ \alpha_r = 0.1$, $\beta_{C_I} = 0.5104,\ \alpha_{C_I} = 0.0116$ and $\beta_{C_E} = 0.7390,\ \alpha_{C_E} = 0.2457$): errors estimation (left), object boundary histogram (middle) and object boundary credible interval (right).

The True Object is an Ellipse

To further test the estimation approach, we describe the reconstruction of a series of inclusions given by ellipses defined by the following:

$$\Omega_{Inner} = \left\{ (x,y) \in \mathbb{R}^2 \middle| \frac{x^2}{(0.5+\epsilon)^2} + \frac{y^2}{(0.5-\epsilon)^2} < 1 \right\},$$

where $\epsilon = \{\pm 0.1, \pm 0.2\}$.

Experiment 4. We fit a star-shape model using elliptical true data with the same hyper-prior parameter values as in Experiment 3, when $L = 2$.

In Figure 3.15, the green part shows that the reconstructed shape is smaller than the true inclusion, whilst the red part illustrates the opposite. From the same figure, it can be seen that as $|\epsilon|$ is increased, the accuracy of the estimation becomes lower whatever the orientation of the ellipse, horizontal or vertical. For instance, the estimation graphs (left) show smaller errors when $\epsilon = \pm 0.1$ than when $\epsilon = \pm 0.2$. Moreover, the histograms and the credible interval graphs show nearly elliptical reconstructions when $\epsilon = \pm 0.1$. Also, the estimated MFS coefficients follow the true values better when $\epsilon = \pm 0.1$ than when $\epsilon = \pm 0.2$.

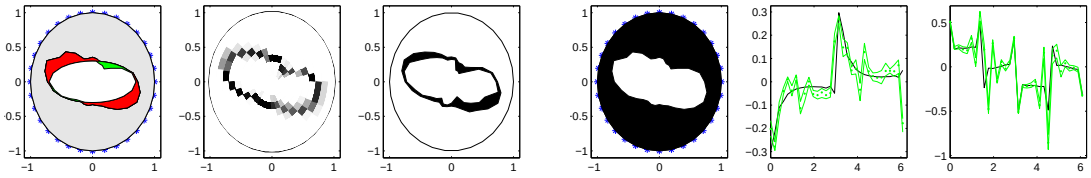

$\epsilon = +0.2$

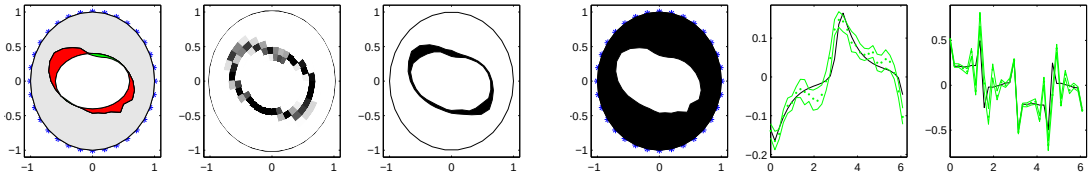

$\epsilon = +0.1$

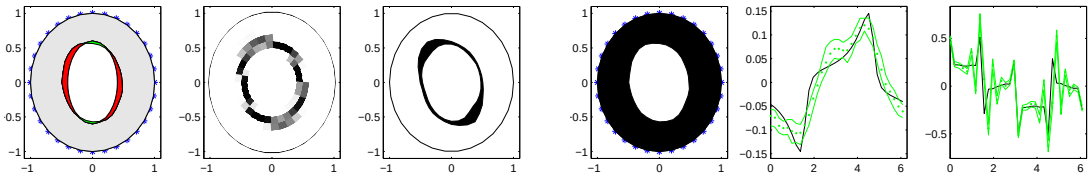

$\epsilon = -0.1$

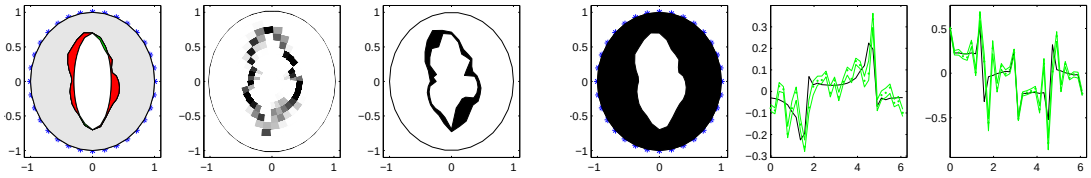

$\epsilon = -0.2$

Figure 3.15: Star-shape model with the hyper-prior parameters as in Figure 3.14. Errors estimation (left), object boundary histogram, object boundary credible interval, fitted ellipse, MFS coefficients (with credible intervals) corresponding to the inner and outer boundaries (right).

3.4.2 Using the voltage data

In this section, we use the voltages T_p, for $p = \overline{1, L}$, based on the annular domain with a rigid circular or elliptical inclusion. These voltages are used as data instead of the potential $\underline{w} = (w_j)_{j=\overline{1,N}} = u\,(1, \theta)$ and the current flux $\underline{v} = (v_j)_{j=\overline{1,N}} = \frac{\partial u}{\partial n}\,(1, \theta)$.

To begin with, the number of the electrodes is $L = 4$ and up to three different pat-

terns of the injected currents are considered.

Case 1: In this case a single current pattern is considered where we inject current via two opposite electrodes, as in equation (3.4). In this case, only one ERT direct problem is solved to obtain four voltages.

Case 2: In this case two current patterns are considered where we inject the current pattern (3.4), as well as another current pattern given by

$$I_p = \begin{cases} 1 & \text{if } p = 1, \\ -1 & \text{if } p = 2, \\ 0 & \text{if } p \in \{3, 4\}. \end{cases} \tag{3.26}$$

Solving these two ERT direct problems results in eight voltages.

Case 3: In this case, three current patterns are considered where we inject using the current patterns (3.3), (3.4) and (3.26). This means that three ERT direct problems are solved to obtain twelve voltages.

It is useful to first compare the direct solutions when circular and elliptical inclusions are considered. Figures 3.16(a) and 3.16(b) illustrate a comparison between the MFS solutions for the boundary potential $u(1, \theta)$ and the current flux $(\partial u/\partial n)(1, \theta)$, respectively, when the numbers of electrodes is $L = 4$, and the inner circular, horizontal and vertical elliptical inclusions are considered. From Figure 3.16(a), it can be seen that there are small variations in the boundary potential function values obtained from the horizontal/vertical elliptical inclusions compared to the one obtained from the circular inclusion. Whilst in Figure 3.16(b), the values of boundary current flux functions of horizontal, vertical and circular rigid inclusions are almost the same.

(a)

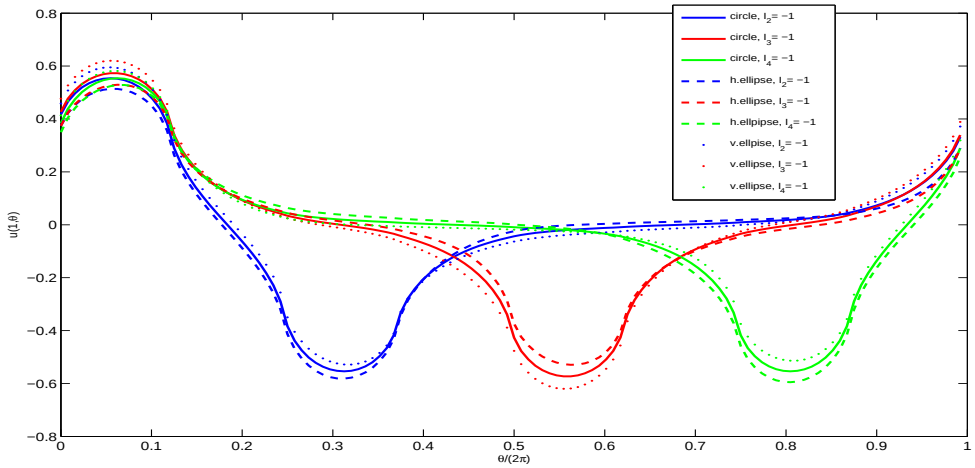

(b)

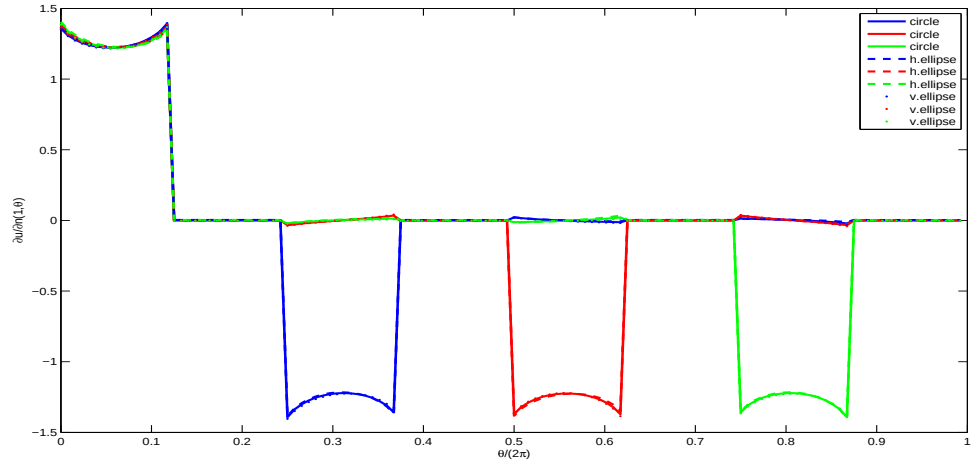

Figure 3.16: Comparison between (a) boundary potentials $(1, \theta)$ and (b) the normal derivatives $\partial u/\partial n\,(1, \theta)$, as functions of $\theta/(2\pi)$, for the current patterns (3.26), (3.4) and (3.3).

The True Object is a Circle

Experiment 5. We fit a circular object model to reconstruct a circular rigid inclusion.

Firstly, we solve the inverse ERT problem in Case 1 and consider that the target object is a circle of radius 0.5 centred at the origin. So, only one single radius needs

to be determined, as well as the 128 internal MFS coefficients and 128 external MFS coefficients, and with $\eta_I = 0.9$ and $\eta_E = 1.15$. The hyper-prior parameter of the internal and external MFS coefficients are fixed at $\alpha_{C_I} = 0.1160$ and $\alpha_{C_E} = 2.4570$, respectively, as in Experiment 3.

Figures 3.17 and 3.18 illustrate the object and the MFS coefficient estimation. It can be seen that the reconstruction of the object shows a different circle with radius equal to 0.6738 and a standard deviation of 0.0080. This is because in Experiment 5 we have less data (just 4 voltage values) comparing to the experiments of the previous subsection. The MFS coefficients which are linked to the source points of the outer boundary keep track of the true values (the black line) and have a very narrow credible interval, but that those linked to the inner boundary do not follows the true values and have wider credible interval.

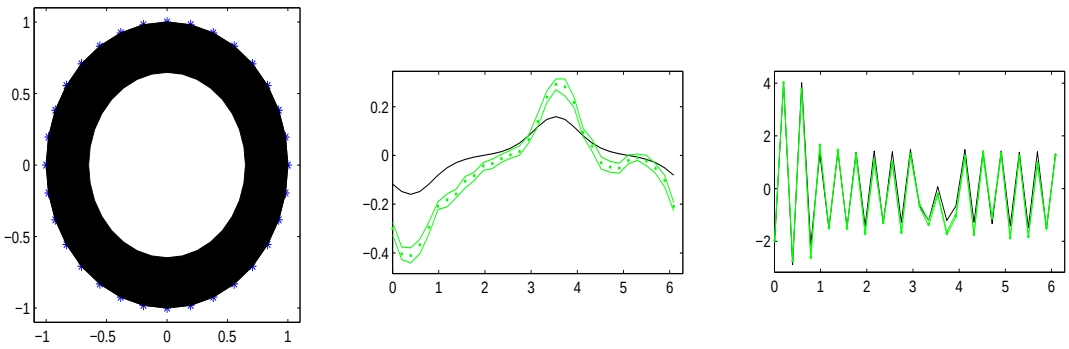

Figure 3.17: Circle model with full posterior distribution: fitted circle (left) and MFS coefficients along with credible intervals corresponding to the inner (middle) and outer boundaries (right).

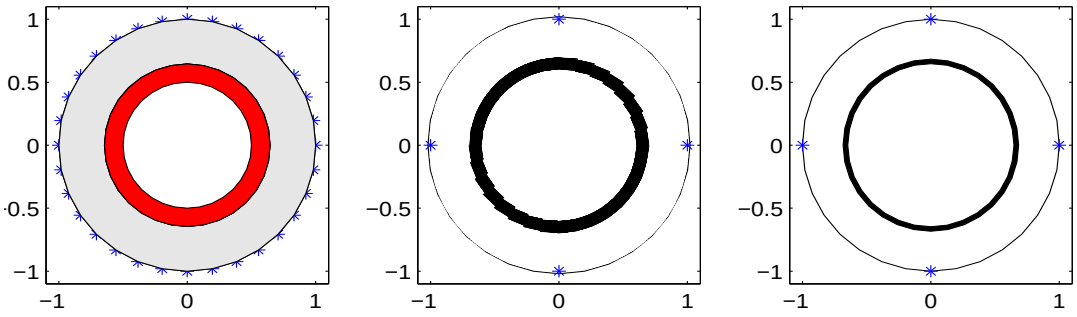

Figure 3.18: Circle model with full posterior distribution with prior parameters ($\beta_r = 1.0$, $\alpha_r = 0.1$, $\beta_{C_I} = \alpha_{C_I} = 0.0116$ and $\beta_{C_E} = \alpha_{C_E} = 0.2457$): errors estimation (left), object boundary histogram (middle) and object boundary credible interval (right).

Secondly, we solve the inverse ERT problem in Case 2. Figure 3.19 shows the fitted circle (left) and the MFS coefficients linked to the inner/outer boundary (centre/right). More precisely, the top ones are generated when using the current pattern (3.26) to calculate the first set of four voltages. Whilst, the bottom graphs are obtained when using the current pattern (3.4). All MFS coefficients are better estimated comparing to those in Case 1.

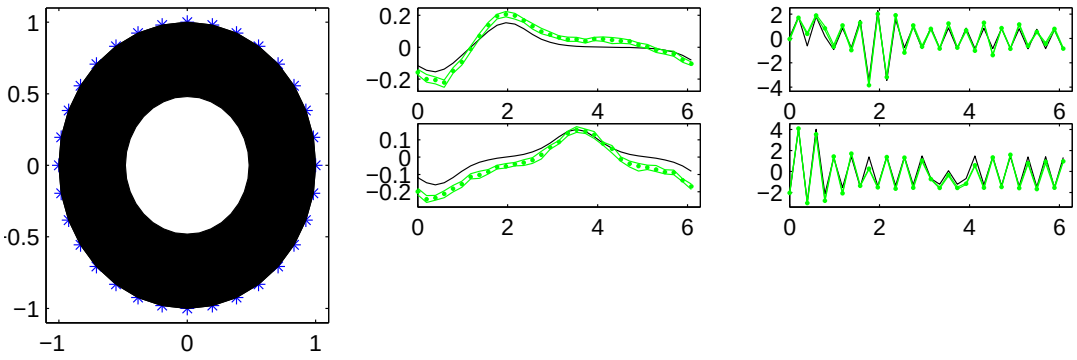

Figure 3.19: Circle model with full posterior distribution: fitted circle (left) and MFS coefficients along with credible intervals corresponding to the inner (middle) and outer (right) boundaries.

Experiment 6. Now we fit a star-shaped model using data from a circular inclusion. This uses 64 radii, $\underline{r}$ at equally-spaced angles, in addition to the unknown inner and

outer MFS coefficients, $\underline{c}$. All the hyper-prior parameters are the same as in Experiment 5.

The estimation errors of the three cases are illustrated in the left hand side of Figure 3.20, followed by the object boundary histograms and object boundary credible intervals. Then, the fitted shape and MFS coefficients (with credible intervals) corresponding to the inner and outer boundaries, respectively, in the right-hand side of the same figure. It can be seen that the smallest error is in Case 3, in comparison with the true value of 0.5, this has the largest data set with twelve voltage measurements are used. Although Cases 1 and 2 show almost the same degree of estimation error, but Case 2 provides more reliable results because the object boundary histogram and object boundary credible interval are more circular; this means better shape estimation.

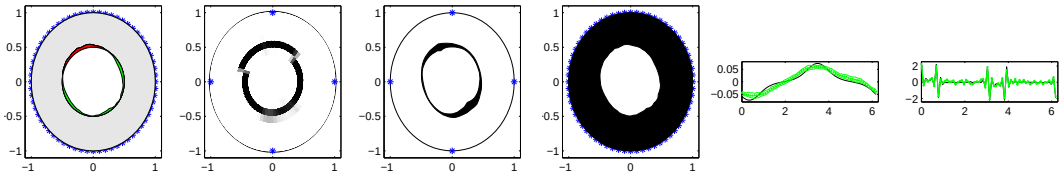

Four voltages and the estimated radius is 0.4707, with an estimated standard deviation 0.0065.

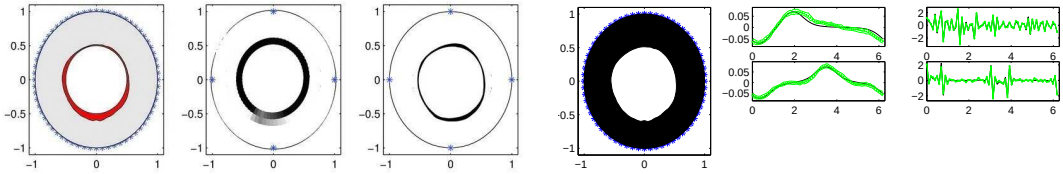

Eight voltages and the estimated radius is 0.5301, with an estimated standard deviation 0.0026.

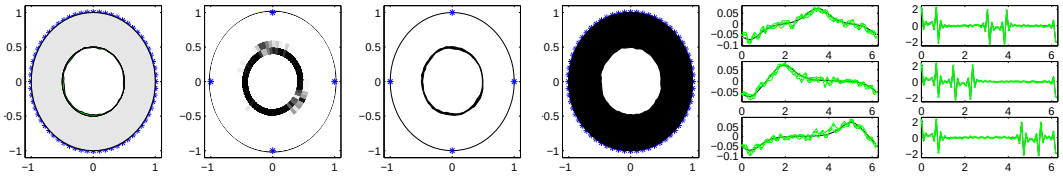

Twelve voltages and the estimated radius is 0.4909, with an estimated standard deviation 0.0027.

Figure 3.20: Star-shape model (left to right, then top to bottom): Estimation errors, object boundary histograms, object boundary credible interval, fitted shape, MFS coefficients (with credible intervals) corresponding to the inner and outer boundaries.

The True Object is an Ellipse

Experiment 7. We fit a star-shaped model using the data from an elliptical inclusion as in Case 3. All the hyper-prior parameters are the same as in Experiment 5.

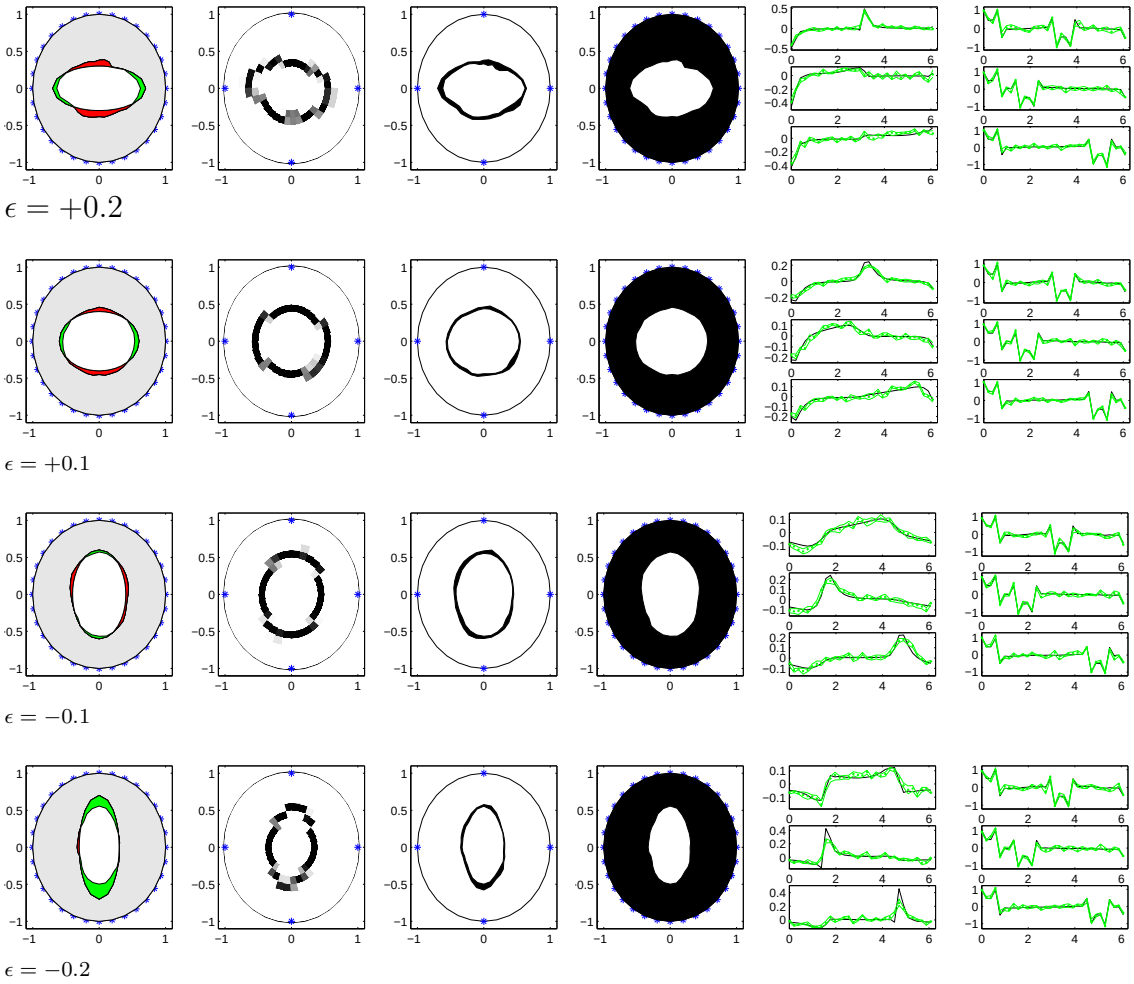

Figure 3.21: Comparison between the star-shape fitted models with different number of data voltages (left to right): estimation errors, object boundary histogram, object boundary credible interval, fitted ellipse, MFS coefficients (with credible intervals) corresponding to the inner and outer boundaries.

3.5 Extending to eight to $L = 8$ electrodes

In this section, we use a data set of $7 \times 8 = 56$ voltage measurements coming from $L = 8$ electrodes to estimate the rigid inclusion. The following seven current patterns

are used:

$$I_p = \begin{cases} 1 & \text{if } p = 1, \\ -1 & \text{if } p = 2, \\ 0 & \text{if } p \in \{3, 4, 5, 6, 7, 8\}, \end{cases} \tag{3.27}$$

$$I_p = \begin{cases} 1 & \text{if } p = 1, \\ -1 & \text{if } p = 3, \\ 0 & \text{if } p \in \{2, 4, 5, 6, 7, 8\}, \end{cases} \tag{3.28}$$

$$I_p = \begin{cases} 1 & \text{if } p = 1, \\ -1 & \text{if } p = 4, \\ 0 & \text{if } p \in \{2, 3, 5, 6, 7, 8\}, \end{cases} \tag{3.29}$$

$$I_p = \begin{cases} 1 & \text{if } p = 1, \\ -1 & \text{if } p = 5, \\ 0 & \text{if } p \in \{2, 3, 4, 6, 7, 8\}, \end{cases} \tag{3.30}$$

$$I_p = \begin{cases} 1 & \text{if } p = 1, \\ -1 & \text{if } p = 6, \\ 0 & \text{if } p \in \{2, 3, 4, 5, 7, 8\}, \end{cases} \tag{3.31}$$

$$I_p = \begin{cases} 1 & \text{if } p = 1, \\ -1 & \text{if } p = 7, \\ 0 & \text{if } p \in \{2, 3, 4, 5, 6, 8\}, \end{cases} \tag{3.32}$$

$$I_p = \begin{cases} 1 & \text{if } p = 1, \\ -1 & \text{if } p = 8, \\ 0 & \text{if } p \in \{2, 3, 4, 5, 6, 7\}. \end{cases} \tag{3.33}$$

This means that seven ERT direct problems are solved to obtain 56 voltage measurements to be used to solve the inverse ERT problem.

Figures 3.22(a) and 3.22(b) illustrate a comparison between the MFS solutions for the boundary potential $u(1, \theta)$ and the current flux $(\partial u/\partial n)(1, \theta)$, respectively, when the number of the attached electrodes is $L = 8$ using the seven current patterns (3.27)-(3.33), for the circular and horizontal elliptical inclusions. In contrast, Figures 3.23(a) and 3.23(b) represent the same quantities except that the horizontal elliptical inclusion is replaced by the vertical one.

From Figures 3.22(a) and 3.23(a), it can be seen that there is some variation in the boundary potential function values obtained from the elliptical inclusions compared to those obtained from the circular inclusion. Whilst in Figures 3.22(b) and 3.23(b) the values of boundary current flux functions for all the inclusions are almost the same.

(a)

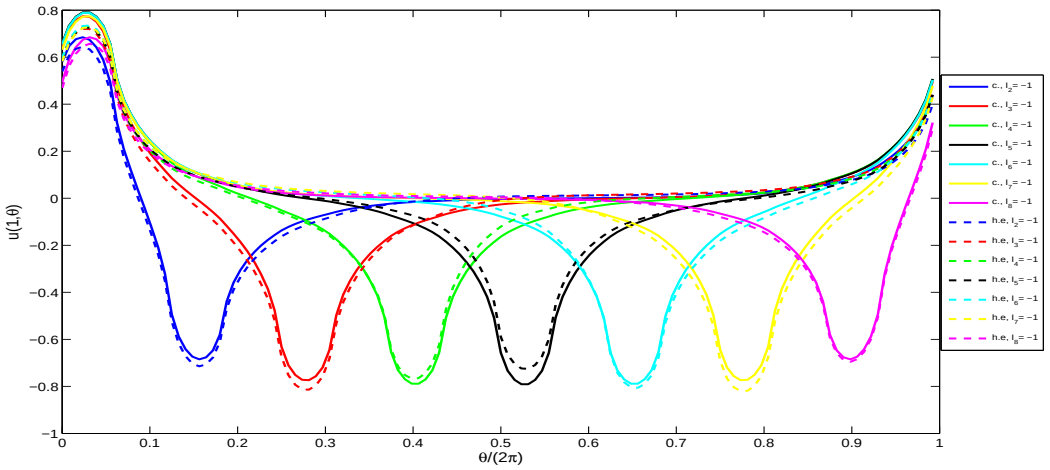

(b)

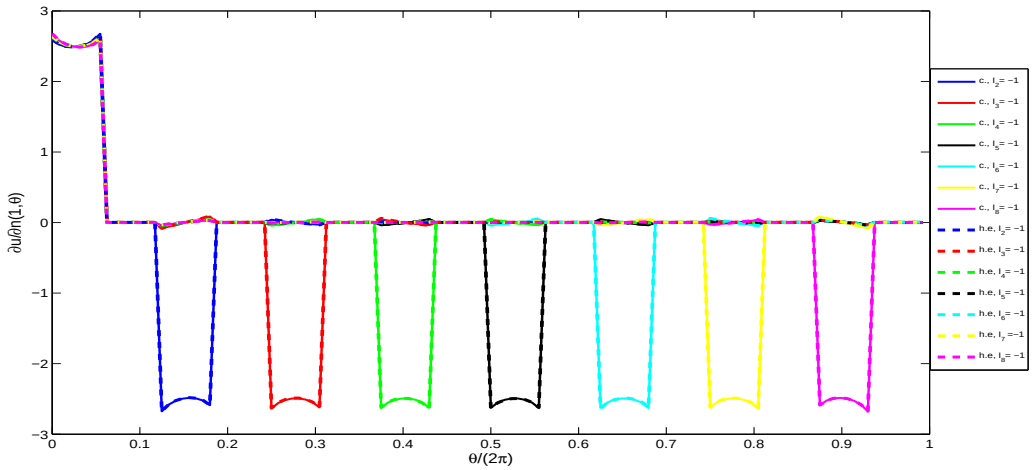

Figure 3.22: Comparison between (a) the boundary potentials $u\,(1,\theta)$ and (b) the normal derivatives $\partial u/\partial n\,(1,\theta)$, as functions of $\theta/(2\pi)$, for the current pattern (3.27) first curves on the right, and (3.28), (3.29),(3.30), (3.31), (3.32) and (3.33), subsequently. Horizontal ellipse, $\epsilon = +0.1$ (dashed lines) and circle, $\epsilon = 0$ (continuous lines).

(a)

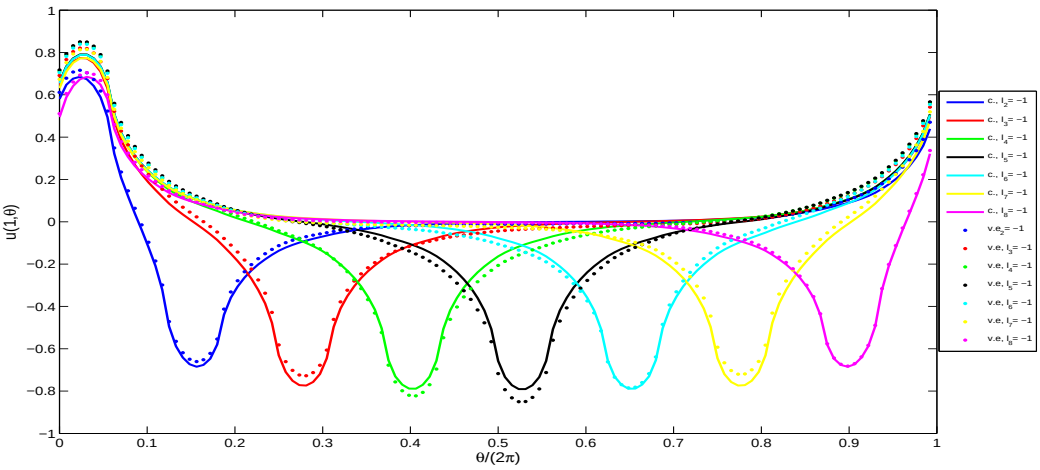

(b)

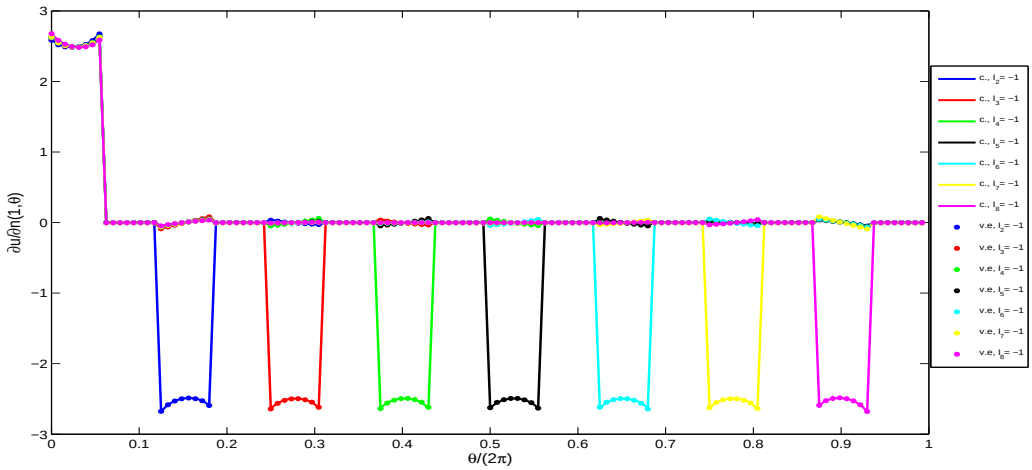

Figure 3.23: Comparison between (a) the boundary potentials $u\,(1,\theta)$ and (b) the normal derivatives $\partial u\,(1,\theta)$, as functions of $\theta/(2\pi)$, for the current pattern (3.27) first curves on the right, (3.28), (3.29),(3.30), (3.31), (3.32) and (3.33), subsequently. Vertical ellipse, $\epsilon = -0.1$ (dotted lines) and circle, $\epsilon = 0$ (continuous lines).

Experiment 8. We fit a star-shaped model to data from the circular inclusion. This includes 32 radii, $\underline{r}$ at equally-spaced angles, in addition to the unknown inner and outer MFS coefficients, $\underline{c}$. The hyper-prior parameters used here are the same as in Experiment 3 multiplied by ten.

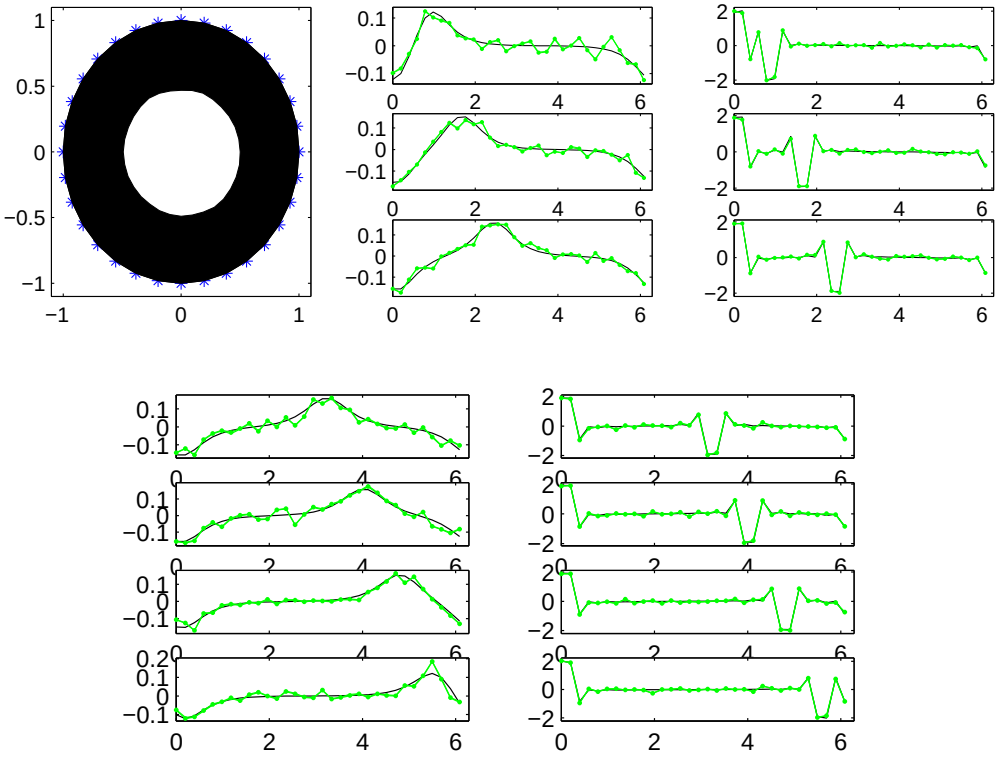

Figure 3.24: Star-shape model with full posterior distribution: fitted shape (left) and MFS coefficients along with credible intervals corresponding to the inner (middle) and outer (right) boundaries.

From Figure 3.24, it can be seen that the accuracy of the reconstruction is slightly biased with an estimated radii average of 0.4871 compared to its true value of 0.5, and a standard deviation of 0.0007. So, the accuracy has increased compared to Experiment 6. Also, both the outer and inner MFS coefficients of all seven MFS solutions follow the exact values and have very narrow credible interval. Figure 3.25 illustrates that the reconstruction of a circular inclusion is extremely good.

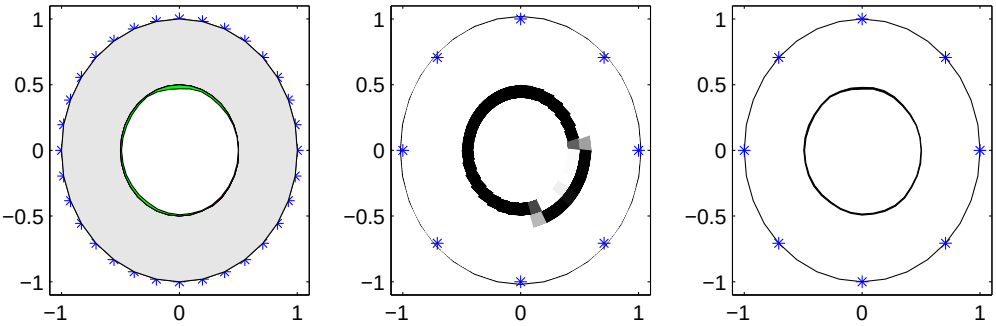

Figure 3.25: Star-shape model with full posterior distribution with prior parameters ($\alpha_r = 1.0$, $\alpha_{C_I} = 0.1160$ and $\alpha_{C_E} = 2.457$): estimation errors (left), object boundary histogram (middle) and object boundary credible interval (right).

Experiment 9. We fit a star-shaped model using data from an elliptical inclusion. The hyper-prior parameters used here are the same as in Experiment 8.

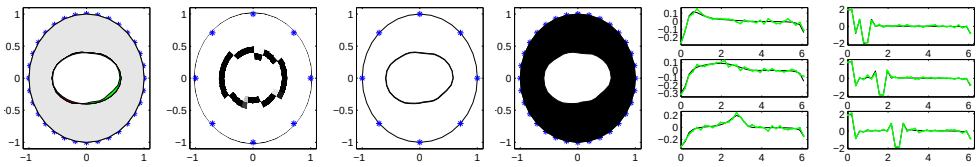

$\epsilon = +0.1$

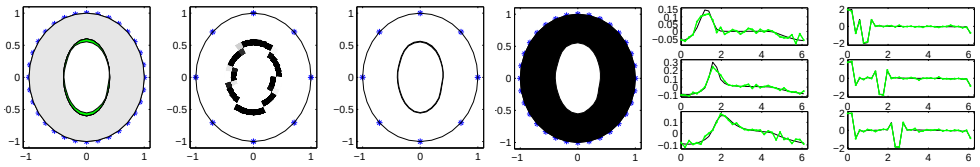

$\epsilon = -0.1$

Figure 3.26: Comparison between the fitted star-shape models with different numbers of data voltages (left to right): estimation errors, object boundary histogram, object boundary credible interval, fitted shape, MFS coefficients (with credible intervals) corresponding to the inner and outer boundaries.

From Figure 3.26, it can be seen that for $\epsilon = \pm 0.1$ the accuracy of the object reconstruction is very good because it is obvious that the estimated errors (left) are small

and the object boundary histogram, the object boundary credible interval, and the fitted ellipse for both choices of ϵ show near ellipses. Moreover, the estimated MFS coefficient values follow the true values. Here, we have only ploted those linked to the current patterns (3.27), (3.28) and (3.29) because the rest have almost the same features.

3.6 Conclusions

The Bayesian statistical approach combined with an MCMC algorithm have been used in this chapter to solve the inverse complete-electrode model problem using noisy ERT data with the forward solution obtained from the MFS. In particular, two types of noisy data sets have been considered; the first comprises boundary potential and current flux measurements while the second uses boundary voltage measurements. The shape and size of a rigid inclusions have been reconstructed in order to detect the outline of various objects.

These experiments have been gradually developed starting with simple and not very practical cases, Experiments 1, 2 and 3, where the number of attached electrodes on the outer boundary was $L = 2$, ending with very realistic cases where $L = 8$ in Experiments 8 and 9. When $L = 2$, there is only a single current pattern, whilst when $L = 8$ there are seven possible current patterns all of which are available to produce data for the estimation process. In all of the reconstruction models, the inner rigid inclusion is assumed to be a star-shaped object centred at the origin with 32 unknown radii. There are further parameters as there are 128 inner MFS coefficients and 128 outer MFS coefficients which also need estimating. For each experiment that uses the first data set, a simulated noisy data set of potential and current flux measurements was produced using 60 numerical values calculated using the MFS at 30 equally-spaced points along the region boundary.

In the experiments when $L = 2$ the accuracy of the reconstruction from the single

current pattern was surprisingly good. In other experiments, that are not shown here, when $L = 4$ but using only a single current pattern it was found that using opposing electrodes provides better estimation of the inner inclusion than was obtained from a single current pattern using adjacent electrodes. When moving to the more realistic cases and using all available current patterns, the improvement in accuracy increased further and when the number of electrodes was $L = 8$, the reconstruction results were very good. This used the maximum number of voltage measurements that is equal to $L(L-1) = 56$ as seven multiple current pattern are applied.

To conclude, this chapter demonstrates that using realistic voltage data produces excellent final reconstructions of the rigid inclusion when the maximum number of current patterns is used. Further it has been demonstrated that the combination of Bayesian statistical modelling and stochastic estimation based on the MCMC algorithm can be very successful. In particular, good reconstruction of the shape of the inclusions is possible along with simultaneous estimation of MFS coefficients. The methods have also produced measures of uncertainty in the inverse solution through Bayesian credible intervals.

Chapter 4

Estimation of the centre, contact impedance and extension to multiple rigid inclusions

4.1 Introduction

The purpose of this chapter is to solve inverse CEM problems in ERT when the centre of the inner rigid inclusion is unknown. Then, determining the different constant contact impedances (CCI) on the electrodes, as well as detecting simultaneously the unknown centre and the CCI. Lacking the exact knowledge of the CCI is a result of the electrochemical effect at the interface of electrode-skin where the properties of the skin such as the degree of the skin's thickness causes some variation in each electrode-skin interface. In a previous clinical work [45], ERT problems were solved for detecting an unknown boundary of an internal object, as well as inaccurately known measured CCI. We assume that the true values of the CCI are completely unknown and all we know is that these values must be strictly positive constants. The last part of this chapter is concerned with extending the inverse analysis to identifying multiple inner rigid inclusions, [37, 49].

4.2 The MFS forward solutions when the centre of the circular rigid inclusion is not at the origin

In this section, we describe the main modifications required when applying the MFS to solve the CEM direct problem solved in Section 2.6.2 in the unit disk $\Omega = B(\underline{0}; 1)$ which contains a rigid inclusion,

$$\Omega_{Inner} = B((X_0, Y_0); d_1) = \left\{(x, y) \in \mathbb{R}^2 | (x - X_0)^2 + (y - Y_0)^2 < d_1^2\right\}, \quad (4.1)$$

where $d_1 \in (0, 1)$, $X_0 \in (-1, 1)$ and $Y_0 \in (-1, 1)$ are chosen such that $\Omega_{Inner} \subset \Omega$. Alternatively, in polar coordinates Ω_{Inner} can be represented as

$$x = X_0 + r\cos(\theta), \quad y = Y_0 + r\cos(\theta), \quad r \in (0, d_1), \quad \theta \in [0, 2\pi). \quad (4.2)$$

The geometrical condition that $\Omega_{Inner} \subset \Omega$ recasts as

$$\begin{aligned} 1 &> (X_0 + r\cos(\theta))^2 + (Y_0 + r\sin(\theta))^2 \\ &= X_0^2 + Y_0^2 + r^2 + 2r\left(X_0\cos(\theta) + Y_0\sin(\theta)\right), \ r \in (0, d_1), \ \theta \in [0, 2\pi) \end{aligned} \quad (4.3)$$

The coordinates of the internal boundary collocation points are
$\underline{x}_i = \left(X_0 + d_1\cos\left(\frac{2\pi(i-M)}{M}\right), Y_0 + d_1\sin\left(\frac{2\pi(i-M)}{M}\right)\right)$ for $i = \overline{M+1, 2M}$,
and the internal source points are
$\underline{\xi}_j = (\xi_j^1, \xi_j^2) = \left(X_0 + R_1\cos\left(\frac{2\pi(j-N)}{N}\right), Y_0 + R_1\sin\left(\frac{2\pi(j-N)}{N}\right)\right)$ for $j = \overline{N+1, 2N}$,
where $0 < R_1 < d_1$. Also, as previously, R_1 is defined as $R_1 = d_1 \times \eta_I$, where $\eta_I \in (0, 1)$ is a contraction parameter.

4.2.1 Numerical results and discussion

In this subsection, we show some comparisons between the MFS direct solutions for the boundary potential, current flux and the voltages in cases where the centre of the circular rigid inclusion is changed from the origin to $(0.1, 0.1)$.

For illustrative purposes, let us take $d_1 = 0.5$, $M = N = 128$, $R = 1.15$, $R_1 = 0.45$ and $L = 4$ with CCI values equal to $z_{\{1,2,3,4\}} = 1$, and consider the three current patterns (3.26), (3.4) and (3.3) in this order from the previous chapter.

Figures 4.1(a) and 4.1(b) show comparisons between the MFS forward solutions for the boundary potential $u(1, \theta)$ and the current flux $(\partial u/\partial n)(1, \theta)$, respectively, when the centre of the inner circular object is $(0, 0)$ and $(0.1, 0.1)$. From Figure 4.1(a), it can be seen that there are obvious variations in the boundary potential when changing the centre of the inner object from the origin to $(X_0, Y_0) = (0.1, 0.1)$. More precisely, the greatest variations can be seen on the third attached electrode because the equipotential lines cover that part of the domain much more when the current pattern (3.3) is applied. Whilst, in Figure 4.1(b), the values of current flux are almost the same all around the unit disk.

(a)

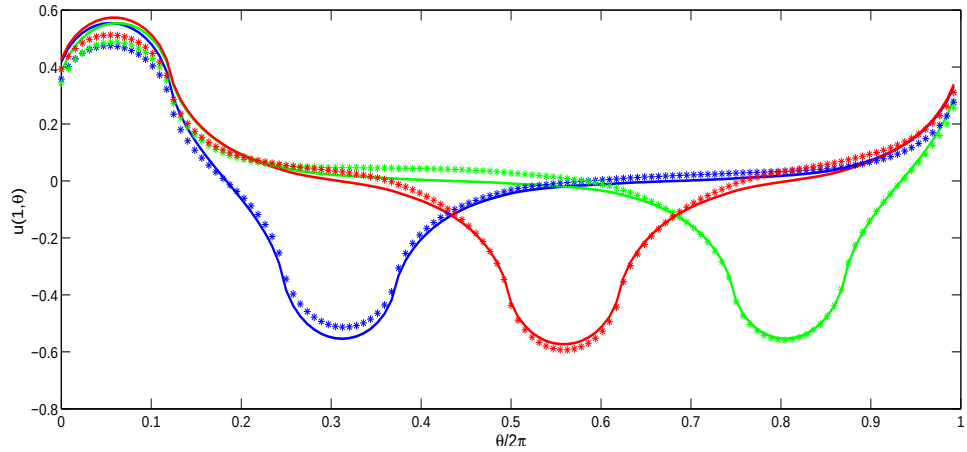

(b)

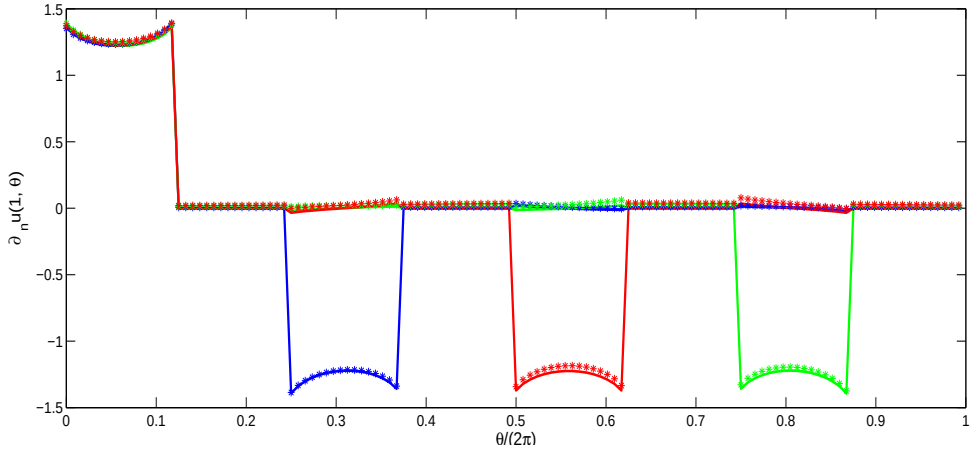

Figure 4.1: (a) The boundary potential $u(1,\theta)$ and (b) the normal derivative $\partial_n u(1,\theta)$ when the centre of the inner circle is at $(0,0)$ (continuous line) and $(0.1,0.1)$ (points), as a functions of $\theta/(2\pi)$, for the current patterns (3.26) (blue), (3.4) (red) and (3.3) (green).

Since there is not much sensitivity in the potential and especially the current flux when the centre of the inner circular object is changed from $(0,0)$ to $(0.1,0.1)$, it is worth investigating the differences in the calculated boundary voltages U_p^i, on the attached electrodes ε_p, $p=\overline{1,4}$, $i=\overline{1,3}$, for the current patterns (3.26) ($i=1$), (3.4) ($i=2$) and (3.3) ($i=3$), see Table 4.1. From Table 4.1, it can be seen that the values for the voltages $\{U_3^1, U_4^1, U_2^2, U_4^2, U_2^3, U_3^3\}$ are close to zero whatever the chosen

centre, especially the values $\{U_2^2, U_4^2\}$ where the best current pattern (3.4) is injected through opposite electrodes. This is because the currents are not injected through the corresponding attached electrodes. However, there are noticeable differences in all the voltages when the centre is varied.

Table 4.1: The numerical voltages when the center of the inner rigid inclusion is at $(0, 0)$ in comparison with the resulting voltages when the centre is at $(0.1, 0.1)$, for the current patterns (3.26), (3.4) and (3.3).

Current pattern (3.26)		
Voltages	Centre $(0, 0)$	Centre $(0.1, 0.1)$
$U_1^1 \approx$	1.7759	1.7101
$U_2^1 \approx$	-1.7759	-1.7294
$U_3^1 \approx$	-0.0221	-0.0069
$U_4^1 \approx$	0.0221	0.0032
Current pattern (3.4)		
Voltages	Centre $(0, 0)$	Centre $(0.1, 0.1)$
$U_1^2 \approx$	1.7980	1.7638
$U_2^2 \approx$	1.8×10^{-10}	0.0086
$U_3^2 \approx$	-1.7980	-1.7785
$U_4^2 \approx$	5.5×10^{-10}	0.0073
Current pattern (3.3)		
Voltages	Centre $(0, 0)$	Centre $(0.1, 0.1)$
$U_1^3 \approx$	1.7759	1.7318
$U_2^3 \approx$	0.0221	0.0358
$U_3^3 \approx$	-0.0221	-0.0252
$U_4^3 \approx$	-1.7759	-1.7535

4.3 The inverse solution when the centre of the inner rigid inclusion is unknown

In this section, we will identify the inner object Ω_{Inner} in the domain Ω when the centre (X_0, Y_0) of that object, as well as the MFS coefficients $\underline{c} = (c_k)_{k=\overline{1,2M}}$ and the radii $\underline{r} = (r_i)_{i=\overline{1,M}}$ of the assumed star-shaped object are all unknown. Moreover, the data

sets which are simulated here are the voltages on the electrodes for various current patterns. This data set is obtained from the Robin boundary condition after solving the CEM direct problem using the MFS. Further, these voltages are corrupted by adding Gaussian noise with zero mean and standard deviation $\sigma = 0.01$. In all experiments in this chapter, we consider the following cases:

Case 1: The injected current patterns are given by equations (3.26), (3.4) and (3.3). This is convenient when the number of the attached electrodes on the outer boundary is $L = 4$. Basically, the voltages are calculated at 4 equally-spaced points on the outer boundary, that is at the locations where the four electrodes are attached. These four voltage values are obtained each time a current pattern is applied. This results in three sets of voltages giving a total of 12 single voltage values, namely,

$$\{U_1^1, U_2^1, U_3^1, U_4^1\},$$

when the first current pattern (3.26) is applied,

$$\{U_1^2, U_2^2, U_3^2, U_4^2\},$$

when the second current pattern (3.4) is applied, and

$$\{U_1^3, U_3^3, U_3^3, U_4^3\},$$

when the third current pattern (3.3) is applied.

Case 2: The injected current patterns are given by equations (3.27)-(3.33) where the number of the attached electrodes is $L = 8$. This results in seven sets containing a total of 56 voltage values to be used to produce the inverse solution, namely:

$$\{U_1^1, U_2^1, U_3^1, U_4^1, U_5^1, U_6^1, U_7^1, U_8^1\},$$

when we apply the current pattern (3.27),

$$\{U_1^2, U_2^2, U_3^2, U_4^2, U_5^2, U_6^2, U_7^2, U_8^2\},$$

when we apply the current pattern (3.28),

$$\{U_1^3, U_3^3, U_3^3, U_4^3, U_5^3, U_6^3, U_7^3, U_8^3\},$$

when we apply the current pattern (3.29),

$$\{U_1^4, U_2^4, U_3^4, U_4^4, U_5^4, U_6^4, U_7^4, U_8^4\},$$

when we apply the current pattern (3.30),

$$\{U_1^5, U_2^5, U_3^5, U_4^5, U_5^5, U_6^5, U_7^5, U_8^5\},$$

when we apply the current pattern (3.31),

$$\{U_1^6, U_2^6, U_3^6, U_4^6, U_5^6, U_6^6, U_7^6, U_8^6\},$$

when we apply the current pattern (3.32), and

$$\{U_1^7, U_2^7, U_3^7, U_4^7, U_5^7, U_6^7, U_7^7, U_8^7\},$$

when we apply the current pattern (3.33).

Experiment 1. We examine Cases 1 and 2 by fitting a star-shaped model to data from a true circular object of radius 0.5 centred at $(0.1, 0.1)$. In both cases, the unknowns are 32 radii at equally-spaced angles $\underline{r} = (r_i, i = \overline{1, 32})$, in addition to the 128 inner MFS coefficients, $\underline{c}_I$, and the 128 outer MFS coefficients, $\underline{c}_E$, as well as the unknown centre denoted by (X_0, Y_0).

Assuming the centre of the inner object is unknown means the additional constraint (4.3) is required in the MCMC to ensure that the star-shaped object stays within the unit circle.

The hierarchical structure of the statistical parameter model on the right side of Figure 3.5 is considered here. Moreover, we fix the values of the hyper-prior parameters (from Experiments 8 and 9 in Chapter 3) of the internal and external MFS coefficients at $\alpha_{C_I} = 0.1160$ and $\alpha_{C_E} = 2.4570$, respectively, as well as the hyper-prior parameter value for the radius at $\alpha_r = 1.0$, and allow estimation of the smoothing parameters β_{C_I}, β_{C_E} and β_r, as well as all the unknowns which have been mentioned earlier.

Figure 4.2 shows a comparison between the reconstruction of the inner object in Cases 1 and 2. From this figure, it can be seen that the accuracy of the reconstruction is very good when $L = 8$, with the estimated radius of 0.4915 compared to its true value of 0.5, and a very small standard deviation of 0.0009. Moreover, the estimated centre is $(0.0906, 0.0989)$ in comparison to the true centre $(0.1000, 0.1000)$. However, when $L = 4$ the estimated radius is 0.5593 with standard deviation 0.0004 and the estimated centre is at $(0.1054, 0.1003)$. Both sets of outer and inner MFS coefficients in Cases 1 and 2 keep follow the exact values and have smooth and very narrow credible intervals. In the left side of Figure 4.2 the estimated errors, which are defined as the difference between the true and estimated radii, can hardly be seen on the graph. Furthermore, the object boundary histograms are circular with respect to the estimated centre.

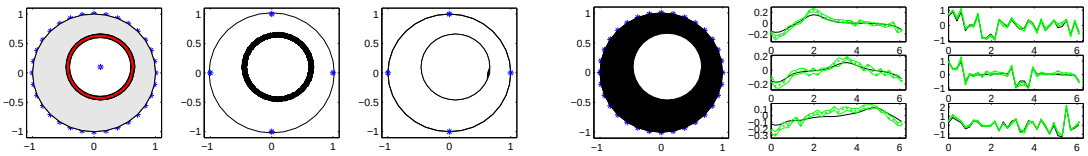

Case 1. The number of the attached electrodes is $L = 4$ and the number of the measured voltages is 12.

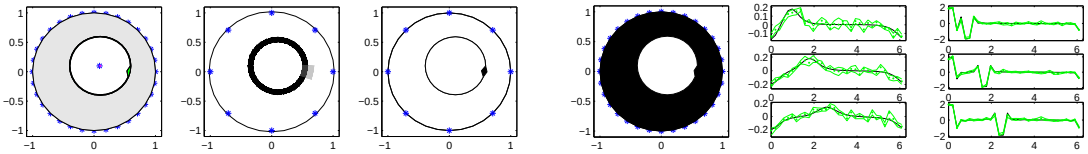

Case 2. The number of the attached electrodes is $L = 8$ and the number of the measured voltages is 56.

Figure 4.2: Results from the star-shaped model with different numbers of data voltages: errors estimation (left), object boundary histogram, object boundary credible intervals, fitted circle, MFS coefficients (with credible intervals) corresponding to the inner and outer boundaries (right).

4.4 The MFS forward solutions when the constant contact impedance is changed to piecewise constant

In this section, we study how the MFS forward solutions, in terms of the boundary potential, current flux and the voltages, are affected by a change in the constant contact impedance (CCI).

4.4.1 Numerical results and discussion

For illustrative purposes, let us consider the centre of the inner circle being at the origin, take $M = N = 128$, $R = 1.15$, $R_1 = 0.45$ and $L = 4$, and apply the current patterns

(3.26), (3.4) and (3.3). We investigate two different sets the CCI values, namely,

$$z_p^{(1)} = 1, \quad p = \overline{1,4} \quad \text{on } \partial\Omega, \tag{4.4}$$

and

$$z_p^{(2)} = 1, \quad p = \overline{1,2}, \quad z_p^{(2)} = 2, \quad p = \overline{3,4} \quad \text{on } \partial\Omega. \tag{4.5}$$

Table 4.2 shows the three calculated sets of voltages. From this table, it can be seen that injecting the current pattern (3.26) makes the voltage values, using both equations (4.4) and (4.5), almost the same due to two reasons. Firstly, the voltages which are calculated at electrodes $\varepsilon_{1,2}$ which carry current, have the same values because the values of the CCI are still the same in both equations (4.4) and (4.5), $z_1^1 = z_1^2 = z_2^1 = z_2^2 = 1$. Furthermore, voltages which are calculated at the free-current electrodes, $\varepsilon_{3,4}$, nearly vanish for any positive value of the CCI. In contrast, the major differences between the voltage values occurring when equations (3.4) and (3.3) are used. More precisely, the voltage value U_3^2 drops from -1.7980 to -3.0723 due to the dramatic increase in the corresponding value of the CCI from $z_3^1 = 1$ to $z_3^2 = 2$, as well as the voltage value U_4^3 decreases from -1.7759 to -3.0502 due to the same change of the CCI values from $z_4^1 = 1$ to $z_4^2 = 2$.

Table 4.2: The numerical voltages for the CCI values (4.4) and (4.5), when the center of the inner circular rigid inclusion is at $(0, 0)$, for the current patterns (3.26), (3.4) and (3.3).

Current pattern (3.26)		
Voltages	$z_{1,2,3,4} = 1$	$z_{1,2} = 1$ and $z_{3,4} = 2$
$U_1^1 \approx$	1.7759	1.7760
$U_2^1 \approx$	-1.7759	-1.7760
$U_3^1 \approx$	-0.0221	-0.0221
$U_4^1 \approx$	0.0221	0.0221
Current pattern (3.4)		
Voltages	$z_{1,2,3,4} = 1$	$z_{1,2} = 1$ and $z_{3,4} = 2$
$U_1^2 \approx$	1.7980	1.7981
$U_2^2 \approx$	1.8×10^{-10}	4.6×10^{-5}
$U_3^2 \approx$	-1.7980	-3.0723
$U_4^2 \approx$	5.5×10^{-10}	4.6×10^{-5}
Current pattern (3.3)		
Voltages	$z_{1,2,3,4} = 1$	$z_{1,2} = 1$ and $z_{3,4} = 2$
$U_1^3 \approx$	1.7759	1.7760
$U_2^3 \approx$	0.0221	0.0222
$U_3^3 \approx$	-0.0221	-0.0221
$U_4^3 \approx$	-1.7759	-3.0502

4.5 The inverse solutions when the CCI values are unknown

We consider Case 2 of Section 4.4, where both the centre of the inner rigid inclusion, as well as the positive constant contact impedance (CCI) values $\{z_{1,2,3,4,5,6,7,8}\}$ are unknown. In the following experiment, $L = 8$ and we simulate 56 measured voltages which are also corrupted by adding Gaussian noise with zero mean and standard deviation $\sigma = 0.01$.

Experiment 2. We fit a star-shaped model from the circular data of radius 0.5 centred at $(0.1, 0.1)$, and the true values of the CCI are $z_{1,2,3,4} = 1$ and $z_{5,6,7,8} = 2$. We fix the values of the hyper-prior parameters at the same values which were considered in

Experiment 1.

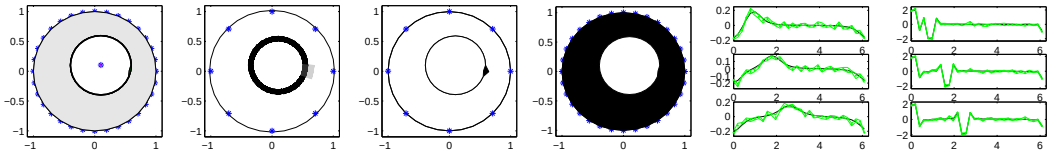

Figure 4.3: The star-shaped model when the CCI values and the centre of the inner object are unknown: errors estimation (left), object boundary histogram, object boundary credible intervals, fitted circle, MFS coefficients (with credible intervals) corresponding to the inner and outer boundaries (right).

From Figure 4.3, it can be seen that the accuracy of the reconstruction is very good, with the estimated radius of 0.4915 compared to its true value of 0.5, and a very small standard deviation of 0.0005. Moreover, the estimated centre is $(0.1013, 0.1040)$ in comparison to the true centre $(0.1000, 0.1000)$. Moreover, from Table 4.3 and Figure 4.4, it can be seen, in general, that the values of CCI are well estimated comparing to the true values, especially $\{z_1, z_3, z_4, z_6, z_7, z_8\}$ where the standard deviations are relatively small.

Table 4.3: The average mean of the estimated contact impedances over the MCMC iterations with the corresponding standard deviations.

	True value	Estimated value	Standard deviation
z_1	1	1.0671	0.0369
z_2	1	1.1583	0.1313
z_3	1	0.9637	0.0419
z_4	1	0.9156	0.0697
z_5	2	1.9036	0.1537
z_6	2	1.9641	0.0528
z_7	2	2.0660	0.0530
z_8	2	2.0333	0.0607

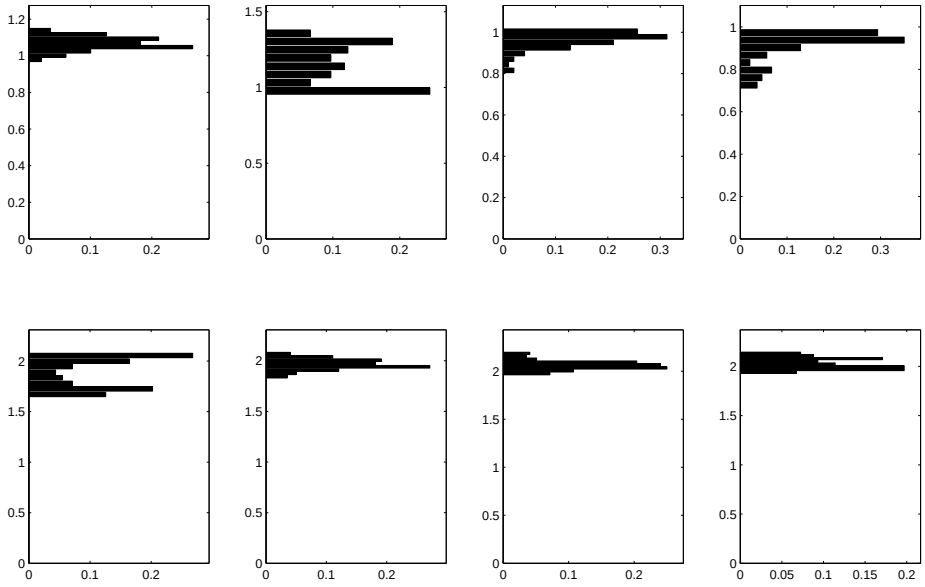

Figure 4.4: Histograms of the estimated contact impedances.

4.6 The MFS forward solution for multiple rigid inclusions

In this section, we illustrate the main modifications which are required when the MFS is applied to solve the CEM direct problem in the unit disk, containing two rigid inclusions,

$$\begin{aligned}\Omega_{Inner_1} &= B_1\left((X_0, Y_0); d_1\right) \\ &= \left\{(x_0, y_0) \in \mathbb{R}^2 | (x_0 - X_0)^2 + (y_0 - Y_0)^2 < d_1^2\right\}, \end{aligned} \tag{4.6}$$

$$\begin{aligned}\Omega_{Inner_2} &= B_2\left((X_1, Y_1); d_2\right) \\ &= \left\{(x_1, y_1) \in \mathbb{R}^2 | (x_1 - X_1)^2 + (y_1 - Y_1)^2 < d_2^2\right\}, \end{aligned} \tag{4.7}$$

where $\{d_1, d_2\} \in (0,1)$, $\{X_0, X_1\} \in (-1,1)$ and $\{Y_0, Y_1\} \in (-1,1)$ are chosen such that $\Omega_{Inner_1}, \Omega_{Inner_2} \subset \Omega$.

Alternatively, in polar coordinates Ω_{Inner_1} and Ω_{Inner_2} can be represented, respectively, as

$$x_0 = X_0 + r_1\cos(\theta), \quad y_0 = Y_0 + r_1\cos(\theta), \quad r_1 \in (0, d_1), \quad \theta \in [0, 2\pi), \tag{4.8}$$

and

$$x_1 = X_1 + r_2\cos(\theta), \quad y_1 = Y_1 + r_2\cos(\theta), \quad r_2 \in (0, d_2), \quad \theta \in [0, 2\pi). \tag{4.9}$$

The geometrical conditions that $\Omega_{Inner_1}, \Omega_{Inner_2} \subset \Omega$ can be recast as

$$\begin{aligned} 1 &> (X_0 + r_1\cos(\theta))^2 + (Y_0 + r_1\sin(\theta))^2 \\ &= X_0^2 + Y_0^2 + r_1^2 + 2r_1\left(X_0\cos(\theta) + Y_0\sin(\theta)\right), \\ &\qquad r_1 \in (0, d_1), \theta \in [0, 2\pi) \end{aligned} \tag{4.10}$$

and

$$\begin{aligned} 1 &> (X_1 + r_2\cos(\theta))^2 + (Y_1 + r_2\sin(\theta))^2 \\ &= X_1^2 + Y_1^2 + r_2^2 + 2r_2\left(X_1\cos(\theta) + Y_1\sin(\theta)\right), \\ &\qquad r_2 \in (0, d_2), \theta \in [0, 2\pi) \end{aligned} \tag{4.11}$$

and they must not intersect.

The coordinates of the boundary collocation points on $\partial\Omega_{Inner_1}$ are
$\underline{x}_i = \left(X_0 + d_1\cos\left(\frac{2\pi(i-M)}{M}\right), Y_0 + d_1\sin\left(\frac{2\pi(i-M)}{M}\right)\right)$ for $i = \overline{M+1, 2M}$,
and the coordinates of the boundary collocation points $\partial\Omega_{Inner_2}$ are
$\underline{x}_i = \left(X_1 + d_2\cos\left(\frac{2\pi(i-2M)}{M}\right), Y_1 + d_2\sin\left(\frac{2\pi(i-2M)}{M}\right)\right)$ for $i = \overline{2M+1, 3M}$.
Also, the internal source points in Ω_{Inner_1} and Ω_{Inner_2} are
$\underline{\xi}_j = (\xi_j^1, \xi_j^2) = (X_0 + R_1\cos\left(\frac{2\pi(j-N)}{N}\right), Y_0 + R_1\sin\left(\frac{2\pi(j-N)}{N}\right))$ for $j = \overline{N+1, 2N}$,

and

$\underline{\xi}_j = (\xi_j^1, \xi_j^2) = (X_1 + R_2 \cos\left(\frac{2\pi(j-2N)}{N}\right), Y_1 + R_2 \sin\left(\frac{2\pi(j-2N)}{N}\right))$ for $j = \overline{2N+1, 3N}$, where $0 < R_1 < d_1$ and $0 < R_2 < d_2$. Also, R_1 and R_2 are defined previously as $R_1 = d_1 \times \eta_{I_1}$ and $R_2 = d_2 \times \eta_{I_2}$, where $\eta_{I_1}, \eta_{I_2} \in (0, 1)$ are contraction parameters.

4.6.1 Numerical results and discussion

In this subsection, we show some comparisons between the MFS direct solutions for the boundary potential, current flux and the voltages, in the case where the number of rigid inclusions is extended to two circles being centered at $C_1(0, 0.5)$ and $C_2(0, -0.5)$. For illustrative purposes, we take $M = N = 128$, $R = 1.15$, $R_1 = R_2 = 0.45$, $d_1 = d_2 = 0.4$ and $L = 8$, and apply the current patterns (3.27)-(3.33).

Figures 4.5(a) and 4.5(b) show comparisons between the MFS forward solutions for the boundary potential $u(1, \theta)$ and the current flux $(\partial u/\partial n)(1, \theta)$, when the unit disc has one inclusion $B_1\left((0, 0.5), 0.4\right)$ comparing to when it has two inclusions $B_1\left(C_1, 0.4\right)$ and $B_2\left(C_2, 0.4\right)$. In general, it can be seen from these figures that the boundary potential and the current flux follow the same pattern. Due to the properties of equipotential lines and the current flow, it can be seen that when the current patterns (3.27)-(3.29) are applied, the top-half of the unit disc is being scanned. As a result, the values of the boundary potential and current flux are almost the same whether we have one or two inclusions. However, using the other current patterns has significant impact on the potential and current flux values. More precisely, the biggest difference in the potential values in Figure 4.5(a) or in the current flux values in Figure 4.5(b), can be seen when equation (3.32) is used, followed by when equation (3.31) is applied, due to the position of the second inclusion, $B_2\left(C_2, 0.4\right)$. Then, a smaller difference can be seen when current pattern in equation (3.33) is employed, followed by a gradually decreasing difference obtained from applying the current patterns (3.30), (3.29), (3.28) and (3.27), respectively.

(a)

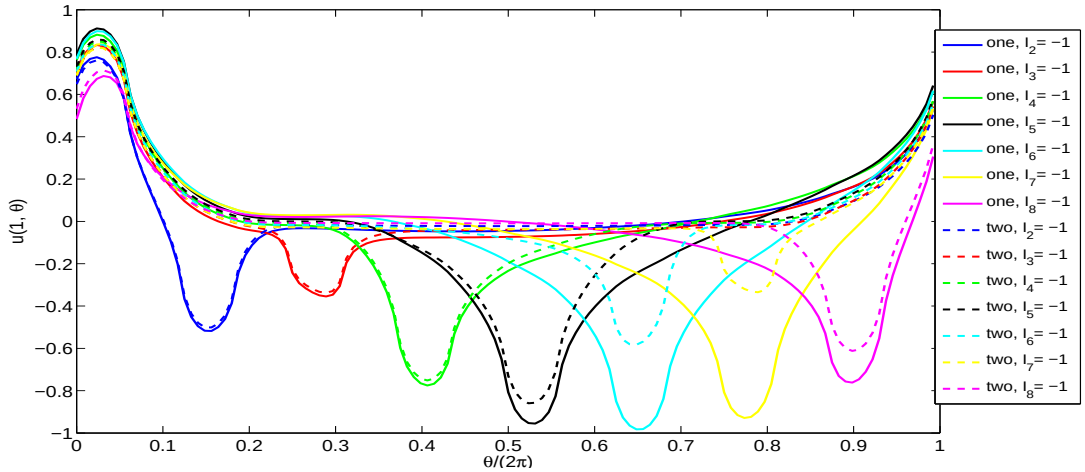

(b)

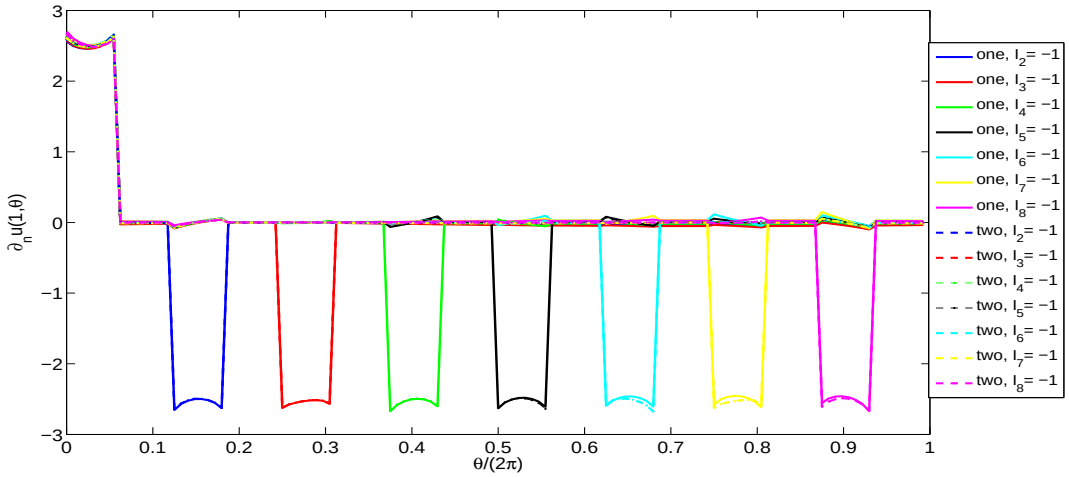

Figure 4.5: (a) The boundary potential $u\,(1,\theta)$ and (b) the normal derivative $\partial u_n\,(1,\theta)$, as functions of $\theta/(2\pi)$, for the current pattern (3.27) first curves on the right, (3.28), (3.29), (3.30), (3.31), (3.32) and (3.33), subsequently. Two rigid inclusions, (dashed lines) and one rigid inclusion, (continuous lines).

Table 4.4: The numerical voltages when the center of the inner rigid inclusion is at $(0, 0.5)$, in comparison to when the centres of two rigid inclusions are at $(0, 0.5)$ and (0,-0.5), for the current patterns (3.27)-(3.33).

Using Equation (3.27)		
The voltages	One inclusion	Two inclusions
$U_1^1 \approx$	3.2366	3.2396
$U_2^1 \approx$	-3.0174	-2.9964
Using Equation (3.28)		
The voltages	One inclusion	Two inclusions
$U_1^2 \approx$	3.2902	3.3010
$U_3^2 \approx$	-2.8683	-2.8503
Using Equation (3.29)		
The voltages	One inclusion	Two inclusions
$U_1^3 \approx$	3.3588	3.3381
$U_4^3 \approx$	-3.2724	-3.2429
Using Equation (3.30)		
The voltages	One inclusion	Two inclusions
$U_1^4 \approx$	3.4102	3.3506
$U_5^4 \approx$	-3.4371	-3.3506
Using Equation (3.31)		
The voltages	One inclusion	Two inclusions
$U_1^5 \approx$	3.4096	3.3205
$U_6^5 \approx$	-3.4454	-3.0773
Using Equation (3.32)		
The voltages	One inclusion	Two inclusions
$U_1^6 \approx$	3.3507	3.2990
$U_7^6 \approx$	-3.3843	-2.8483
Using Equation (3.33)		
The voltages	One inclusion	Two inclusions
$U_1^7 \approx$	3.1855	3.1961
$U_8^7 \approx$	-3.2217	-3.1009

In Table 4.4, there is no need to report the values of voltages $\{U_3^1, U_4^1, U_5^1, U_6^1, U_7^1, U_8^1\}$, $\{U_2^2, U_4^2, U_5^2, U_6^2, U_7^2, U_8^2\}$, $\{U_2^3, U_3^3, U_5^3, U_6^3, U_7^3, U_8^3\}$, $\{U_2^4, U_3^4, U_4^4, U_6^4, U_7^4, U_8^4\}$, $\{U_2^5, U_3^5, U_4^5, U_5^5, U_7^5, U_8^5\}$, $\{U_2^6, U_3^6, U_4^6, U_5^6, U_6^6, U_8^6\}$ and $\{U_2^7, U_3^7, U_4^7, U_5^7, U_6^7, U_7^8\}$, since their values are almost zero. This is because these voltage values are located at points where a free-current electrodes have been attached.

It can be seen from Table 4.4 that although there are not many differences in the values of the voltages on the electrodes $\varepsilon_{1,2,3,4,5,8}$ when two inner rigid inclusions are compared to the corresponding voltage values obtained using only one rigid inclusion in the unit disk, differences in the compared voltages on the attached electrodes $\varepsilon_{6,7}$ are noticeable. This is due to the effect of the second rigid inclusion centred at $(0, -0.5)$ on the equipotential lines when the current patterns (3.31) and (3.32) are applied.

4.7 The inverse solutions for two rigid inclusions

In this section, we consider Case 2 of Section 4.4 where the centres of two inner rigid inclusions are unknown, (X_0, Y_0) and (X_1, Y_1). In the following experiment, $L = 8$ and we simulate 56 measured voltage which are also corrupted by adding Gaussian noise with zero mean and standard deviation $\sigma = 0.01$.

Further modifications in the inverse mathematical formulation when extending the number of the inclusions to two are considered. Assuming the centres of the objects are unknown means an additional condition is required in the MCMC to ensure that the star-shaped objects do not intersect. So, the distance between the centres (X_0, Y_0) and (X_1, Y_1) should be greater than the sum of the diameters. As a result,

$$S = \sqrt{(X_0 - X_1)^2 + (Y_0 - Y_1)^2} > \text{diam}(\Omega_{Inner_1}) + \text{diam}(\Omega_{Inner_2}), \tag{4.12}$$

where the diameters of Ω_{Inner_1} and Ω_{Inner_2} are defined as

$$\text{diam}(\Omega_{Inner_1}) = \max_{\underline{x},\underline{y} \in \partial\Omega_{Inner_1}} |\underline{x} - \underline{y}|, \tag{4.13}$$

and

$$\text{diam}(\Omega_{Inner_2}) = \max_{\underline{x},\underline{y}\in\partial\Omega_{Inner_2}} |\underline{x}-\underline{y}|, \tag{4.14}$$

respectively. Alternatively, in polar coordinates $\text{diam}(\Omega_{Inner_1})$ can be represented as

$$\text{diam}(\Omega_{Inner_1}) = \max_{\theta,\phi\in[0,2\pi)} \sqrt{r_1^2(\theta)+r_1^2(\phi)-2r_1(\theta)r_1(\phi)\cos(\theta-\phi)} \tag{4.15}$$

and similarly for $\text{diam}(\Omega_{Inner_2})$.

Experiment 3. We fit a star-shaped model to true circular data when the centres of those objects are at $(0, 0.5)$ and $(0, -0.5)$ with true radii equal to 0.4. Fitting star-shaped models includes finding an estimated values for 32 radii, $\underline{r}_1$ for the first inclusion, and 32 radii, $\underline{r}_2$ for the second inclusion, the MFS coefficients, $(\underline{c}_k)_{k=\overline{1,3M}}$ consisting of 128 outer MFS coefficients corresponding to $\partial\Omega_{Outer}$, 128 inner MFS coefficients corresponding to Ω_{Inner_1} and 128 inner MFS coefficients corresponding to Ω_{Inner_2}, in addition to the unknown centres (X_0, Y_0) and (X_1, Y_1).

Again, we emphasize that the condition (4.12) should be imposed in the MCMC reconstruction code. The diameters of Ω_{Inner_1} and Ω_{Inner_2} can be simplified as

$$\text{diam}(\Omega_{Inner_1}) = \max_{i,j=\overline{1,32}} \sqrt{r_{1i}^2+r_{1j}^2-2r_{1i}r_{1j}\cos(\theta_i-\theta_j)}, \tag{4.16}$$

and

$$\text{diam}(\Omega_{Inner_2}) = \max_{i,j=\overline{1,32}} \sqrt{r_{2i}^2+r_{2j}^2-2r_{2i}r_{2j}\cos(\theta_i-\theta_j)}. \tag{4.17}$$

We fix the values of the hyper-prior parameters at the same values which were considered in Experiments 1 and 2.

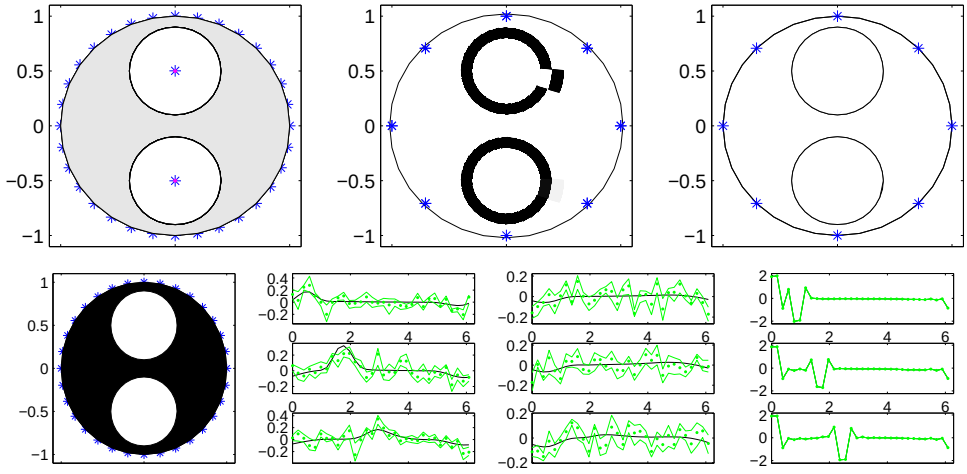

Figure 4.6: The star-shape models for two inclusions when the centres of the inner objects are unknown, from left to right and continued on the second row: errors estimation, object boundary histogram, object boundary credible intervals, fitted circles, MFS coefficients (with credible intervals) corresponding to the inner and outer boundaries.

From Figure 4.6 it can be seen that the accuracy of the reconstruction is as good as the corresponding reconstruction obtained in Experiment 1 (when only one rigid inclusion is considered), in terms of the estimated radii, centres and the outer MFS coefficients which still follow the true values. More precisely, for the rigid inclusion Ω_{Inner_1}, the estimated radii average is 0.4008 comparing to its true value 0.4, and a standard deviation of 0.0009, whilst the estimated centre is at $(-0.0004, 0.5004)$ comparing to the truth one which is $(0, 0.5)$. Moreover, for the rigid inclusion Ω_{Inner_2}, the estimated radii average is 0.4020 comparing to its true value 0.4 and a standard deviation of 0.00016 and estimated centre at $(0.0006, -0.5015)$ comparing to the truth centre $(0, 0.5)$. However, the estimated values of the inner MFS coefficients show oscillations with wide credible intervals when the number of inclusions is extended to two.

4.8 Conclusions

The Bayesian statistical approach in combination with an MCMC algorithm have been successfully employed to solve inverse CEM problems using simulated noisy data of the voltages. We have considered the voltage data as they are more sensitive to changes in the centre, the CCI and in extending the number of objects to two, than the potential and current flux data type. As a result, three different inverse problems have been examined and solved to provide full reconstruction of the inner objects. Firstly, the inverse CEM problem has been solved in an annular domain with a rigid inclusion where the centre of the inclusion is unknown (Section 4.3). Secondly, another inverse CEM problem has been solved in an annular domain with a rigid inclusion with unknown centre, as well unknown CCI values (Section 4.5). Finally, the inverse CEM problem has been solved in an annular domain with two rigid inclusions where the centres of these inclusions are unknown (Section 4.7). The experiments demonstrate that high accuracy reconstructions of the inner object are obtained when the number of the attached electrodes is $L = 8$.

Chapter 5

Extension to three-dimensions

5.1 Introduction

This chapter aims to extend the previous two-dimensional computations of direct and inverse problems to three dimensions. As a remarkable step towards solving the direct and the inverse CEM problems of ERT (future work), in a first attempt, we will consider the forward and inverse solutions of the continuous model of ERT in three dimensions. The MFS is again applied to find the forward solutions of the Dirichlet problem for the three-dimensional Laplace's equation in the unit sphere (Problem 1), or in the unit sphere with a spherical/ellisoidal rigid inclusion (Problem 2). We discuss the numerical results for a set of examples and compare them with the corresponding exact solutions where available.

Prior to this study, three-dimensional rigid inclusions have been reconstructed in [15, 39, 57] by standard regularization schemes, where the MFS was used to produce the direct solution and a constrained optimization procedure was employed for determining the boundary of a three-dimensional star-shaped rigid inclusion. In this chapter, we use the Bayesian approach, instead of the gradient-based minimization of [15], to find the inverse solution by extending the study of [6, 7] from two-dimensions to three-dimensions.

5.2 Mathematical formulation

In this section, we consider Laplace's equation for a three-dimensional bounded domain Ω, namely,

$$\triangle u = 0 \qquad \text{in } \Omega, \tag{5.1}$$

and formulate two forward problems for different geometries.

Problem 1: We consider Ω as the unit sphere $\Omega = \{(x, y, z) \in \mathbb{R}^3 | x^2 + y^2 + z^2 < 1\}$ and solve (5.1) subject to the Dirichlet boundary condition

$$u = f \qquad \text{on } \partial\Omega. \tag{5.2}$$

Problem 2: We consider an annular domain $\Omega = \Omega_{Outer} \backslash \overline{\Omega}_{Inner}$ with a rigid inclusion

(a) $\Omega_{Inner} = \{(x, y, z) \in \mathbb{R}^3 |\ x^2 + y^2 + z^2 < (0.5)^2\}$

or

(b) $\Omega_{Inner} = \left\{(x, y, z) \in \mathbb{R}^3 |\ \frac{x^2}{(0.5)^2} + \frac{y^2}{(0.5)^2} + \frac{z^2}{(0.4)^2} < 1\right\}$

inside the unit sphere $\Omega_{Outer} = \{(x, y, z) \in \mathbb{R}^3 | x^2 + y^2 + z^2 < 1\}$. Equation (5.1) is solved subject to the Dirichlet boundary conditions

$$u = f \qquad \text{on } \partial\Omega_{Outer} \tag{5.3}$$

and

$$u = 0 \qquad \text{on } \partial\Omega_{Inner}. \tag{5.4}$$

On the other hand, in the inverse formulation, since the concern is not only to find the potential u but also identifying the rigid inclusion Ω_{Inner}, the following Neumann current flux measurement is required to compensate for the unknown geometry of the

inner rigid inclusion $\partial\Omega_{Inner}$, namely,

$$\frac{\partial u}{\partial n} = g \qquad \text{on } \partial\Omega_{Outer}. \tag{5.5}$$

As a result, the inverse problem of the continuous model of ERT is given by equations (5.1) and (5.3)-(5.5). Uniqueness of this problem when $f \not\equiv 0$ is provided in Appendix A.

Problem 3: We consider an annular domain $\Omega = \Omega_{Outer} \backslash (\overline{\Omega}_{Inner1} \cup \overline{\Omega}_{Inner1})$ with two rigid inclusions, which need to be detected when the inverse problem is solved, defined by
$\Omega_{Inner1} = \left\{(x, y, z) \in \mathbb{R}^3 |\ x^2 + (y - 0.5)^2 + z^2 < (0.4)^2\right\}$
and $\Omega_{Inner1} = \left\{(x, y, z) \in \mathbb{R}^3 |\ x^2 + (y + 0.5)^2 + z^2 < (0.4)^2\right\}$.
These are located inside the unit sphere. Then, equation (5.1) is solved subject to (5.3), (5.5) and

$$u = 0 \qquad \text{on } \partial\Omega_{Inner1} \cup \partial\Omega_{Inner2}. \tag{5.6}$$

5.3 The MFS for the direct Problem 1

In this section, we seek an approximation to the solution of Laplace's equation (5.1) in the unit sphere as a linear combination of fundamental solutions in the following form:

$$u(\underline{p}) = \sum_{k=1}^{N-1} \sum_{l=1}^{N} c_{kl} G(\underline{\xi}_{k,l}, \underline{p}), \quad \underline{p} \in \overline{\Omega}, \tag{5.7}$$

where G is the fundamental solution of the three-dimensional Laplace's equation given by

$$G(\underline{\xi}, \underline{p}) = \frac{1}{4\pi|\underline{\xi} - \underline{p}|}. \tag{5.8}$$

The source points $\underline{\xi}_{k,l}$ are located outside $\overline{\Omega}$, and c_{kl} for $k = \overline{1,(N-1)}$ and $l = \overline{1,N}$ are unknown coefficients to be determined by imposing the Dirichlet boundary condition (5.2).

Since Ω is a sphere, we can use spherical coordinates for the boundary collocation and source points. This leads to

$$\underline{x}_{i,j} = (\sin\theta_i \cos\phi_j, \sin\theta_i \sin\phi_j, \cos\theta_i)\,, \quad i = \overline{1,(M-1)}, \quad j = \overline{1,M}, \tag{5.9}$$

$$\underline{\xi}_{k,l} = R\left(\sin\tilde{\theta}_k \cos\tilde{\phi}_l, \sin\tilde{\theta}_k \sin\tilde{\phi}_l, \cos\tilde{\theta}_k\right), \quad k = \overline{1,(N-1)}, \quad l = \overline{1,N}, \tag{5.10}$$

respectively, where $R > 1$,

$$\theta_i = \frac{\pi i}{M}, \quad i = \overline{1,(M-1)}, \quad \phi_j = \frac{2\pi(j-1)}{M}, \quad j = \overline{1,M}$$

and

$$\theta_k = \frac{\pi k}{N}, \quad k = \overline{1,(N-1)}, \quad \phi_l = \frac{2\pi(l-1)}{N}, \quad l = \overline{1,N}.$$

In total, the number of the collocation points is $(M-1) \times M$ and the number of the source points is $(N-1) \times N$.

From (5.7), the normal derivative is approximated as

$$\frac{\partial u}{\partial n}(\underline{p}) = \sum_{k=1}^{N-1} \sum_{l=1}^{N} c_{kl} \frac{\partial G}{\partial n}(\underline{\xi}_{k,l}, \underline{p}), \quad \underline{p} \in \partial\Omega, \tag{5.11}$$

where

$$\frac{\partial G}{\partial n}(\underline{\xi}_{k,l}, \underline{p}) = \left(\frac{\partial G}{\partial x} n_x + \frac{\partial G}{\partial y} n_y + \frac{\partial G}{\partial z} n_z\right)(\underline{\xi}_{k,l}, \underline{p}), \tag{5.12}$$

$$\frac{\partial G}{\partial x}(\underline{\xi}_{k,l}, \underline{p}) = -\frac{(x - \xi_{k,l})}{4\pi|\underline{p} - \underline{\xi}_{k,l}|^3}, \quad \frac{\partial G}{\partial y}(\underline{\xi}_{k,l}, \underline{p}) = -\frac{(y - \xi_{k,l})}{4\pi|\underline{p} - \underline{\xi}_{k,l}|^3},$$

$$\frac{\partial G}{\partial z}(\underline{\xi}_{k,l}, \underline{p}) = -\frac{(z - \xi_{k,l})}{4\pi|\underline{p} - \underline{\xi}_{k,l}|^3}, \quad k = \overline{1,(N-1)}, \quad l = \overline{1,N},$$

and the components of the outward unit normal vector to the unit sphere are

$$n_x = \sin\theta\cos\phi,\ n_y = \sin\theta\sin\phi,\ n_z = \cos\theta, \quad \theta \in (0,\pi),\ \phi \in [0, 2\pi).$$

In order to obtain the coefficient $\underline{c} = (c_{k,l})_{k=\overline{1,(N-1)},\, l=\overline{1,N}}$, we collocate equation (5.7) at the points (5.9) and use the boundary condition (5.2). This results in

$$\sum_{k=1}^{N-1}\sum_{l=1}^{N} G_{ijkl} c_{kl} = f_{i,j}, \quad i = \overline{1,(M-1)}, \quad j = \overline{1,M}, \tag{5.13}$$

where $f_{i,j} = f(\underline{x}_{i,j})$ and $G_{ijkl} = \frac{1}{4\pi|\underline{\xi}_{k,l} - \underline{x}_{i,j}|}$ for $i = \overline{1,(M-1)}$, $j = \overline{1,M}$, $k = \overline{1,(N-1)}$ and $l = \overline{1,N}$. Expression (5.13) can be re-written as

$$\sum_{n=1}^{N(N-1)} \tilde{F}_{m,n}\, \tilde{\mathbf{C}}_n = \tilde{\mathbf{b}}_m, \quad m = \overline{1, M(M-1)}, \tag{5.14}$$

where

$$\tilde{F} = \begin{pmatrix}
G_{1111} & G_{1112} & \dots & G_{111N} & \dots & G_{11(N-1)1} & G_{11(N-1)2} & \dots & G_{11(N-1)N} \\
G_{1211} & G_{1212} & \dots & G_{121N} & \dots & G_{12(N-1)1} & G_{12(N-1)2} & \dots & G_{12(N-1)N} \\
\vdots & \vdots & \vdots & \vdots & \vdots & \vdots & \vdots & \vdots & \vdots \\
G_{1M11} & G_{1M12} & \dots & G_{1M1N} & \dots & G_{1M(N-1)1} & G_{1M(N-1)2} & \dots & G_{1M(N-1)N} \\
G_{2111} & G_{2112} & \dots & G_{211N} & \dots & G_{21(N-1)1} & G_{21(N-1)2} & \dots & G_{21(N-1)N} \\
G_{2211} & G_{2212} & \dots & G_{221N} & \dots & G_{22(M-1)1} & G_{22(N-1)2} & \dots & G_{22(N-1)N} \\
\vdots & \vdots & \vdots & \vdots & \vdots & \vdots & \vdots & \vdots & \vdots \\
G_{2M11} & G_{2M12} & \dots & G_{2M1N} & \dots & G_{2M(M-1)1} & G_{2M(N-1)2} & \dots & G_{2M(N-1)N} \\
\vdots & \vdots & \vdots & \vdots & \vdots & \vdots & \vdots & \vdots & \vdots \\
G_{(M-1)111} & G_{(M-1)112} & \dots & G_{(M-1)11N} & \dots & G_{(M-1)1(N-1)1} & G_{(M-1)1(N-1)2} & \dots & G_{(M-1)1(N-1)N} \\
G_{(M-1)211} & G_{(M-1)212} & \dots & G_{(M-1)21N} & \dots & G_{(M-1)2(N-1)1} & G_{(M-1)2(N-1)2} & \dots & G_{(M-1)2(N-1)N} \\
\vdots & \vdots & \vdots & \vdots & \vdots & \vdots & \vdots & \vdots & \vdots \\
G_{(M-1)M11} & G_{(M-1)M12} & \dots & G_{(M-1)M1N} & \dots & G_{(M-1)M(N-1)1} & G_{(M-1)M(N-1)2} & \dots & G_{(M-1)M(N-1)N}
\end{pmatrix},$$

$$\tilde{\mathbf{C}} = \begin{pmatrix} c_{11} \\ c_{12} \\ \vdots \\ c_{1N} \\ c_{21} \\ c_{22} \\ \vdots \\ c_{2N} \\ \vdots \\ c_{(N-1)1} \\ c_{(N-1)2} \\ \vdots \\ c_{(N-1)N} \end{pmatrix} \text{ and } \tilde{\mathbf{b}} = \begin{pmatrix} f_{11} \\ f_{12} \\ \vdots \\ f_{1M} \\ f_{21} \\ f_{22} \\ \vdots \\ f_{2M} \\ \vdots \\ f_{(M-1)1} \\ f_{(M-1)2} \\ \vdots \\ f_{(M-1)M} \end{pmatrix}.$$

The linear system of algebraic equations (5.14) consists of $(M-1) \times M$ equations with $(N-1) \times N$ unknowns. If $M = N$, we can directly apply the Gauss elimination method to obtain the MFS coefficients $\tilde{\mathbf{C}}_n$. However, if $M > N$ the least-squares method is used to solve the over-determined system of equations (5.14). This yields the solution

$$\tilde{\mathbf{C}} = \left(\tilde{F}^T \tilde{F}\right)^{-1} \tilde{F}^T \tilde{\mathbf{b}}. \tag{5.15}$$

Once the coefficient vector $\tilde{\mathbf{C}}$ has been obtained accurately, equations (5.7) and (5.12) provide explicitly the solution for the interior potential u inside the domain Ω and the current flux $\partial u/\partial n$ on the boundary $\partial\Omega$.

5.3.1 Numerical results and discussion

In this section, we discuss the MFS solution of the direct Problem 1, given by equations (5.1) and (5.2), and compare the numerically obtained results with the exact solutions for the normal derivative on the boundary and the interior solution.

Example 1: Solve Problem 1 using the MFS where the analytical solution is

$$u(x, y, z) = x^2 + y^2 - 2z^2, \quad (x, y, z) \in \Omega. \tag{5.16}$$

Solution: Choosing $M = N = 16$ results in $15 \times 16 = 240$ collocation points which means 240 equations. On the other hand, the number of the source points is $15 \times 16 = 240$, this in turn, means that the number of the unknowns is 240, as well. We also have $R = 5$.

Figure 5.1 illustrates a comparisons between the exact and MFS interior solutions, as well as the exact and MFS normal derivatives. This figure shows excellent agreement between the exact and numerical solutions; up to 12 and 11 decimal places for interior solution and the normal derivative, respectively.

Figure 5.2 illustrates the absolute errors between the exact and numerical solutions previously illustrated in Figure 5.1. From this figure, it can be seen that the errors decrease as $M = N$ increases. Although the cases (e) and (f) (when $M = N = 32$) show smaller errors in terms of accuracy than (c) and (d) (when $M = N = 16$), the latter show better representations in terms of the smoothness of the numerical interior solutions and normal derivatives.

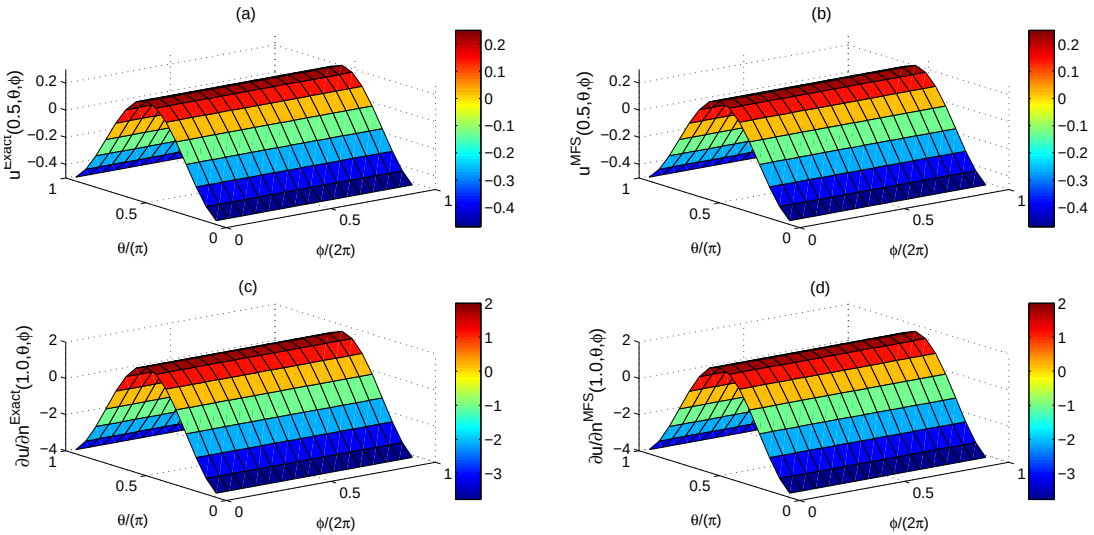

Figure 5.1: Comparison between (a) the exact interior solution $u^{Exact}(0.5, \theta, \phi)$ and (b) the MFS interior solutions $u^{MFS}(0.5, \theta, \phi)$, and comparison between (c) the exact boundary derivative $(\partial u/\partial n)^{Exact}(1, \theta, \phi)$ and (d) the MFS boundary derivative $(\partial u/\partial n)^{MFS}(1, \theta, \phi)$, as a functions of $\phi/(2\pi)$ and θ/π, when $M = N = 16$ and $R = 5$.

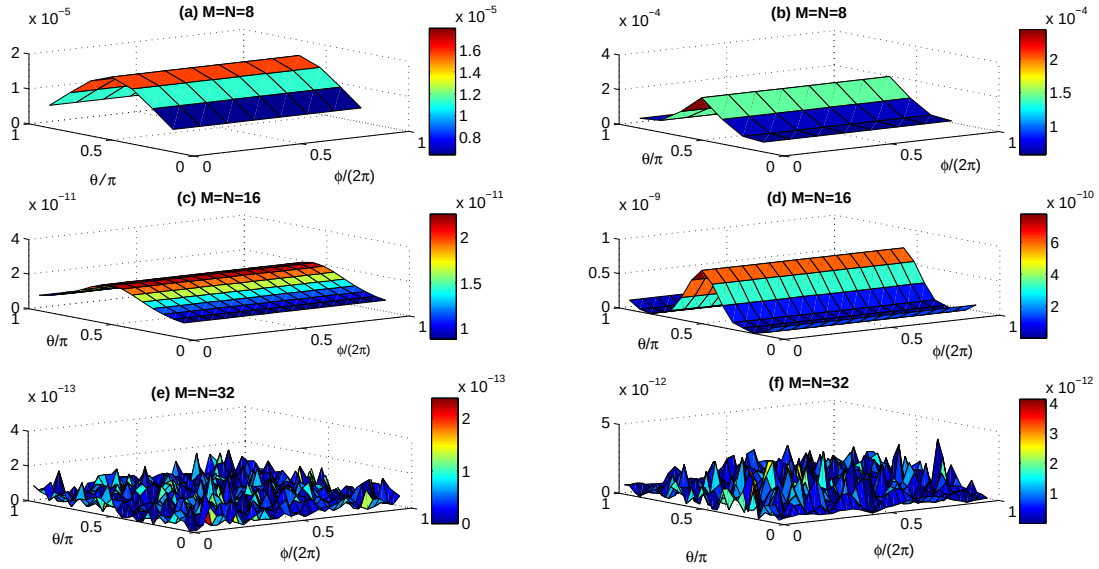

Figure 5.2: (a, c, e) the absolute errors between the MFS interior solutions $u^{MFS}(0.5, \theta, \phi)$ and the exact interior solution $u^{Exact}(0.5, \theta, \phi)$, for $M = N = \{8, 16, 32\}$, respectively, (b, d, f) the absolute errors between the MFS boundary derivative $(\partial u/\partial n^{MFS})(1, \theta, \phi)$ and the exact boundary derivative $(\partial u/\partial n^{Exact})(1, \theta, \phi)$, for $M = N = \{8, 16, 32\}$, respectively. In all cases $R = 5$.

Figure 5.3 illustrates the absolute errors between the exact and numerical interior solutions and normal derivatives for fixed $M = N = 16$ and various $R \in \{2, 5, 10\}$. From this figure, it can be seen that the errors decrease as R increases. Although the cases (e) and (f) (when $R = 10$) show smaller absolute errors in terms of accuracy than the cases (c) and (d) (when $R = 5$), the latter show better representations in terms of the smoothness of the numerical interior solutions and normal derivatives.

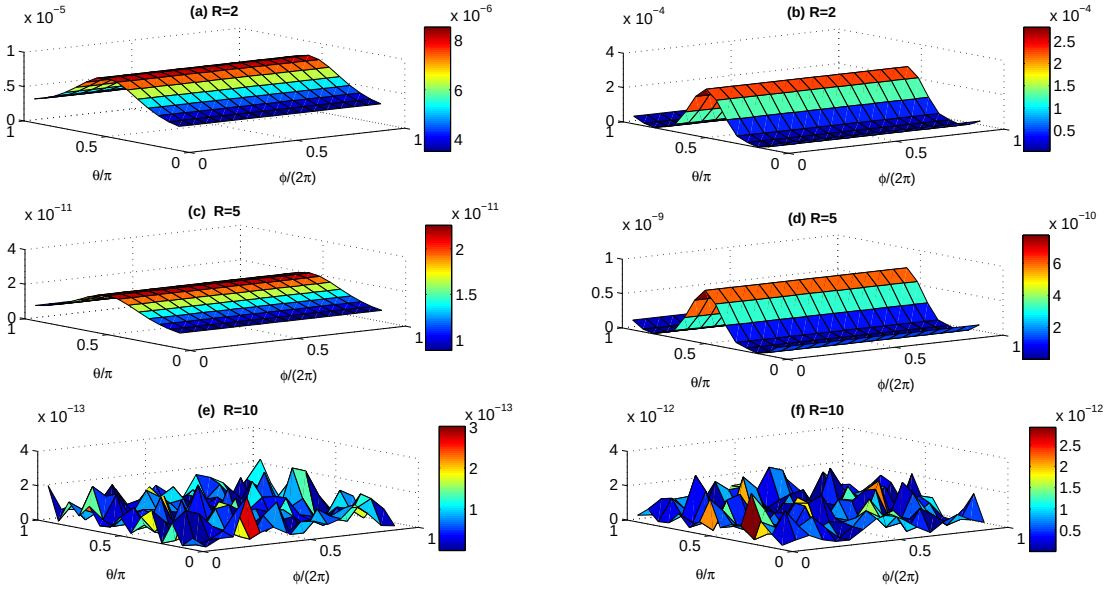

Figure 5.3: (a, c, e) the absolute errors between the MFS interior solutions $u^{MFS}(0.5, \theta, \phi)$ and the exact interior solution $u^{Exact}(0.5, \theta, \phi)$, for $R = \{2, 5, 10\}$, respectively, and (b, d, f) the absolute errors between the MFS boundary derivative $(\partial u/\partial n^{MFS})(1, \theta, \phi)$ and the exact boundary derivative $(\partial u/\partial n^{Exact})(1, \theta, \phi)$, for $R = \{2, 5, 10\}$, respectively. In all cases $M = N = 16$.

5.4 The MFS for the direct Problem 2

In this section, we seek an approximation to the solution of equation (5.1), in an annular bounded domain with a rigid inclusion inside, as a linear combination of fundamental

solutions in the following form:

$$u(\underline{p}) = \sum_{k=1}^{2(N-1)} \sum_{l=1}^{N} c_{kl} G(\underline{\xi}_{k,l}, \underline{p}), \quad \underline{p} \in \overline{\Omega}. \tag{5.17}$$

The internal source points denoted by $\underline{\xi}^1_{k,l}$, are located inside the inner domain Ω_{Inner}, and are defined, for Problem $2(a)$, by

$$\underline{\xi}^1_{k,l} = R_1 \left(\sin\tilde{\theta}_k \cos\tilde{\phi}_l, \sin\tilde{\theta}_k \sin\tilde{\phi}_l, \cos\tilde{\theta}_k \right), \quad k = \overline{1,(N-1)}, \quad l = \overline{1,N}, \tag{5.18}$$

where $0 < R_1 < 0.5$, and, for Problem $2(b)$, by

$$\underline{\xi}^1_{k,l} = \eta_I \left(0.5 \sin\tilde{\theta}_k \cos\tilde{\phi}_l, 0.5 \sin\tilde{\theta}_k \sin\tilde{\phi}_l, 0.4 \cos\tilde{\theta}_k \right), \quad k = \overline{1,(N-1)}, \quad l = \overline{1,N}, \tag{5.19}$$

where $0 < \eta_I < 1$. Whilst the external source points denoted by $\underline{\xi}^2_{k,l}$, are located outside the outer domain Ω_{Outer}, and are defined by

$$\underline{\xi}^2_{k,l} = R \left(\sin\tilde{\theta}_{k-N+1} \cos\tilde{\phi}_l, \sin\tilde{\theta}_{k-N+1} \sin\tilde{\phi}_l, \cos\tilde{\theta}_{k-N+1} \right), \quad k = \overline{N,2(N-1)}, \quad l = \overline{1,N}. \tag{5.20}$$

Similarly, the internal collocation points denoted by $\underline{x}^1_{i,j}$, are located on $\partial\Omega_{Inner}$, and are defined, for Problem $2(a)$, by

$$\underline{x}^1_{i,j} = 0.5 \left(\sin\theta_i \cos\phi_j, \sin\theta_i \sin\phi_j, \cos\theta_i \right), \quad i = \overline{1,(M-1)}, \quad j = \overline{1,M}, \tag{5.21}$$

and, for Problem $2(b)$, by

$$\underline{x}^1_{i,j} = \left(0.5 \sin\theta_i \cos\phi_j, 0.5 \sin\theta_i \sin\phi_j, 0.4 \cos\theta_i \right), \quad i = \overline{1,(M-1)}, \quad j = \overline{1,M}, \tag{5.22}$$

whilst the external collocation points denoted by $\underline{x}^2_{i,j}$ are located on $\partial\Omega_{Outer}$, and are defined by

$$\underline{x}^2_{i,j} = (\sin\theta_{i-M+1}\cos\phi_j, \sin\theta_{i-M+1}\sin\phi_j, \cos\theta_{i-M+1}),$$
$$i = \overline{M, 2(M-1)}, \quad j = \overline{1, M}. \tag{5.23}$$

As a result, in total the number of the collocation points is $2(M-1)\times M$ and the number of the source points is $2(N-1)\times N$; this means that the number of the MFS inner and outer coefficients is $2(N-1)\times N$.

Here, for any collocation point $\underline{p} = (x, y, z) \in \partial\Omega_{Inner}$, the component of the outward normal vector is

$$n_x = -\sin\theta\cos\phi,\ n_y = -\sin\theta\sin\phi,\ n_z = -\cos\theta, \quad \text{for} \quad \theta\in(0,\pi),\ \phi\in[0,2\pi).$$

In order to obtain the coefficient $\underline{c} = (c_{k,l})_{k=\overline{1,2(N-1)},\, l=\overline{1,N}}$, we substitute (5.17) into the boundary conditions (5.3) and (5.4). This results in

$$\sum_{k=1}^{2(N-1)}\sum_{l=1}^{N} G_{ijkl}c_{kl} = f_{i,j}, \quad i = \overline{1, 2(M-1)}, \quad j = \overline{1, M}, \tag{5.24}$$

where $f_{i,j} = f(\underline{x}_{i,j})$ and $G_{ijkl} = \frac{1}{4\pi|\underline{\xi}_{k,l}-\underline{x}_{i,j}|}$, for $i = \overline{1, 2(M-1)}$, $j = \overline{1, M}$, $k = \overline{1, 2(N-1)}$ and $l = \overline{1, N}$. Note that from (5.4), $f_{i,j} = 0$ for $i = \overline{1, (M-1)}, j = \overline{1, M}$. Equation (5.24) can be re-written as

$$\sum_{n=1}^{2N(N-1)} \hat{F}_{m,n}\,\hat{\mathbf{C}}_n = \hat{\mathbf{b}}_m, \quad m = \overline{1, 2M(M-1)}, \tag{5.25}$$

where

$$\hat{F} = \begin{pmatrix} G_{1111} & \dots & G_{111N} & \dots & G_{11[2(M-1)]1} & \dots & G_{11[2(N-1)]N} \\ G_{1211} & \dots & G_{121N} & \dots & G_{12[2(M-1)]1} & \dots & G_{12[2(N-1)]N} \\ \vdots & \vdots & \vdots & \vdots & \vdots & \vdots & \vdots \\ G_{1M11} & \dots & G_{1M1N} & \dots & G_{1M[2(M-1)]1} & \dots & G_{1M[2(N-1)]N} \\ G_{2111} & \dots & G_{211N} & \dots & G_{21[2(M-1)]1} & \dots & G_{21[2(N-1)]N} \\ G_{2211} & \dots & G_{221N} & \dots & G_{22[2(M-1)]1} & \dots & G_{22[2(N-1)]N} \\ \vdots & \vdots & \vdots & \vdots & \vdots & \vdots & \vdots \\ G_{2M11} & \dots & G_{2M1N} & \dots & G_{2M[2(M-1)]1} & \dots & G_{2M[2(N-1)]N} \\ \vdots & \vdots & \vdots & \vdots & \vdots & \vdots & \vdots \\ G_{[2(M-1)]111} & \dots & G_{[2(M-1)]11N} & \dots & G_{[2(M-1)]1[2(N-1)]2} & \dots & G_{[2(M-1)]1[2(N-1)]N} \\ G_{[2(M-1)]211} & \dots & G_{[2(M-1)]21N} & \dots & G_{[2(M-1)]2[2(N-1)]1} & \dots & G_{[2(M-1)]2[2(N-1)]N} \\ \vdots & \vdots & \vdots & \vdots & \vdots & \vdots & \vdots \\ G_{[2(M-1)]M11} & \dots & G_{[2(M-1)]M1N} & \dots & G_{[2(M-1)]M[2(N-1)]1} & \dots & G_{[2(M-1)]M[2(N-1)]N} \end{pmatrix},$$

$$\hat{\mathbf{C}} = \begin{pmatrix} c_{11} \\ c_{12} \\ \vdots \\ c_{1N} \\ c_{21} \\ c_{22} \\ \vdots \\ c_{2N} \\ \vdots \\ c_{[2(N-1)]1} \\ c_{[2(N-1)]2} \\ \vdots \\ c_{[2(N-1)]N} \end{pmatrix} \text{ and } \hat{\mathbf{b}} = \begin{pmatrix} f_{11} \\ f_{12} \\ \vdots \\ f_{1M} \\ f_{21} \\ f_{22} \\ \vdots \\ f_{2M} \\ \vdots \\ f_{[2(M-1)]1} \\ f_{[2(M-1)]2} \\ \vdots \\ f_{[2(M-1)]M} \end{pmatrix}.$$

The above linear system of algebraic equations (5.25) consists of $2(M-1) \times M$ equations with $2(N-1) \times N$ unknowns. Its solution can be obtained as described at the end of subsection 5.3.

5.4.1 Numerical results and discussion

In this section, we will discuss and compare the direct numerical and exact solutions of Problem 2 given by equations (5.1), (5.3) and (5.4), for the normal derivatives on the inner and outer boundaries and the interior solutions.

Example 2: Solve Problem $2(a)$ using the MFS where the analytical solution is given

by

$$u(x,y,z) = \frac{1}{\sqrt{x^2+y^2+z^2}} - \frac{1}{0.5}. \tag{5.26}$$

Solution: Choosing $M = N = 16$, resulting in $30 \times 16 = 480$ collocation points and 480 source points. We also take $R = 5$ and $R_1 = 0.3$.

Figure 5.4 illustrates a comparisons between the exact interior solutions and the MFS interior solutions, as well as the corresponding normal derivatives on $\partial\Omega_{Inner}$ and $\partial\Omega_{Outer}$. This figure shows an excellent agreement between the exact and the numerical MFS solutions up to 5 or 6 decimal places.

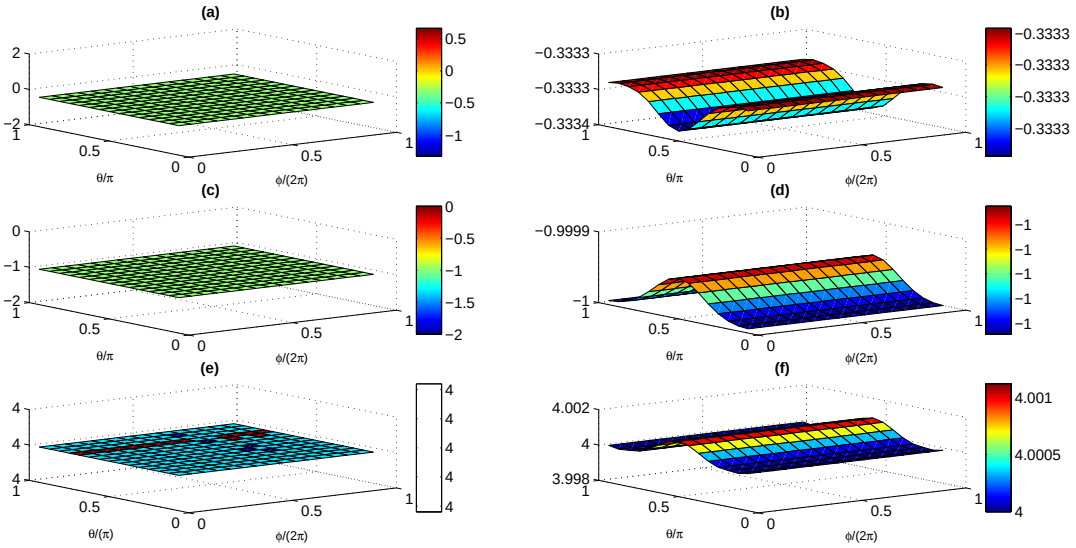

Figure 5.4: (a) The exact interior solution $u^{Exact}(0.6,\theta,\phi)$ and (b) the MFS interior solutions $u^{MFS}(0.6,\theta,\phi)$, (c) the exact outer derivative $(\partial u/\partial n)^{Exact}_{Outer}(1,\theta,\phi)$, (d) the MFS outer derivative $(\partial u/\partial n)^{MFS}_{Outer}(1,\theta,\phi)$, (e) the inner exact derivative $(\partial u/\partial n)^{Exact}_{Inner}(0.5,\theta,\phi)$, and (f) the MFS inner derivative $(\partial u/\partial n)^{MFS}_{Inner}(0.5,\theta,\phi)$, as a functions of $\phi/(2\pi)$ and θ/π, when $M = N = 16$, $R = 5$ and $R_1 = 0.3$.

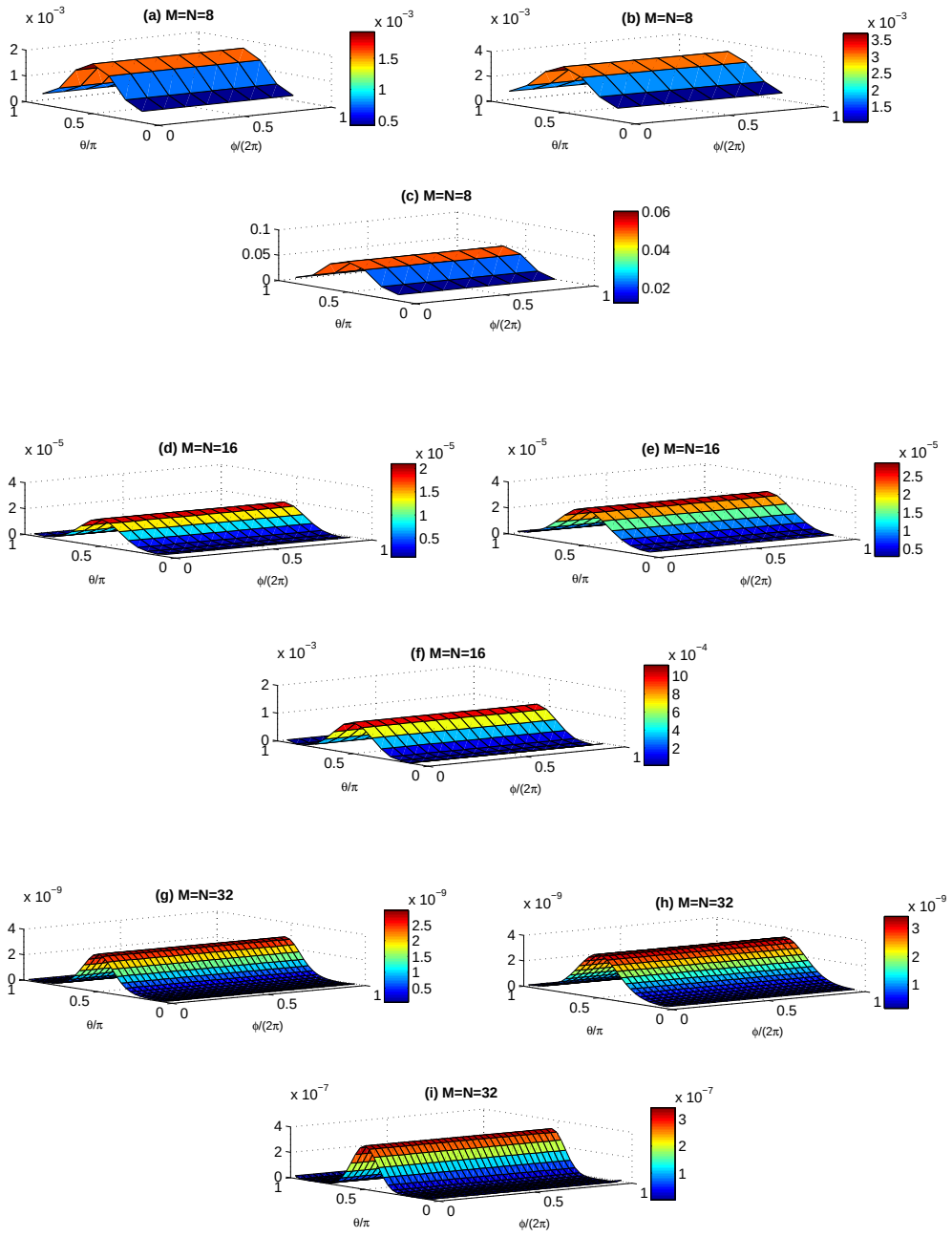

Figure 5.5: (a, d, g) The absolute errors between the MFS interior solutions $u^{MFS}(0.6, \theta, \phi)$ and the exact interior solution $u^{Exact}(0.6, \theta, \phi)$, for $M = N = \{8, 16, 32\}$, respectively, (b, e, h) the absolute errors between the MFS outer derivative $(\partial u/\partial n^{MFS})(1, \theta, \phi)$ and the exact outer derivative $(\partial u/\partial n^{Exact})(1, \theta, \phi)$, for $M = N = \{8, 16, 32\}$, respectively, and (c, f, i) the absolute errors between the MFS inner derivative $(\partial u/\partial n^{MFS})(0.5, \theta, \phi)$ and the exact inner derivative $(\partial u/\partial n^{Exact})(0.5, \theta, \phi)$, for $M = N = \{8, 16, 32\}$, respectively, as a functions of $\phi/(2\pi)$ and θ/π, when $R = 5$ and $R_1 = 0.3$.

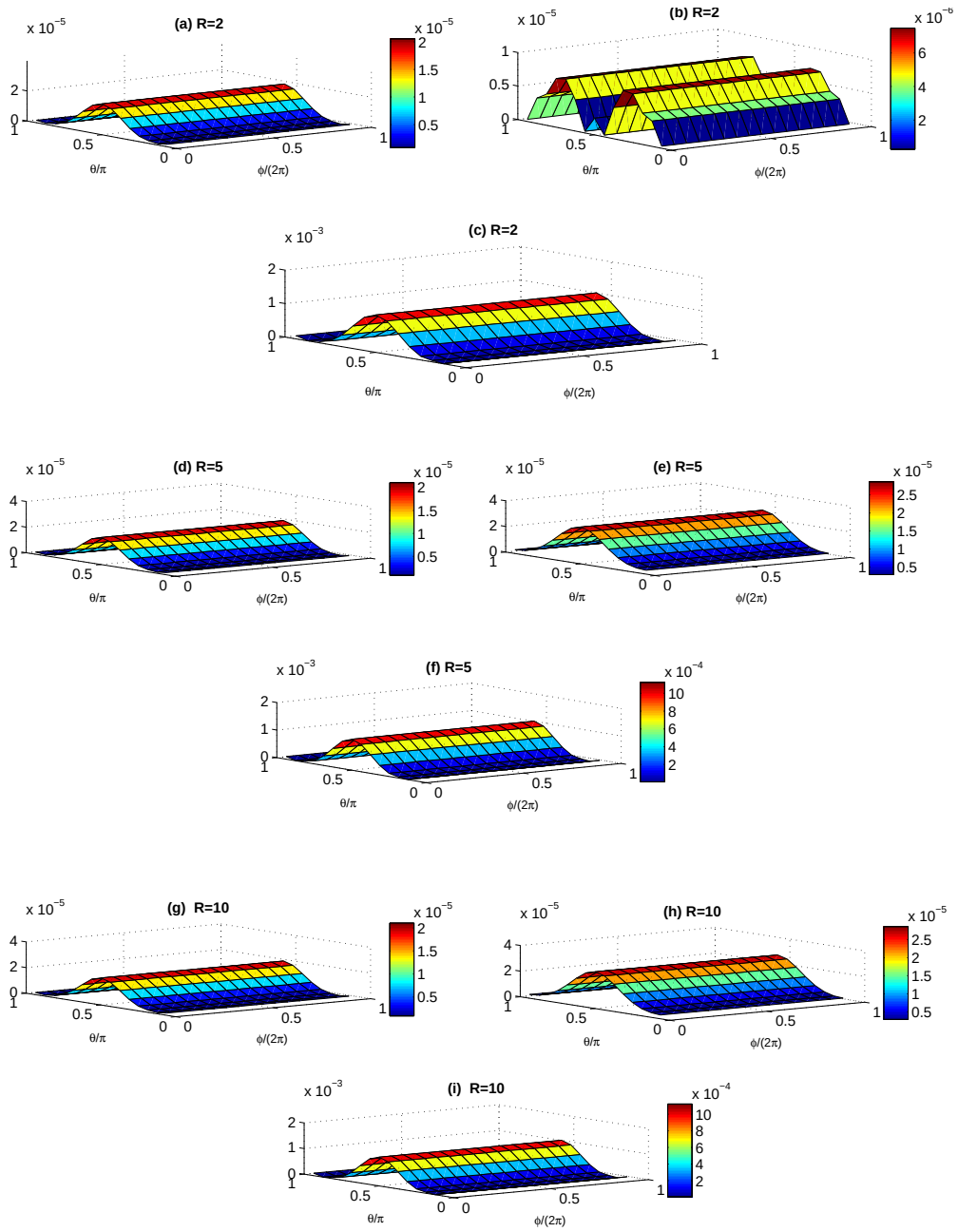

Figure 5.6: (a, d, g) The absolute errors between the MFS interior solutions $u^{MFS}(0.6, \theta, \phi)$ and the exact interior solution $u^{Exact}(0.6, \theta, \phi)$, for $R = \{2, 5, 10\}$, respectively, (b, e, h) the absolute errors between the MFS outer derivative $(\partial u/\partial n)^{MFS}(1, \theta, \phi)$ and the exact outer derivative $(\partial u/\partial n)^{Exact}(1, \theta, \phi)$, for $R = \{2, 5, 10\}$, respectively, (c, f, i) the absolute errors between the MFS inner derivative $(\partial u/\partial n)^{MFS}(0.5, \theta, \phi)$ and the exact inner derivative $(\partial u/\partial n)^{Exact}(0.5, \theta, \phi)$, for $R = \{2, 5, 10\}$, respectively, as a functions of $\phi/(2\pi)$, when θ/π and $M = N = 16$ and $R_1 = 0.3$.

Figures 5.5 and 5.6 illustrate the absolute errors between the exact the numerical MFS solutions for various values of $M = N \in \{8, 16, 32\}$ when $R = 5$, and for various $R \in \{2, 5, 10\}$ when $M = M = 16$, respectively. In these figures R_1 is fixed at 0.3. From Figure 5.5, it can be seen that as $M = N$ increases, the accuracy of MFS solution increases. However, increasing R from 2 to 5 (when $M = N = 16$) makes those solutions even better and choosing $R = 5$ provides the same accuracy as when $R = 5$, for $M = N = 16$.

5.5 The MFS for the direct Problem 3

In this section, we seek an approximation to the solution of equation (5.1), in an annular bounded domain with two rigid inclusions inside, as a linear combination of fundamental solutions in the following form:

$$u(\underline{p}) = \sum_{k=1}^{3(N-1)} \sum_{l=1}^{N} c_{kl} G(\underline{\xi}_{k,l}, \underline{p}), \quad \underline{p} \in \overline{\Omega}. \tag{5.27}$$

The internal source points for the first rigid inclusion denoted by $\underline{\xi}^1_{k,l}$, are located inside the inner domain Ω_{Inner1}, and are defined, for Problem 3, by

$$\underline{\xi}^1_{k,l} = R_1 \left(\sin\tilde{\theta}_k \cos\tilde{\phi}_l, \sin\tilde{\theta}_k \sin\tilde{\phi}_l, \cos\tilde{\theta}_k \right), \quad k = \overline{1, (N-1)}, \quad l = \overline{1, N}, \tag{5.28}$$

where $0 < R_1 < 0.4$, and denoted by $\underline{\xi}^2_{k,l}$ for the second inclusion, are located inside the inner domain Ω_{Inner2}, and are defined by

$$\underline{\xi}^2_{k,l} = R_2 \left(\sin\tilde{\theta}_{k-N+1} \cos\tilde{\phi}_l, \sin\tilde{\theta}_{k-N+1} \sin\tilde{\phi}_l, \cos\tilde{\theta}_{k-N+1} \right), \\ k = \overline{N, 2(N-1)}, \quad l = \overline{1, N}, \tag{5.29}$$

where $0 < R_2 < 0.4$, as well. Whilst the external source points, denoted by $\underline{\xi}^3_{k,l}$, are located outside the outer domain Ω_{Outer}, and are defined by

$$\underline{\xi}^3_{k,l} = R\left(\sin\tilde{\theta}_{k-[2(N-1)+1]+1}\cos\tilde{\phi}_l, \sin\tilde{\theta}_{k-[2(N-1)+1]+1}\sin\tilde{\phi}_l, \cos\tilde{\theta}_{k-[2(N-1)+1]+1}\right),$$
$$k = \overline{[2(N-1)+1], 3(N-1)}, \quad l = \overline{1, N}. \tag{5.30}$$

Similarly, the internal collocation points for the first inclusion denoted by $\underline{x}^1_{i,j}$, are located on $\partial\Omega_{Inner1}$, and are defined, for Problem 3, by

$$\underline{x}^1_{i,j} = 0.4\left(\sin\theta_i\cos\phi_j, \sin\theta_i\sin\phi_j, \cos\theta_i\right), \quad i = \overline{1, (M-1)}, \quad j = \overline{1, M}, \tag{5.31}$$

and for second inclusion of Problem 3, the internal collocation points are denoted by $\underline{x}^2_{i,j}$ and located on $\partial\Omega_{Inner2}$

$$\underline{x}^2_{i,j} = 0.4\left(\sin\theta_{i-M+1}\cos\phi_j, \sin\theta_{i-M+1}\sin\phi_j, \cos\theta_{i-M+1}\right),$$
$$i = \overline{M, 2(M-1)}, \quad j = \overline{1, M}, \tag{5.32}$$

whilst, the external collocation points denoted by $\underline{x}^3_{i,j}$, are located on $\partial\Omega_{Outer}$, and are defined by

$$\underline{x}^3_{i,j} = \left(\sin\theta_{i-[2(M-1)+1]+1}\cos\phi_j, \sin\theta_{i-[2(M-1)+1]+1}\sin\phi_j, \cos\theta_{i-[2(M-1)+1]+1}\right),$$
$$i = \overline{[2(M-1)+1], 3(M-1)}, \quad j = \overline{1, M}. \tag{5.33}$$

As a result, in total the number of the collocation points is $3(M-1)\times M$ and the number of the source points is $3(N-1)\times N$ which in turn means that the number of the MFS inner and outer coefficients is $3(N-1)\times N$.

In order to obtain the coefficient $\underline{c} = (c_{k,l})_{k=\overline{1,3(N-1)},\, l=\overline{1,N}}$, we substitute (5.27) into

the boundary conditions (5.3) and (5.6). This results in

$$\sum_{k=1}^{3(N-1)} \sum_{l=1}^{N} G_{ijkl} c_{kl} = f_{i,j}, \quad i = \overline{1, 3(M-1)}, \quad j = \overline{1, M}, \tag{5.34}$$

where $f_{i,j} = f(\underline{x}_{i,j})$ and $G_{ijkl} = \frac{1}{4\pi|\underline{\xi}_{k,l} - \underline{x}_{i,j}|}$, for $i = \overline{1, 3(M-1)}$, $j = \overline{1, M}$, $k = \overline{1, 3(N-1)}$ and $l = \overline{1, N}$. Note that from (5.6), $f_{i,j} = 0$ for $i = \overline{1, 2(M-1)}, j = \overline{1, M}$. Equation (5.34) can be re-written as

$$\sum_{n=1}^{3N(N-1)} \breve{F}_{m,n}\, \breve{\mathbf{C}}_n = \breve{\mathbf{b}}_m, \quad m = \overline{1, 3M(M-1)}, \tag{5.35}$$

where

$$\breve{F} = \begin{pmatrix}
G_{1111} & \dots & G_{111N} & \dots & G_{11[3(M-1)]1} & \dots & G_{11[3(N-1)]N} \\
G_{1211} & \dots & G_{121N} & \dots & G_{12[3(M-1)]1} & \dots & G_{12[3(N-1)]N} \\
\vdots & \vdots & \vdots & \vdots & \vdots & \vdots & \vdots \\
G_{1M11} & \dots & G_{1M1N} & \dots & G_{1M[3(M-1)]1} & \dots & G_{1M[3(N-1)]N} \\
G_{2111} & \dots & G_{211N} & \dots & G_{21[3(M-1)]1} & \dots & G_{21[3(N-1)]N} \\
G_{2211} & \dots & G_{221N} & \dots & G_{22[3(M-1)]1} & \dots & G_{22[3(N-1)]N} \\
\vdots & \vdots & \vdots & \vdots & \vdots & \vdots & \vdots \\
G_{2M11} & \dots & G_{2M1N} & \dots & G_{2M[3(M-1)]1} & \dots & G_{2M[3(N-1)]N} \\
\vdots & \vdots & \vdots & \vdots & \vdots & \vdots & \vdots \\
G_{[3(M-1)]111} & \dots & G_{[3(M-1)]11N} & \dots & G_{[3(M-1)]1[3(N-1)]2} & \dots & G_{[3(M-1)]1[3(N-1)]N} \\
G_{[3(M-1)]211} & \dots & G_{[3(M-1)]21N} & \dots & G_{[3(M-1)]2[3(N-1)]1} & \dots & G_{[3(M-1)]2[3(N-1)]N} \\
\vdots & \vdots & \vdots & \vdots & \vdots & \vdots & \vdots \\
G_{[3(M-1)]M11} & \dots & G_{[3(M-1)]M1N} & \dots & G_{[3(M-1)]M[3(N-1)]1} & \dots & G_{[3(M-1)]M[3(N-1)]N}
\end{pmatrix},$$

$$\breve{\mathbf{C}} = \begin{pmatrix} c_{11} \\ c_{12} \\ \vdots \\ c_{1N} \\ c_{21} \\ c_{22} \\ \vdots \\ c_{2N} \\ \vdots \\ c_{[3(N-1)]1} \\ c_{[3(N-1)]2} \\ \vdots \\ c_{[3(N-1)]N} \end{pmatrix} \text{ and } \breve{\mathbf{b}} = \begin{pmatrix} f_{11} \\ f_{12} \\ \vdots \\ f_{1M} \\ f_{21} \\ f_{22} \\ \vdots \\ f_{2M} \\ \vdots \\ f_{[3(M-1)]1} \\ f_{[3(M-1)]2} \\ \vdots \\ f_{[3(M-1)]M} \end{pmatrix}.$$

The above linear system of algebraic equations (5.35) consists of $3(M-1) \times M$ equations with $3(N-1) \times N$ unknowns. Its solution can be obtained as described at

the end of subsection 5.3.

5.5.1 Numerical results and discussion

In this section, as the analytical solution is not available we will represent only the direct numerical of the outer derivative which will be used afterwards to determine the shape and the size of the inner rigid inclusions in Problem 3 given by equations (5.1), (5.3) and (5.6).

Example 3: Consider the numerical solution of the forward problem of Problem 3 using the MFS where the function f in the boundary condition (5.3) is equal to $u(x, y, z) = x^2 + y^2 - 2z^2$.

Solution: Choose $M = N = 16$, resulting in $45 \times 16 = 720$ collocation points and 720 source points and set $R = 5$ and $R_{1,2} = 0.3$.

Figure 5.7 illustrates the MFS numerical normal derivatives on the external boundary for fixed $M = N = 16$ and various $R \in \{2, 5, 10\}$. From this figure, it can be seen that making R larger does not greatly affect the values of the normal derivative in terms of stability and smoothness. Figure 5.8 shows the same MFS numerical values for fixed $R = 5$ and various $M = N \in \{8, 16, 32, 64\}$. In both Figures 5.7 and 5.8 it is obvious that the two peaks are caused by the existence of the two inner rigid inclusions.

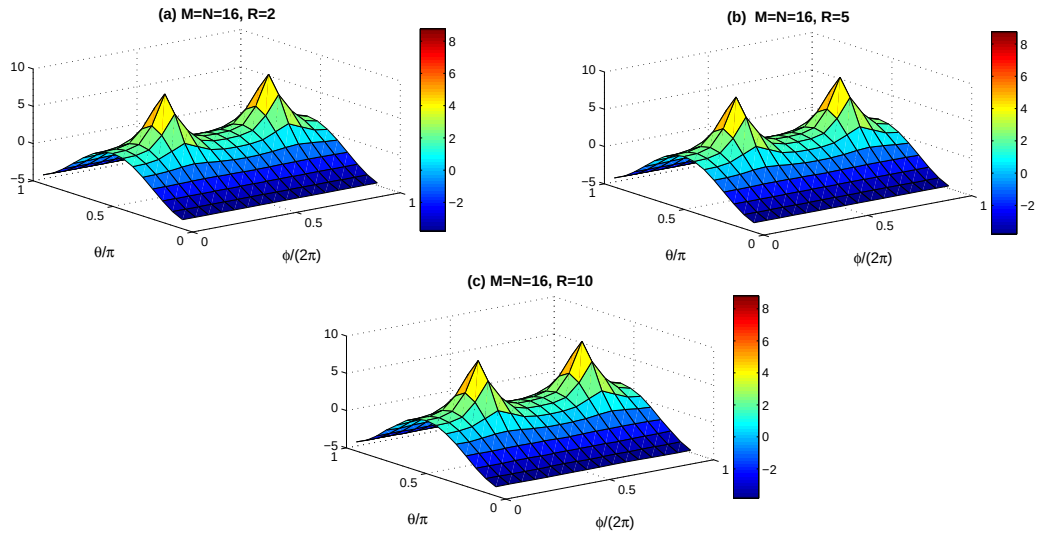

Figure 5.7: (a, b, c) the MFS outer derivative $(\partial u/\partial n)^{MFS}_{Outer}(1, \theta, \phi)$, as a functions of $\phi/(2\pi)$ and θ/π, when $M = N = 16$, $R = \{2, 5, 10\}$ and $R_{1,2} = 0.3$.

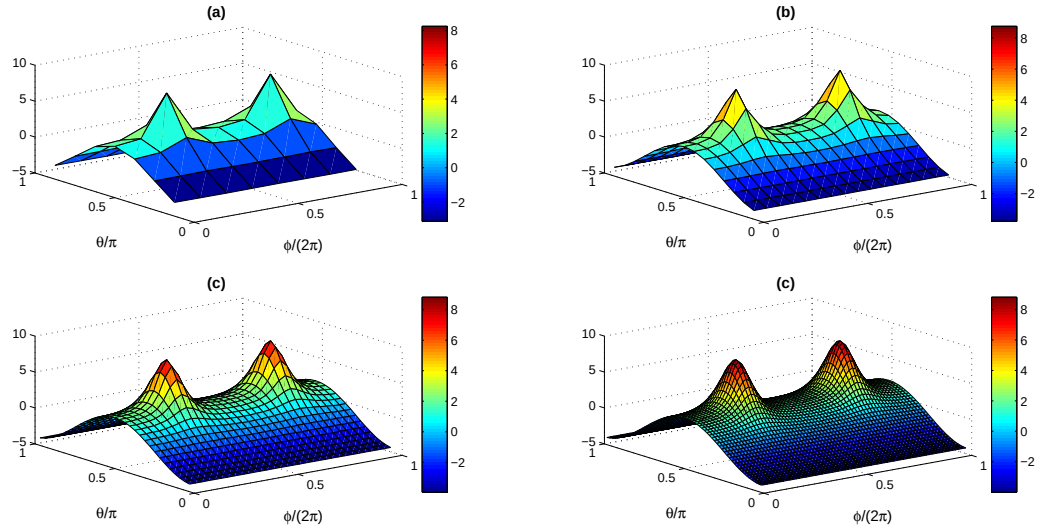

Figure 5.8: the MFS outer derivative $(\partial u/\partial n)^{MFS}_{Outer}(1, \theta, \phi)$, as a functions of $\phi/(2\pi)$ and θ/π, when $M = N = \{8, 16, 32, 64\}$, $R = 5$ and $R_{1,2} = 0.3$.

5.6 The inverse solution for the continuous model of ERT in three dimensions

We extend the study of [6, 7] concerning the solution of the inverse problem of the two-dimensional continuous model of ERT to three dimensions. More clearly, we will invert the continuous model of ERT in three dimensions using the same strategy that has been applied throughout Chapters 3 and 4 for the CEM, where the MFS direct solutions were combined with the MCMC method to detect (a) a single inner rigid object and (b) two rigid inclusions as described in Section 4.7. The inclusion model parameters will be firstly defined and the description of the MFS will then be given. Also, the necessary modifications in the statistical modelling approach (corresponding to Sections $3.3.1$ and $3.3.2$) will be considered. Finally, numerical simulations are reported to demonstrate the efficiency of the estimation procedure.

5.6.1 Mathematical formulation of one rigid inclusion

Let us assume that we have a three-dimensional star-shaped object Ω_{Inner} centered at the origin in the unit sphere Ω and parametrised by

$$r_{ij} = r(\theta_i, \phi_j), \quad i = \overline{1,(N-1)}\ j = \overline{1,N}, \tag{5.36}$$

using the spherical coordinated representation

$$\Omega_{Inner} = \{r(\theta,\phi)\,(\sin\theta\cos\phi, \sin\theta\sin\phi, \cos\theta) \mid \phi \in [0,2\pi], \theta \in [0,\pi)\}. \tag{5.37}$$

The input data consists of the potential and current flux given by (5.3) and (5.5), respectively.

As in Chapter 3, the boundary potential u is specified as in (5.3) and the current flux $\partial u/\partial n$ is obtained numerically by solving the direct problem of Problem 2, as

described in Section 5.4, in order to provide the current flux data (5.5). Afterwards, the potential and current flux values are corrupted with noise as

$$w_{i,j} = f(x_{i,j}) + \eta_{i,j}, \quad v_{i,j} = g(x_{i,j}) + \zeta_{i,j},\ i = \overline{M, 2(M-1)}, \quad j = \overline{1, M}, \quad (5.38)$$

where the additive noise variables $\eta_{i,j}$ and $\zeta_{i,j}$ follow independent Gaussian distributions which have zero means and variances σ_w^2 and σ_v^2, respectively.

The rigid-inclusion condition (5.4) must be imposed as

$$\sum_{k=1}^{2(N-1)} \sum_{l=1}^{N} c_{kl} G\left(\underline{\xi}_{k,l}, r_{i,j}(\sin\theta_i \cos\phi_j, \sin\theta_i \sin\phi_j, \cos\theta_i)\right) = 0, \quad i = \overline{1, (N-1)},\ j = \overline{1, N}. \quad (5.39)$$

It is noticeable that the MFS introduces an extra $2(N-1) \times N$ unknowns which are represented in the MFS inner and outer coefficients. These coefficients could be estimated simultaneously with the $(N-1) \times N$ radii of the star-shaped object from the system of equations (5.39), as well as fitting equations (5.17) and the corresponding approximation of the derivative as a linear combination of fundamental solutions to match the Cauchy data pair (5.38), that is,

$$\sum_{k=1}^{2(N-1)} \sum_{l=1}^{N} c_{kl} G(\underline{\xi}_{k,l}, \underline{x}_{i,j}) = w_{i,j}, \quad i = \overline{M, 2(M-1)},\ j = \overline{1, M}, \quad (5.40)$$

and

$$\sum_{k=1}^{2(N-1)} \sum_{l=1}^{N} c_{kl} \frac{\partial G}{\partial n}(\underline{\xi}_{k,l}, \underline{x}_{i,j}) = v_{i,j}, \quad i = \overline{M, 2(M-1)},\ j = \overline{1, M}. \quad (5.41)$$

Equations (5.39)-(5.41) create a system of $(N-1) \times N + 2(M-1) \times M$ equations with $3(N-1) \times N$ unknowns. Although the linearity in $\underline{c}$ is obvious in equations (5.40) and (5.41), equation (5.39) clearly shows nonlinearity between $\underline{r}$ and $\underline{c}$.

The constraint $0 < r_{ij} < 1$ for $i = \overline{1, (N-1)},\ j = \overline{1, N}$ should be imposed to

ensure that the inner star-shaped object remains within the unit sphere during the reconstruction process.

5.6.2 Mathematical formulation of two rigid inclusions

Let us assume that we have two three-dimensional star-shaped objects Ω_{Inner1} and Ω_{Inner2} centered at given points say, (X_0, Y_0, Z_0) and (X_1, Y_1, Z_1) in the unit sphere Ω and represented by $\underline{r}_1 = (r^1_{ij})_{i=\overline{1,(N-1)},\, j=\overline{1,N}}$ and $\underline{r}_2 = (r^2_{ij})_{i=\overline{1,(N-1)},\, j=\overline{1,N}}$, respectively.

The boundary potential u is specified as in (5.3) and the current flux $\partial u/\partial n$ is obtained numerically by solving the direct problem of Problem 3, as described in Section 5.5, in order to provide the current flux data (5.5). Then, the potential and current flux values are corrupted with noise as

$$w_{i,j} = f(x_{i,j}) + \eta_{i,j},\ v_{i,j} = g(x_{i,j}) + \zeta_{i,j},\ i = \overline{(2(M-1)+1)\,, 3(M-1)},\ j = \overline{1, M}. \tag{5.42}$$

The rigid-inclusion condition (5.6) is imposed as

$$\sum_{k=1}^{3(N-1)} \sum_{l=1}^{N} c_{kl} G\left(\underline{\xi}_{k,l}, r_{i,j}(\sin\theta_i \cos\phi_j, \sin\theta_i \sin\phi_j, \cos\theta_i)\right) = 0,$$
$$i = \overline{1, 2(N-1)},\ j = \overline{1, N}. \tag{5.43}$$

Now, it can be seen that the MFS introduces an extra $3(N-1) \times N$ unknowns which are represented in $2(N-1) \times N$ inner coefficients linked to the source points of the first and the second inclusions, and $(N-1) \times N$ outer coefficients linked to the external source points. These coefficients are estimated simultaneously with the $2(N-1) \times N$ radii of the star-shaped objects from the system of equations (5.43), as well as fitting equations (5.27) and the corresponding approximation of the derivative as a linear combination of fundamental solutions to match the Cauchy data pair (5.42),

that is,

$$\sum_{k=1}^{3(N-1)} \sum_{l=1}^{N} c_{kl} G(\underline{\xi}_{k,l}, \underline{x}_{i,j}) = w_{i,j},\ i = \overline{(2(M-1)+1)\,, 3(M-1)},\ j = \overline{1, M}, \tag{5.44}$$

and

$$\sum_{k=1}^{3(N-1)} \sum_{l=1}^{N} c_{kl} \frac{\partial G}{\partial n}(\underline{\xi}_{k,l}, \underline{x}_{i,j}) = v_{i,j},\ i = \overline{(2(M-1)+1)\,, 2(M-1)},\ j = \overline{1, M}. \tag{5.45}$$

Equations (5.43)-(5.45) create a system of $2(N-1) \times N + 2(M-1) \times M$ equations with $5(N-1) \times N$ unknowns.

We need to take into account that the distance between the centres should be greater than the sum of the diameters

$$S = \sqrt{(X_0 - X_1)^2 + (Y_0 - Y_1)^2 + (Z_0 - Z_1)^2} > \text{diam}(\Omega_{Inner_1}) + \text{diam}(\Omega_{Inner_2}), \tag{5.46}$$

where the diameters of Ω_{Inner_1} and Ω_{Inner_2} are defined in equations (4.13) and (4.14), respectively, with $\underline{x} = (x_1, x_2, x_3)$ and $\underline{y} = (y_1, y_2, y_3)$.

5.6.3 Statistical modelling in three-dimensions

The only modifications to the statistical modeling (Section 3.3.1) is that the data and the model parameters become matrices instead of vectors. Considering the case where we have one rigid inclusion, the potential values are $\underline{w} = (w_{i,j})_{i=\overline{M,2(M-1)},\ j=\overline{1,M}}$ and the current flux values $\underline{v} = (v_{i,j})_{i=\overline{M,2(M-1)},\ j=\overline{1,M}}$, whilst the model parameters are the radii $\underline{r} = (r_{i,j})_{i=\overline{1,(N-1)},\ j=\overline{1,N}}$ and MFS coefficients $\underline{c} = (c_{k,l})_{k=\overline{1,2(N-1)},\ l=\overline{1,N}}$. The formulas of the likelihoods, the priors and the hyper-prior, and the full posterior distri-

bution stay the same after giving consideration to the dimensionality of each variable.

Experiment 1. Find the inverse solution of Problem $2(a)$ by fitting:

(a) A spherical object model using the data from a spherical inclusion of radius 0.5 centred at $(0, 0, 0)$.

(b) A star-shaped object model using the data from a spherical inclusion of radius 0.5 centred at $(0, 0, 0)$.

First of all, we calculate numerically the current flux $\partial u/\partial u$ on the external boundary $\partial\Omega_{Outer}$ by solving the forward Dirichlet problem (5.1) and (5.3)-(5.4), as in Example 2, using the MFS with $(N-1)N = 35 \times 36 = 1260$. Then, the measured potential and current flux (5.38) are calculated on a mesh of equally-spaced collocation points, with $(M-1)M = 13 \times 14 = 182$, on the external fixed boundary of $\partial\Omega_{Outer}$. Data defined in (5.38) is generated by adding Gaussian noise to those boundary measurements with a standard deviation $\sigma_w = \sigma_v = 0.01$.

We take $(N-1)N = 14 \times 15 = 210$ which makes the discretised problem (that defined in (5.39)-(5.41)) under-determined, since it consists of $(N-1)N+2(M-1)M = 210 + 2 \times 182 = 574$ equations with $3(N-1)N = 3 \times 210 = 630$ unknowns. We take $\eta_I = 0.6$, $R = 5$ and $R_1 = 0.3$.

Secondly, the hierarchical structure of the statistical model in the right side of Figure 3.8 is considered here. Moreover, is it reasonable to use the same hyper-prior parameters that have been used in [6] and worked well for Experiment 3.3. So, we fix the values of the hyper-prior parameters of the internal and external MFS coefficients at $\alpha_{C_I} = 0.0116$ and $\alpha_{C_E} = 0.2457$, respectively, as well as the hyper-prior parameter value for the radius at $\alpha_r = 0.1$.

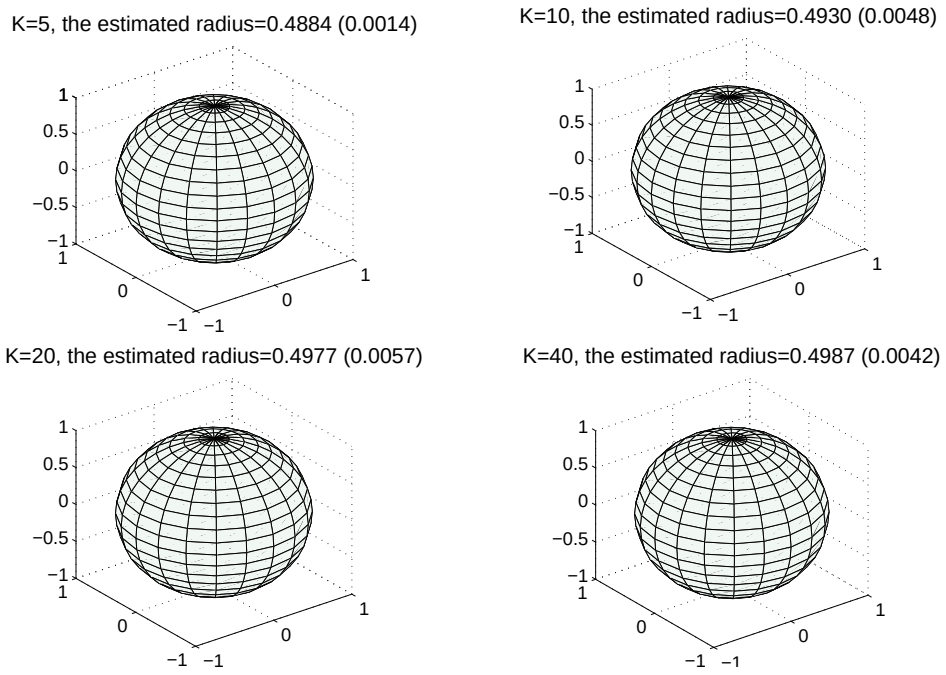

Figure 5.9: Spherical model reconstruction: the estimated radius for various MCMC iterations $K \in \{5, 10, 20, 40\}$, for with full posterior distribution with hyper-prior parameters ($\alpha_r = 0.1$, $\alpha_{C_I} = 0.0116$ and $\alpha_{C_I} = 0.2457$).

For both reconstruction cases (a) and (b), the constraint $0 < r_{i,j} < 1$ is required to ensure that the reconstruction of the inner object stays within the unit sphere at each iteration of the MCMC. However, in Case (a) the radii $r_{i,j}$ are equal, hence only one radius is estimated in addition to the $2(N-1) \times N$ coefficients.

Figure 5.9 shows the three-dimensional reconstruction. It can be seen that, as the number of MCMC iterations increase $K \in \{5, 10, 20, 40\}$, the corresponding estimated radius $\{0.4884, 0.4930, 0.4977, 0.4987\}$ becomes closer to the true value which is 0.5 with relatively small standard deviation.

Figure 5.10 illustrates the three-dimensional reconstruction for the star-shaped model. It can be seen that, as the number of MCMC iterations increase, the average of corresponding estimated radii becomes closer to the true value which is 0.5 and its standard deviation is much smaller (i.e. when $K = 40$ the estimated radius is 0.4968 with corresponding standard deviation 0.0094).

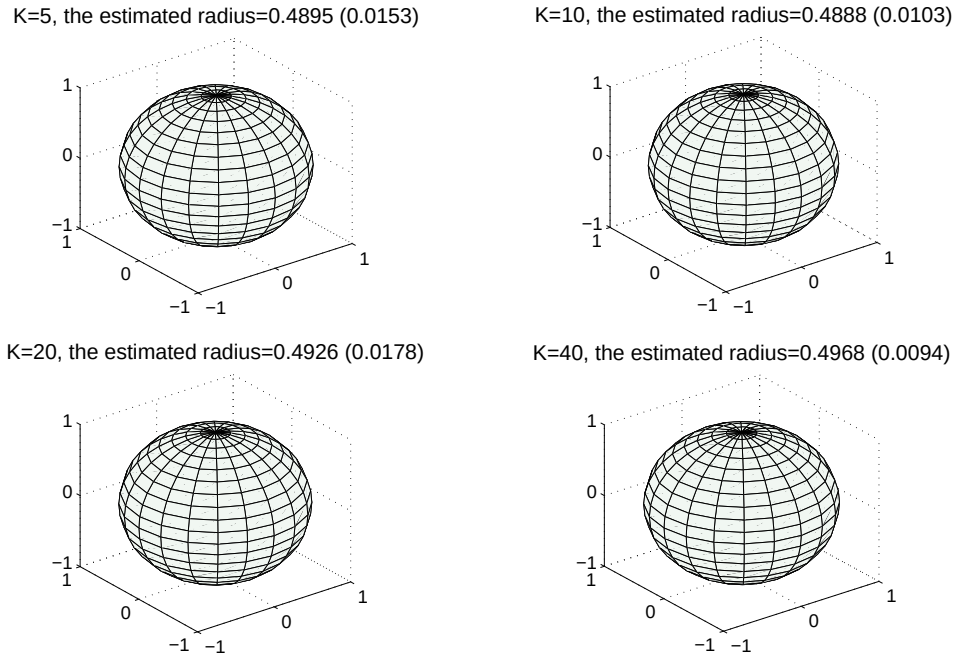

Figure 5.10: Star-shaped model reconstruction: the estimated radius for various MCMC iterations $K \in \{5, 10, 20, 40\}$, for with full posterior distribution with hyper-prior parameters ($\alpha_r = 0.1$, $\alpha_{C_I} = 0.0116$ and $\alpha_{C_I} = 0.2457$).

Experiment 2. Find the inverse solution of Problem $2(b)$ by fitting a star-shaped object model using the data from an ellipsoid inner inclusion of radius

$$r(\theta, \phi) = \sqrt{(0.5 \sin\theta \cos\phi)^2 + (0.5 \sin\theta \sin\phi)^2 + (0.4 \cos\theta)^2},$$

$$\theta \in (0, \pi),\ \phi \in [0, 2\pi).$$

centred at $(0, 0, 0)$, where the Dirichlet data on $\partial\Omega_{Outer}$ is taken as

$$u(x, y, z) = e^{x+y}, \quad (x, y, z) \in \partial\Omega_{Outer}.$$

We apply the MFS with the same inputs as in Experiment 1.

Figure 5.11 shows an excellent three-dimensional reconstruction for the ellipsoid star-shaped model. The MCMC algorithm converges to the exact ellipsoid within just a few iterations with a run time, for $K = 80$, at about three hours.

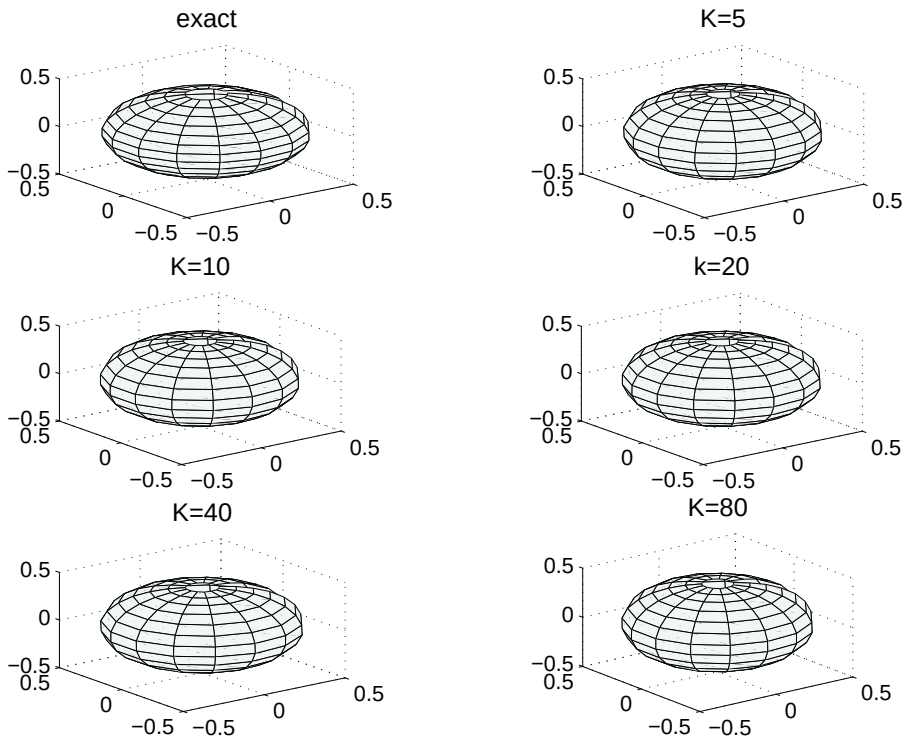

Figure 5.11: Star-shaped model reconstruction: The exact inner ellipsoid, and the fitted ellipsoids for various MCMC iterations $K \in \{5, 10, 20, 40, 80\}$, with prior parameters ($\alpha_r = 0.1$, $\alpha_{C_I} = 0.0116$ and $\alpha_{C_I} = 0.2457$).

One way to illustrate that the MCMC works well is to consider the 2-norm values of $(r_{i,j}^{MFS} - r_{i,j}^{exact})$, where $i = \overline{1, 14},\ j = \overline{1, 15}$, as well as the maximum absolute error values which are calculated over the grid for $K \in \{5, 10, 20, 40, 80\}$, see Table 5.1. The random fluctuations suggest that the algorithm is in equilibrium and mixing well.

Table 5.1: The 2-norm of a $(r_{i,j}^{MFS} - r_{i,j}^{exact})$ and the maximum absolute error of the same matrix, over the mesh $i = \overline{1,14},\ j = \overline{1,15}$, for Experiment 2 and corresponding to various number of MCMC iterations $K \in \{5, 10, 20, 40, 80, 160, 320\}$.

K	$\|\|r_{i,j}^{MFS} - r_{i,j}^{exact}\|\|$	$\max \|r_{i,j}^{MFS} - r_{i,j}^{exact}\|$
5	0.0068	0.0063
10	0.0053	0.0036
20	0.0066	0.0036
40	0.0086	0.0052
80	0.0084	0.0031
160	0.0102	0.0028
320	0.0168	0.0047

A better way to illustrate that the MCMC algorithm preforms well is to investigate the reliability of the obtained reconstructions in Figure 5.11 by running the same reconstructing code for 2000 iterations. This took three days of running time. Figure 5.12 plots the object boundary credible intervals for some cross-sections of the three-dimensional reconstruction in the xy-plane. From this figure, it can be seen that the width of the credible intervals is very narrow near the top and the bottom of the reconstructed ellipsoid compared to the ones at the middle. The occurrence of such width differences is physically interpreted as having less data points around the ellipsoid centre while there is more data towards the extreme top and bottom.

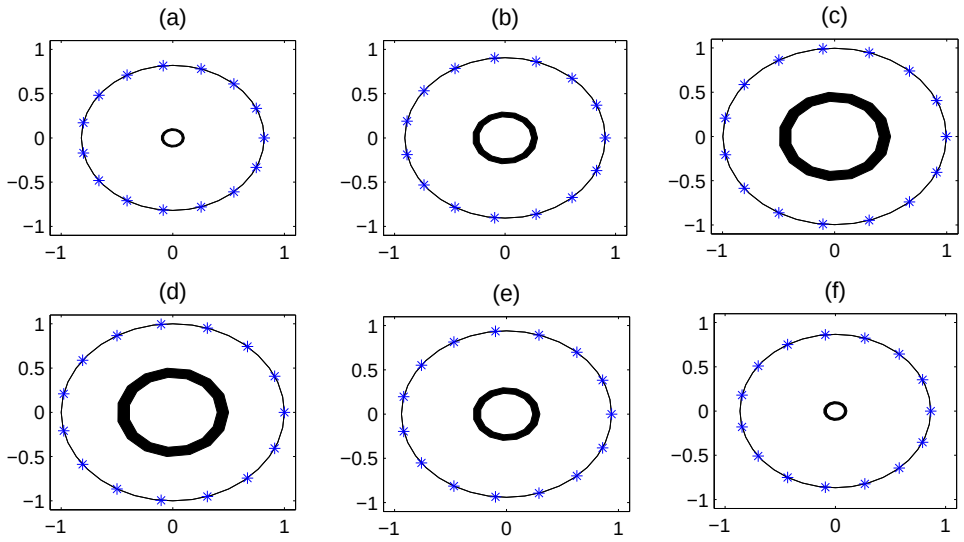

Figure 5.12: Credible intervals for various cross-sections $\theta = \{\frac{\pi}{14}, \frac{3\pi}{14}, \frac{6\pi}{14}, \frac{8\pi}{14}, \frac{11\pi}{14}\ \frac{13\pi}{14}\}$ and $(\phi)_{j=\overline{1,15}} \in [0, 2\pi)$.

An alternative way to examine the accuracy and uncertainty is to consider the surface of the standard deviation shown in Figure 5.13. It can be seen that the standard deviation values over the grid $i = \overline{1, 14},\ j = \overline{1, 15}$ are close to each other but show an ellipsoidal pattern. This confirms that the MCMC algorithm is correctly implemented.

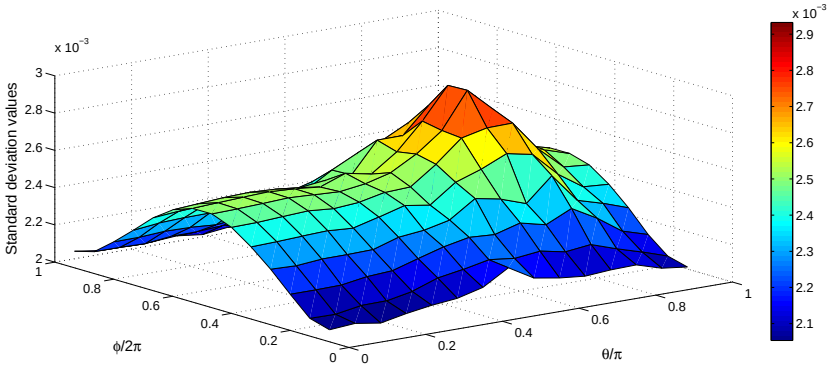

Figure 5.13: The standard deviation over the chosen mesh.

As the standard deviation values are small over the selected grid, henceforth, it is

sufficient to consider the reliability of the reconstruction and efficiency of the MCMC method using only the credible intervals.

Experiment 3. Find the inverse solution of Problem 3 by fitting a star-shaped object model using the data from two spherical inclusions of radii 0.4 centred at $(0, 0.5, 0)$ and $(0, -0.5, 0)$.

Firstly, we calculate the current flux $\partial u/\partial u$ numerically on the external boundary $\partial\Omega_{Outer}$ by solving the forward Dirichlet problem (5.1), (5.3), (5.5) and (5.6) using the MFS with the same inputs as in Experiment 1. However, we take into account that extending the number of rigid inclusions to two leads to a bigger number of equations, $2(N-1)N + 2(M-1)M = 2 \times 210 + 2 \times 210 = 840$ equations with $5(N-1)N = 5 \times 210 = 1050$ unknowns.

Figure 5.14 illustrates excellent three-dimensional reconstruction for the two star-shaped models compared to the exact one. The MCMC algorithm provides very good estimation for both inclusions compared to the truths after few iterations. Figure 5.15 shows the credible intervals over some selected cross-sections of the three-dimensional reconstructions to ensure the certainty of the solution.

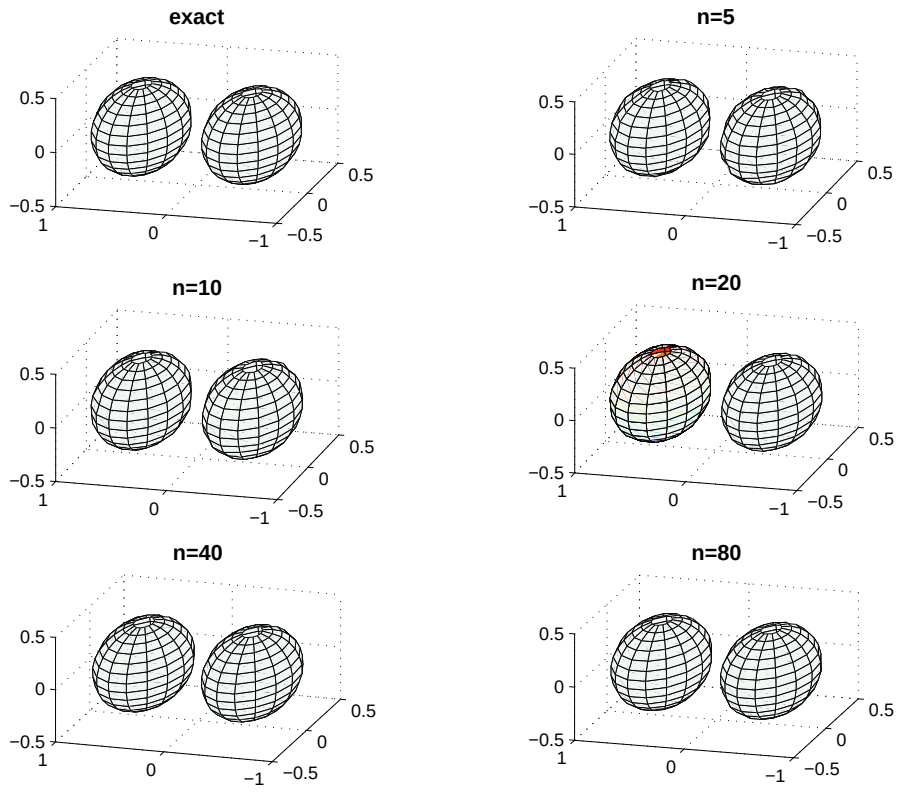

Figure 5.14: Star-shaped models reconstruction: The exact inner spheroids and the fitted spheroids for various MCMC iterations $K \in \{5, 10, 20, 40, 80\}$, with prior parameters ($\alpha_r = 0.1$, $\alpha_{C_I} = 0.0116$ and $\alpha_{C_I} = 0.2457$).

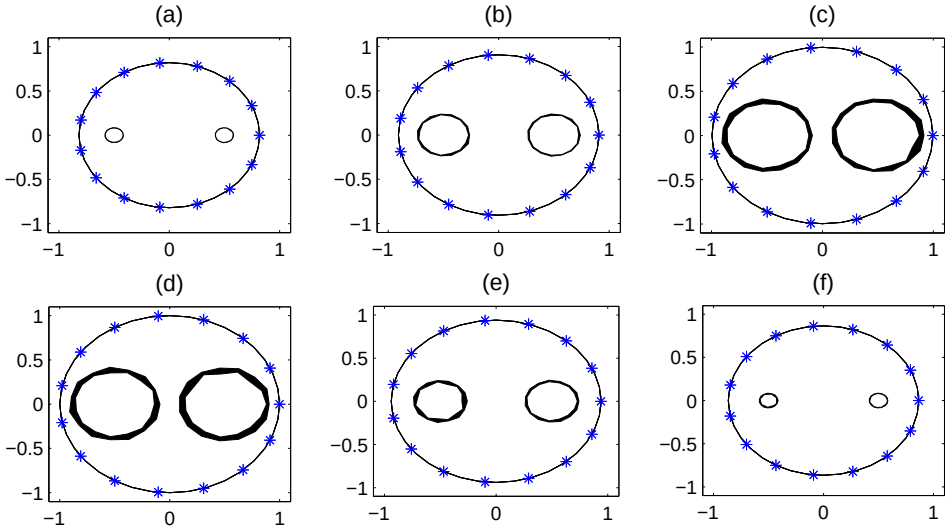

Figure 5.15: Credible intervals for various cross-sections $\theta = \{\frac{\pi}{14}, \frac{3\pi}{14}, \frac{6\pi}{14}, \frac{8\pi}{14}, \frac{11\pi}{14}\ \frac{13\pi}{14}\}$ and $(\phi)_{j=\overline{1,15}} \in [0, 2\pi)$.

5.7 Conclusion

The MFS has been successfully used in combination with the MCMC method to solve the three-dimensional inverse problem in the continuous model of ERT. In the first instance, a series of examples have been solved by the MFS in order to obtain the forward solutions of direct problems in a simply-connected domain (Problem 1), multiply-connected domain either with a spherical rigid inclusion or with an elliptical rigid inclusion (Problem 2). These solutions are represented in terms of the MFS outer boundary derivative, the MFS inner boundary derivative and the MFS interior solutions and are compared with the corresponding exact solution. The MCMC reconstruction method successfully detects the three-dimensional inner sphere or ellipsoid. The purpose of considering Examples 1-3 was to investigate and discuss the influence of the number of collocation and source points, as well as their locations. Furthermore, the only difference in the statistical modelling in the three-dimensional approach was that we have to deal with matrices instead of vectors (Chapters 3 and 4) in terms of the data and model parameters. Numerical results illustrate very good reconstructions for

the inner objects in Problems 1-3. This is justified by the accuracy and efficiency of using MCMC algorithm which has been verified by plotting cross-sections of credible intervals.

Chapter 6

Conclusions

6.1 Summary

This thesis has dealt with a novel approach to solve electrical tomography problems. This approach can be described briefly as follows. The MFS is applied to direct ERT problems subject to the CEM or continuous model boundary conditions. Potential and current flux or voltages are used in an MCMC reconstruction algorithm in order to successfully detect the shape, the size and the position of inner rigid inclusions contained within a given underlying domain. The special kind of inverse problems considered in this thesis are called inverse geometric problems and they occur in many real life applications where the inner object is not known and needs to be determined.

In Chapter 1, the direct CEM problem of ERT is a well-posed problem because it satisfies the existence, uniqueness and stability properties [61]. Also, it describes the potential and current flux on the boundary which lead to the calculated voltages. The inverse ERT problem aims to reconstruct an inner inclusion from voltage measurements for a wide range of injected current patterns and it is severely ill-posed, since a big change in the conductivity distribution may result in a very small variation in the measured boundary voltages.

In Chapter 2, the two-dimensional CEM of ERT has been described by Laplace's equation subject to integrated Robin boundary conditions where the electrochemical

effect between the attached electrodes and the surface of the object has been added to the shunt model. Moreover, the BEM and the MFS have been applied to find the forward solutions. These solutions were represented by the potential, current flux and the voltages on the boundary and the interior potential. These were and examined for different ERT problems where the domain was simply-connected or multiply-connected (containing either a rigid inclusion or a cavity). The methods were also extended to obtain the forward solutions of composite bi-materials. The BEM was considered as the 'exact' solution because in such ERT problems the analytic solutions are impossible to be obtain. Moreover, the BEM solution is convergent and stable.

Chapter 3 has presented the solution of the inverse CEM of ERT in planar domains with a rigid inclusion inside using the MCMC and the MFS. Firstly, the MFS numerical values of forward solutions for the potential and current flux on the outer boundary have been compared for circular, elliptical and bean-shaped rigid inclusions in order to show the data sensitivity to the geometric shape changes of the inner object. This ensured that such data is useful for finding the inverse solution of CEM problem. Moreover, the interior equipotential lines show that for a single current pattern injecting on opposite sides defined in (3.4) is better than applying an adjacent current pattern, such as (3.3), when we solved the inverse CEM problems. This is because more of the doubly-connected domain is scanned by the isolines. In the second part of Chapter 3, a set of experiments has been carried out to determine the shape and the size of inner rigid inclusions based on combination of the MFS direct solver and the statistical modeling approach which has first been used in [6, 7] for rigid inclusion reconstructions in two-dimensional continuous model problems. Specially written MCMC code has been used to reliably estimate the model parameters (the MFS coefficients and the radii) of the inner object. The output was also used for plotting error estimates, object boundary histograms, object boundary credible intervals, fitted inclusion, and to estimate MFS coefficients (with credible intervals). In initial experiment, the optimal hyper-prior parameters fixed values considered in [6] were used. These worked well for the simple experiment of fitting a circular object data truth object when $L = 2$,

Experiment 1. After that, the hyper-prior parameters of the radii were varied and an excellent reconstruction of fitting a star-shaped object from true circle data, Experiment 3, has been achieved. However, fitting a star-shaped object to elliptical true data when $L = 2$ (Experiment 4) did not provide as successful a reconstruction for the inner object as the one in Experiment 3. This is why, at this point of research, we decided to move to the more practical case when the number of electrodes is extended to four and the data type is changed to be voltage measurements. In this case, three different current patterns were injected simultaneously and a set of 12 voltages were collected. The hyper-prior parameters of MFS coefficients and radii model parameter in Experiments 5-7 have been slightly changed by multiplying the previous choice by ten. This resulted in much improvement in the inner object reconstruction when we fitted a star-shaped object using data from a circular or an elliptical inclusion, Experiments 6 and 7. In the last section of Chapter 3, we extended the number of electrodes to eight to create more realistic experiments. This produced seven current patterns which resulted in 56 voltage measurements. The accuracy of the object reconstruction was very good. This was obvious from the small estimated errors, the tiny object boundary histogram, the narrow object boundary credible intervals linked to the inner and outer MFS coefficients, see Experiments 8 and 9.

In Chapter 4, the identification of the centre of a rigid inclusion along with the constant contact impedances and extension to multiple rigid inclusions have been considered. We have utilised the same technique as before based on the MFS and MCMC method and we have run three sets of experiments. The purpose of Experiment 1 was to detect the shape, the size and the position of a star-shaped object when $L = 4$ and $L = 8$ (this showed better object reconstruction and more accurately estimated centre). Experiment 2 was to identify the radii and centre of a rigid inclusion based on voltage data collected from a circular true inclusion, as well as to estimate the contact contact impedances along (this provided good results). In Experiment 3, we extended the work to detect two rigid inclusions which means, in fact, estimated two sets of radii, in addition to estimating the centres of the two inclusions.

In Chapter 5, an extension to solve the three-dimensional ERT problem has been developed. The same strategy of combining the MFS and MCMC method was employed in order to solve the inverse continuous model problems of ERT in three-dimensional domains. This investigation will pave the way towards very practical experiments of solving the inverse CEM in three dimensions (future work). Examples 1-4 examined and compared the forward solutions for the outer derivative, the inner derivative and the interior solutions. In terms of solving the inverse problems, we used noisy Cauchy data in order to estimate the model parameters. Extending to three dimensions has caused some slight changes in the statistical modeling approach where the measured data and the model parameters were represented in matrix forms instead of vectors in two dimensional problems (Chapters 3 and 4). In all experiments, the star-shaped model reconstructions showed very good fitted objects for both one inner (Experiments 1 and 2) or two inner rigid inclusions (Experiment 3).

In summary, the inverse problems of ERT have been solved using MFS forward solutions combined with the MCMC method. Most rigid inclusion reconstructions and model parameters have been well-estimated with very small estimated errors, estimated standard deviation and very narrow credible intervals. This gives us insight into solving real applications of ERT in future.

6.2 General conclusions

In this thesis, all the obtained MFS forward solutions of ERT problems were very accurate since they provide very good agreement with the BEM solutions. Nevertheless, the MFS is much easier to implement especially in three-dimensions, than the BEM as it is a meshless method. Although applying the MFS to the same set of two-dimensional ERT problems shows some instability that occurs when the degrees of freedom become very large $N = M = 256$, we have demonstrated that for lower values $N = M \in \{16, 32, 64, 128\}$ its accuracy and stability were excellent compared to

the BEM numerical solutions. It turns out to be sufficient to choose $N = M = 16$ for three-dimensional cases to produce very accurate and stable MFS numerical solutions. In addition, the computational time is much smaller when the MFS has been applied. This has a big advantage which clearly appears when the MFS direct solver is called thousands of times in the inverse problems as in the MCMC estimation algorithm. This advantage is enhanced when three-dimensional reconstruction was considered, where choosing $N = M = 16$ resulted in a large number of $3(M-1)M = 720$ collocation points and $3(N-1)N = 720$ of source points.

We have considered two ways of collecting the input data in order to find the inverse solution of the CEM in ERT. Firstly, we injected a single current through electrodes then calculated the potential and current flux at equally-spaced points on the outer boundary. It was proved that using two opposite electrodes has produced better reconstruction than applying the single current via adjacent electrodes. However, there is an ideal way of collecting data and providing better results, where we applied multiple current patterns and then equation (2.4) is used to calculate the voltages. Increasing the number of the current patterns allows us to obtain more voltage data which, in turn, leads to much better object reconstructions. As for solving the inverse problem of the three-dimensional continuous model, the data was only a Cauchy pair of the boundary potential and current flux which also provided excellent results.

We have clarified, through a series of experiments, that the proposed strategy of using the Bayesian statistical framework (which is linked to the MFS direct solver) is a very successful approach to solving ERT problems. Furthermore, the model parameters (this could be the radii, MFS coefficients, the centre coordinates or the contact impedance values) have been well-estimated. We have demonstrated that the MCMC algorithm does not only provide the desired solutions but also assess the uncertainties and the reliability of those estimators by standard deviations, as well as by visualising the object boundary histograms and credible intervals.

6.3 Future work

So far, we have shown that the MFS combined with the Bayesian statistical approach can be developed for solving inverse geometric problems governed by Laplace's equation in two and three dimensions. This corroborates the idea that the MFS combined with the MCMC algorithms can be implemented for other related work, such as:

(i) An inverse geometric problem related to solve the CEM of ERT in two and three dimensions of Chapter 2 for a cavity (replacing equation (3.2) by (2.46)) and for bi-material composite (replacing equation (3.2) by equations (2.50) and (2.50)).

(ii) Another possible future work is to reconstruct more complicated shapes of inclusions and extend the analysis to solve three-dimensional inverse CEM of ERT.

(iii) Assuming the number of rigid/cavity inclusions in (continuous model/CEM) problem of ERT is not known, determine that number, as well as detect the location, the shape and the size of each inclusion.

(iv) Invert real data collected directly from the patient.

Appendix A

Uniqueness proofs and density results

This appendix aims to cite the most significant theoretical results that are linked to the thesis, namely:

(i) The boundary curve of the inner rigid inclusion is uniquely detected from one pair of non-trivial Cauchy data specified on the external boundary, [29, 46].

(ii) Density results for the MFS applied to two and three-dimensional potential problems, [14, 60].

(iii) Well-posedness of the complete-electrode model (CEM), [61].

A.1 Uniqueness in determining a rigid inclusion

Assume that $\Omega = \Omega_{Outer} \backslash \Omega_{Inner}$ (with $\Omega_{Inner} \subset \Omega_{Outer}$) is an annular domain in $\mathbb{R}^n,\ n = 2, 3$, with boundary $\partial\Omega = \partial\Omega_{Outer} \cup \partial\Omega_{Inner}$. To determine the unknown boundary $\partial\Omega_{Inner}$ of a perfectly conducting inclusion (rigid inclusion), we have to solve the following inverse boundary value problem:
Given a single pair of Cauchy data (f, g) on $\partial\Omega_{Outer}$ we wish to determine $\partial\Omega_{Inner}$ and a function $u \in C^2(\Omega) \cap C(\overline{\Omega})$ which satisfy the Laplace's equation

$$\Delta u = 0 \quad \text{in} \quad \Omega \tag{A.1}$$

subject to

$$u = 0 \quad \text{on} \quad \partial\Omega_{Inner} \text{ (rigid inclusion)}, \tag{A.2}$$

and the Cauchy data specification

$$u = f \quad \text{on} \quad \partial\Omega_{Outer}, \tag{A.3}$$

$$\frac{\partial u}{\partial n} = g \quad \text{on} \quad \partial\Omega_{Outer}. \tag{A.4}$$

The following theorem, [29, 46], gives the uniqueness of the inverse problem (A.1)-(A.4).

Theorem 1. *Let $\partial\Omega_{Inner} = \Gamma$ and $\partial\tilde{\Omega}_{Inner} = \tilde{\Gamma}$ be two closed curves which are contained in the interior of Ω_{Outer} and denote by u and $\tilde{u}$ the solutions to the forward well-posed Dirichlet problems (A.1)-(A.3) with the inner boundaries Γ and $\tilde{\Gamma}$, respectively. Assuming that $f \not\equiv 0$ and*

$$\frac{\partial u}{\partial n} = \frac{\partial \tilde{u}}{\partial n} \tag{A.5}$$

on an open set of $\partial\Omega_{Outer}$ then $\Gamma = \tilde{\Gamma}$.

Proof. From (A.5) and Holmgren's uniqueness theorem we can obtain that $u = \tilde{u}$ in the connected component V of $\Omega_{Outer}\backslash(\Omega_{Inner} \cup \tilde{\Omega}_{Inner})$ which contains the exterior boundary $\partial\Omega_{Outer}$. Without loss the generality, we can consider that $V^* := (\Omega_{Outer}\backslash\overline{V})\backslash\Omega_{Inner}$ is a non-empty set. As a result, u is defined in V^* because it describes the solution of problem (A.1)-(A.3) for Γ. Moreover, u is harmonic in V^*, continuous in $\overline{V}^*$, as well as it satisfies the homogeneous boundary condition $u = 0$ on ∂V^*. This boundary condition shows that each boundary point ∂V^* either belongs to Γ or to $\partial V \cap \tilde{\Gamma}$.

Now, for $x \in \Gamma$ we have $u(x) = 0$ because of the boundary condition for u, and for $x \in \tilde{\Gamma}$ we have $u(x) = \tilde{u}(x)$. Hence, $u(x) = 0$ due to the homogeneous boundary condition for $\tilde{u}$. Now, using the maximum principle for harmonic functions we can obtain that $u = 0$ in V^*, and from this it follows that $u = 0$ in Ω. Finally, this contradicts the fact that $f \not\equiv 0$ on $\partial\Omega_{Outer}$ and this completes the proof of uniqueness.

A.2 Density results for the solutions of harmonic problems

In this section, the following Dirichlet problem for Laplace's equation is considered:

$$\begin{cases} \bigtriangledown^2 u = 0 & \text{in} \quad \Omega \subset \mathbb{R}^n, \\ u = f & \text{on} \quad \partial\Omega. \end{cases} \tag{A.6}$$

In (A.6), the domain Ω is bounded, otherwise a condition at infinity should be added.

Let the function $G(\underline{x}, \underline{y}) = e_1(\underline{x} - \underline{y})$ define the fundamental solution of the elliptic Laplacian operator, where

$$e_1(\underline{x}) = \begin{cases} -\frac{\log|\underline{x}|}{2\pi}, & \text{if} \quad n = 2, \\ -\frac{|\underline{x}|^{2-n}}{(2-n)\gamma_{n-1}}, & \text{if} \quad n > 2, \end{cases} \tag{A.7}$$

and γ_{n-1} is the area of the surface of the unit spheroid S^{n-1} in $\mathbb{R}^n$. When we apply the MFS, we seek the approximated solution of the problem (A.6) as a finite linear combination of fundamental solutions,

$$u_N(\underline{x}, \underline{c}) = \sum_{j=1}^{N} c_j G(\underline{x}, \underline{y}_j) = \sum_{j=1}^{N} c_j e_1(\underline{x} - \underline{y}_j), \quad \underline{x} \in \overline{\Omega}, \tag{A.8}$$

where the 'singularities' $\underline{y}_j \in \mathbb{R}^n \backslash \overline{\Omega}$ and the MFS coefficients $\{c_j\}_{j=\overline{1,N}}$ are determined by applying the boundary condition $u = f$ on $\partial\Omega$.

We investigate whether the span of the space of the finite linear combinations (A.8) is dense in the space of harmonic functions in Ω, where the sources ('singularities') $\{\underline{y}_j\}_{j=\overline{1,N}}$ lie on a prescribed pseudo- boundary $\partial\Omega'$ enclosing the domain Ω. More rigorously, we have the following definition on where the MFS sources are located.

Definition 1**.** Consider Ω and Ω' be open connected subset of $\mathbb{R}^n$. We say that Ω' *embraces* Ω if $\overline{\Omega} \subset \Omega'$, and $\Omega' \backslash \Omega$ does not contain any closed connected components.

The Space $C^\lambda(\overline{\Omega})$

The space $C^\lambda(\Omega)$, where $\lambda \in \mathbb{N}$, contains all functions u which, together with all their partial derivatives $D^\alpha u$ of orders $|\alpha| \leq \lambda$, are continuous in Ω. The space $C^\lambda(\overline{\Omega})$ consists of all functions $u \in C^\lambda(\Omega)$ for which $D^\alpha u$ is uniformly continuous and bounded in Ω for every $|\alpha| \leq \lambda$. This it is a Banach space with the norm

$$|u|_{\lambda,\overline{\Omega}} = \max_{|\alpha|\leq\lambda} \sup_{\underline{x}\in\overline{\Omega}} |D^\alpha u(\underline{x})|. \tag{A.9}$$

The following theorem states the density result which warrants the application of the MFS for solving the problem (A.6).

Theorem 2. (see [60]) *Let $\Omega \subset \Omega'$ be domains in $\mathbb{R}^n$ such that Ω' embraces Ω. Then, the space $\mathcal{X}$ of finite linear combination $\sum_{j=1}^N c_j e_1(\underline{x} - \underline{y}_j)$, where e_1 is defined in (A.7) and the sequence $\{\underline{y}_j\}_{j=\overline{1,N}} \subset \partial\Omega'$, is dense in*

$$\mathcal{Y}_\lambda := \{u \in C^2(\Omega); \Delta u = 0 \text{ in } \Omega\} \cap C^\lambda(\overline{\Omega}), \tag{A.10}$$

with respect to the norm (A.9) of space $C^\lambda(\overline{\Omega})$ if $n \geq 3$. If $n = 2$, then the linear sum $\mathcal{X} \oplus \{c.1|_{\overline{\Omega}}; c \in \mathbb{R}\}$ is dense in $\mathcal{Y}_\lambda$ with respect to the same norm.

A.3 Well-posedness of the CEM

The CEM which was described in equations (2.1) and (2.3)-(2.5), does formulate well if the conservation of charge is included

$$\sum_{p=1}^{L} I_p = 0, \tag{A.11}$$

since this condition is needed for existence of a solution. Also, a condition specifying the zero potential (the ground) is needed for solution uniqueness, [61],

$$\sum_{p=1}^{L} U_p = 0. \tag{A.12}$$

Now, to prove the uniqueness for the CEM, we assume that there are two solutions (u, U) and $(\hat{u}, \hat{U})$ in $H = H^1(\Omega) \oplus \mathbb{R}^L$ of equations (2.1) and (2.3)-(2.5) which satisfy conditions (A.11) and (A.12). We let

$$(v, V) = (u, U) - (\hat{u}, \hat{U}); \tag{A.13}$$

this means that (v, V) satisfies (2.1), (2.4), (2.5) and

$$\int_{\varepsilon_p} \frac{\partial v}{\partial n}\, ds = 0. \tag{A.14}$$

Hence, our solution consists of the electric potential in the interior which denoted by v, as well as L surface voltages denoted by V.

Using Green's formula and equation (2.1), we obtain

$$0 = \int_{\Omega} v \bigtriangledown \cdot \bigtriangledown v\, dx = \int_{\partial\Omega} v \frac{\partial v}{\partial n}\, ds - \int_{\Omega} |\bigtriangledown v|^2 dx. \tag{A.15}$$

We substitute condition (2.4) into (A.15) to obtain

$$\int_{\Omega} |\bigtriangledown v|^2 dx = \sum_{p=1}^{L} \int_{\varepsilon_p} \left(V_p - z_p \frac{\partial v}{\partial n} \right) \frac{\partial v}{\partial n} \, ds. \tag{A.16}$$

With the help of (A.14) using that V_p is constant over ε_p, one can rewrite (A.16) as

$$\int_{\Omega} |\bigtriangledown v|^2 dx = -\sum_{p=1}^{L} \int_{\varepsilon_p} z_p \left| \frac{\partial v}{\partial n} \right|^2 ds. \tag{A.17}$$

Since $z_p \geq 0$ it follows that both sides of equation (A.17) are equal only if they are zeros. This means that v is constant. From (2.4), this means that all the voltages V_p's are also equal to the same constant. In addition to this, from (A.12) it can be seen that this constant must be zero. Hence, we have proved that $(v, V) = (0, 0)$ which implies the uniqueness of the solution of the CEM.

Bibliography

[1] P. Aberg, I. Nicander, J. Hansson, P. Geladi, U. Holmgren and S. Ollmar, *Skin cancer identification using multifrequency electrical impedance-a potential screening tool*, IEEE Biomedical Engineering, **51**, (2004), 2097-2102.

[2] R. G. Aykroyd, *Statical image reconstruction*, In: Industrial Tomography: Systems and Applications, (ed. M. Wang), Elsevier, New York, (2015), 401-427.

[3] R. G. Aykroyd, B. A. Cattle and R. M. West, *Boundary element method and Markov chain Monte Carlo for object location in electrical impedence tomography*, 5th International Conference on Inverse Problems in Engineering: Theory and Practice, (ed. D. Lesnic), Chapter **A09**, Vol. II, (2005), (5 pages).

[4] R. G. Aykroyd, and B. A. Cattle, *A flexible statistical and efficient computational approach to object location applied to electrical tomography*, Statistical Computation, **16**, (2006), 363-375.

[5] R. G. Aykroyd and B. A. Cattle, *A boundary-element approach for the complete-electrode model of EIT illustrated using simulated and real data*, Inverse Problems in Science and Engineering, **15**, (2007) 441-461.

[6] R. G. Aykroyd, D. Lesnic and A. Karageorghis, *A fully Bayesian approach to shape estimation of objects from tomography data using MFS forward solutions*, International Journal of Tomography and Simulation, **28**, (2015), 1-21.

[7] R. G. Aykroyd, D. Lesnic and A. Karageorghis, *A Bayesian approach for shape*

estimation of objects, In: 4th Inverse Problems, Design and Opimization Symposium (IPDO 2013), (eds. O. Fudym, J.-L. Battaglia, G.S. Dulikravich, H.R.B. Orlande and M.J. Colaco), Ecole des Mines d'Albi-Carmaux, Albi, France, Paper 06632, (2013), (10 pages).

[8] S. Babaeizadeh, *3-D Electrical Impedance Tomography for Domains with Piecewise Constant Conductivity*, The Department of Electrical and Computer Engineering, Northwestern University, (2006), (192 pages).

[9] A. J. Barrow and S. M. Wu, *Impedance measurements for cervical cancer diagnosis*, Gynecologic Oncology, 5th International Conference on Cervical Cancer, **107**, (2007), S40-S43.

[10] R. H. Bayford, *Bioimpedance tomography (Electrical Imedance Tomography)*, Annual Review of Biomedical Engineering, **8**, (2006), 63-91.

[11] J. R. Berger and A. Karageorghis, *The method of fundamental solutions for heat conduction in layered materials*, International Journal for Numerical Methods in Engineering, **45**, (1999), 1681-1694.

[12] J. R. Berger and A. Karageorghis, *The method of fundamental solutions for heat conduction in layered elastic materials*, Engineering Analysis with Boundary Elements, **25**, (2001), 877-886.

[13] B. Bin-Mohsin and D. Lesnic, *The method of fundamental solutions for Helmholtz-type equations in composite materials*, Computers and Mathematics with Applications, **62**, (2011), 4377-4390.

[14] A. Bogomolny, *Fundamental solution method for elliptic boundary value problems*, SIAM Journal on Applied Mathematics, **22**, (1985), 644-669.

[15] D. J. Borman, D. B. Ingham, B. T. Johansson and D. Lesnic, *The method of fundamental solutions for detection of cavities in EIT*, Journal of Integral Equations and Applications, **21**, (2009), 381-404.

[16] B. Blad and B. Baldetorp, *Impedance spectra of tumour tissue in comparison with normal tissue; a possible clinical application for electrical impedance tomography*, Physiological Measurement, **17**, (1996), A105-A115.

[17] C. Chen, H. Cho and M. Golberg, *Some comments on the ill-conditioning of the method of fundamental solutions*, Engineering Analysis with Boundary Elements, (2006), 405-410.

[18] K. S. Cheng, D. Isaacsson, J. C. Newell and D. G. Gisser, *Electrode models for electric current computed tomography*, IEEE Transactions on Biomedical Engineering, **36**, (1989), 918-924.

[19] M. Cheney, D. Isaacson, and J. C. Newell, *Electrical impedance tomography*, SIAM Review, **41**, (1999), 85-101.

[20] V. Cherepenin, A. Karpov, A. Korjenevsky, V. Kornienko, A. Mazaletskaya, D. Mazourov and D. Meister, *A 3D electrical impedance tomography (EIT) system for breast cancer detection*, Physiological Measurement, **22**, (2001), 9-18.

[21] V. A. Cherepenin, A. Y. Karpov, A. V. Korjenevsky, V. N. Kornienko, Y. S. Kultiasov, M. B. Ochapkin, O. V. Trochanova and J. D. Meister, *Three-dimensional EIT imaging of breast tissues: system design and clinical testing*, IEEE Transactions on Medical Imaging, **21**, (2002), pp. 662-667.

[22] F. Delbary and R. Kress, *Electrical impedance tomography using a point electrode inverse scheme for complete electrode data*, Inverse Problems and Imaging, **5**, (2011), 355-369.

[23] F. Dong, Z. X. Jiang, X. T. Qiao and L. A. Xu, *Application of electrical resistance tomography to two-phase pipe flow parameters measurement*, Flow Measurement and Instrumentation, **14**, (2003), 183-192.

[24] G. Dong, J. Zou, R. H. Bayford, X. Ma, S. Gao, W. Yan and M. Ge, *The comparison between FVM and FEM for EIT forward problem*, IEEE Transactions on Magnetics, **41**, (2005), 1468-1471.

[25] T. Dyakowski, F. C. Jeanmeure and A. J. Jaworski, Applications of electrical tomography for gas-solids and liquid-solids flows: a review, *Powder Technology*, **112**, (2000), 174-192.

[26] T. E. Dyhoum, D. Lesnic and R. G. Aykroyd, *Solving the complete-electrode direct model of ERT using the boundary element method and the method of fundamental solutions*, Electronic Journal of Boundary Elements, **12**, (2014), 26-71.

[27] I. Frerichs, *Electrical impedance tomography (EIT) in applications related to lung and ventilation: a review of experimental and clinical activities*, Physiological Measurement, **21**, (2000), R1-R21.

[28] S. Geman and D. Geman, *Stochastic relaxation, Gibbs distributions and the Bayesian restoration of image*, IEEE Transactions on Pattern Analysis and Machine Intelligence, **6**, (1984), 721-741.

[29] H. Haddar and R. Kress, *Conformal mappings and inverse boundary value problems*, Inverse Problems, **21**, (2005), 935-953.

[30] K. M. Hanson, *Introduction to Bayesian Image Analysis*, Medical Imaging: Image Processing, (1993), 716-731.

[31] M. A. Heravi, L. Marin and C. Sebu, *The method of fundemental solutions for complex electrical impedance tomography*, Engineering Analysis with Boundary Elements, **46**, (2014), 126-139.

[32] D. S. Holder, *Electrical Impedance Tomography of Brain Function*, Department of Medical Physics, University College London and Clinical Neurophysiology, University College Hospital, London, UK, 1-7.

[33] G. Hu, M. Chen, W. He and J. Zhai, *A novel forward problem solver based on meshfree method for electrical impedance tomography*, Przeglad Elektrotechniczny, **89**, No.2a, (2013), 234-237.

[34] J. P. Kaipio, V. Kolehmainen, E. Somersalo and M. Vauhkonen, *Statistical inversion and Monte Carlo sampling methods in electrical impedance tomography*, Inverse Problems, **16**, (2000), 1487-1522.

[35] A. Karageorghis and D.Lesnic, *Detection of cavities using the method of fundamental solutions*, Inverse Problems in Science and Engineering, **17**, (2009), 803-820.

[36] A. Karageorghis and D. Lesnic, *The fundamental solutions for inverse conductivity problem*, Inverse Problems in Science and Engineering, **18**, (2010), 567-583.

[37] A. Karageorghis, D. Lesnic and L. Marin, *A moving pseudo-boundary MFS for void detection*, Numerical Methods for Partial Differential Equations, **29**, (2013), 935-960.

[38] A. Karageorghis, D. Lesnic and L. Marin, *A survey of applications of the MFS to inverse problems*, Inverse Problems in Science and Engineering, **19**, (2011), 309-336.

[39] A. Karageorghis, D. Lesnic and L. Marin, *A moving pseudo-boundary MFS for three-dimensional void detection*, Advances in Applied Mathematics and Mechanics, **5**, (2013), 510-527.

[40] A. Karageorghis and D.Lesnic, *Application of the MFS to inverse obstacle scattering problems*, Engineering Analysis with Boundary Elements, **35**, (2011), 631-638.

[41] J. Katsikadelis, *Boundary Elements: Theory and Applications*, 1st ed., New York: Elsevier, 2002.

[42] S. Kim, R. L.Wang, A. K. Khambampati, B. A. Lee and K. Y. Kim, *An improved boundary distributed source method for electrical resistance tomography forward problem*, Engineering Analysis with Boundary Elements, **44**, (2014),185-192.

[43] T. Kitagawa, *On numerical stability of the method of fundamental solutions applied to the Dirichlet problem*, Japan Journal of Applied Mathematics, **5**, (1988), 123-133.

[44] K. Knudsen, *On the Inverse Conductivity Problem*, Ph.D. Thesis, Department of Mathematical Sciences, Aalborg University, Denmark, (2002).

[45] V. Kolehmainen, M. Lassas and P. Ola, *Electrical impedance tomography problem with inaccurately known boundary and contact impedances*, IEEE Transactions on Medical Imaging, **10**, (2008), 1404-1414.

[46] R. Kress, *Inverse Dirichlet problem and conformal mapping*, Mathematics and Computers in Simulation, **66**, (2004), 255265.

[47] D. Lesnic, L. Elliott and D. B.Ingham, *The boundary element solution of the Laplace and biharmonic equations subjected to noisy boundary data*, International Journal for Numerical Methods in Engineering, **43**, (1998), 479-492.

[48] R. Mann, F.J. Dickin, M. Wang, T. Dyakowski, R. A. Williams, R. B. Edwards, A. E. Forrest and P. J. Holden, *Application of electrical resistance tomography to interrogate mixing processes at plant scale*, Chemical Engineering Science, **52**, (1997), 2087-2097.

[49] H. Nuutti and S. Otto, *Detection of multiple inclusions from sweep data of electrical impedance tomography*, Inverse Problems, **28**, (2012), (22 pages).

[50] D. M. Otten, G. Onik and B. Rubinsky, *Distributed network imaging and electrical impedance tomography of minimally invasive surgery*, Technology in Cancer Research and Treatment, **3**, (2004), 1-10.

[51] M. K. Pidcock, M. Kuzuoglu and K. Leblebicioglu, *Analytic and semi-analytic solutions in electrical impedance tomography: I. Two-dimensional problems*, Physiological Measurements, **16**, (1995), 77-90, .

[52] P. A. Ramachandran, *Method of fundamental solutions: singular value decomposition analysis*, Communications in Numerical Methods in Engineering, **18**, (2002), 789-801.

[53] C. Robert and G. Casella, *A short history of Markov chain Monte Carlo: subjective recollections from incomplete data*, Statistical Science, **26**, (2011), 102-115.

[54] G. O. Roberts, A. Gelman and W. R. Gilks, *Weak convergence and optimal scaling of random walk Metropolis algorithms*, Statistical Science, **7**, (1997), 110-120.

[55] V. Rolnik, O. H. Menin, G. L. C. Carosio and P. S. Junior, *Study of the boundary element method for the direct problem of electrical impedance tomography*, ABCM Symposium Series in Mechatronics, **4**, (2010), 835-843.

[56] A. Samoulian, I. Cousin, A. Tabbagh, A. Bruand and G. Richard, *Electrical resistivity survey in soil science: a review*, Soil and Tillage Research, **83**, (2005), 173-193.

[57] P. Serranho, *A hybrid method for inverse scattering for sound-soft obstacles in* $\mathbb{R}^3$, Inverse Problems and Imaging, **1**, (2007), 691-712.

[58] M. Soleimani, R. Aykroyd, R. West, S. Meng and W. Lionheart, *Bayes-MCMC reconstruction from 3D EIT data using a combined linear and non-linear forward problem solution strategy*, Proceedings of the International Conference on Electrical Bio-Impedance and Electrical Impedance Tomography, **12**, (2004), 12190.

[59] M. Soleimani, C. E. Powell and N. Polydorides, *Improving the forward solver for the complete electrode model in EIT using algebraic multigrid*, IEEE Transactions on Medical Imaging, **24**, (2005), 577-583.

[60] Y.S. Smyrlis, *Applicability and applications of the method of fundamental solutions*, Mathematics of Computation, **78**, (2009), 13991434.

[61] E. Somersalo, M. Cheney and D. Isaacson, *Existence and uniqueness for electrode models for electric current computed tomography*, SIAM Journal on Applied Mathematics, **52**, (1992), 1023-1040.

[62] C. T. Soulsby, M. Khela, E. Yazaki, D. F. Evans, E. Hennessy and J. Powell-Tuck, *Measurements of gastric emptying during continuous nasogastric infusion of liquid feed: Electric impedance tomography versus gamma scintigraphy*, Clinical Nutrition, **25**, (2006), 671-680.

[63] M. Tarvainen, M. Vauhkonen, T. Savolainen and J. P. Kaipio, *Boundary Element Method and Internal Electrodes in Electrical Impedance Tomography*, Department of Applied Physics, University of Kuopio, Report No. 17, 2000.

[64] T. Tidswell, A. Gibson, R. H. Bayford and D. S. Holder, *Three-dimensional electrical impedance eomography of human brain activity*, NeuroImage, **13**, (2001), 283-294.

[65] T. Vilhunen, J. P. Kaipio, P. P. Vauhlonen, T. Savolainen and M. Vauhkonen, *Simultaneous reconstruction of electrode contact impedance and internal electrical properties: I. Theory*, Measurement Science and Technology, **13**, (2000), 1848-1854.

[66] R. M. West, R. G. Aykroyd, S. Meng and R. A. Williams, *Markov chain Monte Carlo techniques and spatial-temporal modelling for EIT*, Physiogical Measrements, **25**, (2004), 181-194.

[67] R. M. West, S. Meng, R. G. Aykroyd and R. A. Williams, *Spatial-temporal modelling for electrical impedance imaging of a mixing process*, Review of Scientific Instruments, **76**, (2005), 073703 (10 pages).

[68] B. M. Weinstock, *Uniform approximation by solutions of elliptic equations*, Proceedings of the American Mathematical Society, **41** (1973), 513-517.

[69] R. A. Williams, X. Jia, R. M. West, M. Wang, J. C. Cullivan, J. Bond, I. Faulks, T. Dyakowski, S. J. Wang, N. Climpson, J. A. Kostuch and D. Payton, *Industrial monitoring of hydrocyclone operation using electrical resistance tomography*, Minerals Engineering, **12**, (1999), 1245-1252.

[70] www.ece.rutgers.edu/∼orfanidi/ewa/ch01.pdf